LBL--32440

DE92 041194

COLLISION DYNAMICS OF METHYL RADICALS AND HIGHLY VIBRATIONALLY EXCITED MOLECULES USING CROSSED MOLECULAR BEAMS

Pamela Mei-Ying Chu

Department of Chemistry
University of California

and

Chemical Sciences Division
Lawrence Berkeley Laboratory
Berkeley, CA 94720 USA

October 1991

This work was supported by the Director, Office of Energy Research, Office of Basic Energy Sciences, Chemical Sciences Division, of the U.S. Department of Energy under Contract No. DE-AC03-76SF00098.

Collision Dynamics of Methyl Radicals and Highly Vibrationally Excited Molecules Using Crossed Molecular Beams

by

Pamela Mei-Ying Chu

Abstract

Inelastic scattering of highly vibrationally excited molecules in the ground electronic state was studied under single collision conditions using crossed molecular beams. The vibrational to translational (V→T) energy transfer in collisions between large highly vibrationally excited polyatomics and rare gases was investigated by time-of-flight techniques. Two different methods, UV excitation followed by internal conversion and infrared multiphoton excitation (IRMPE), were used to form vibrationally excited molecular beams of hexafluorobenzene and sulfur hexafluoride, respectively. The product translational energy was found to be independent of the vibrational excitation. These results indicate that the probability distribution function for V→T energy transfer is peaked at zero. The collisional relaxation of large polyatomic molecules with rare gases most likely occurs through a rotationally mediated process.

The photodissociation of nitrobenzene in a molecular beam was studied using the 266 nm radiation. Two primary dissociation channels were identified including simple bond rupture to produce nitrogen dioxide and phenyl radical and isomerization to form nitric oxide and phenoxy radical. The time-of-flight spectra indicate that simple bond rupture and isomerization occurs via two different mechanisms. Additionally, secondary

dissociation of the phenoxy radicals to carbon monoxide and cyclopentadienyl radicals was observed as well as secondary photodissociation of phenyl radical to give H atom and benzyne.

The development and characterization of a supersonic methyl radical beam source is described. The beam source configuration and conditions were optimized for CH_3 production from the thermal decomposition of azomethane. Elastic scattering of methyl radical and neon was used to differentiate between the methyl radicals and the residual azomethane in the molecular beam. This source was built in preparation for methyl radical photodissociation and reactive scattering studies.

This thesis is dedicated to my parents, Fey and Julia Chu.

Table of Contents

Abstract 1

Dedication i

Acknowledgements v

Chapter 1.

1.1 Introduction 1

1.2 References 4

Chapter 2. Collisional Deactivation of Highly Vibrationally Excited Molecules Using Crossed Molecular Beams.

2.1 Introduction 5

2.2 Experimental 23

2.2.1 Apparatus 23

2.2.2 Background Reduction 27

2.2.3 The Vibrationally Excited Molecular Beam 29

2.2.4 UV Excitation of Hexafluorobenzene 30

2.2.5 Infrared Multiphoton Exictaion of SF_6 34

2.3 Results and Discussion 36

2.3.1 Hexafluorobenzene 37

2.3.2 Sulfur Hexafluoride 41
2.4 Conclusion 43
2.5 References 45
2.6 Figures 48

Chapter 3. Photodissociation of Nitrobenzene at 266 nm.

3.1 Introduction 57
3.2 Experimental 60
3.3 Results and Analysis 62
3.4 Discussion 68
3.5 Conclusion 75
3.6 References 76
3.7 Tables 78
3.8 Figures 80

Chapter 4. A Methyl Radical Source.

4.1 Introduction 90
4.2 Source Design 92
4.3 The Radical Precursor - Azomethane 97
4.4 Azomethane Synthesis 100
4.5 Apparatus 101
4.6 Source Characterization 104
4.7 Beam Contaminants 108
4.8 General Tips 109
4.9 Conclusion 110

4.10 References.....111

4.11 Tables.....113

4.12 Figures.....114

4.13 Appendix.....122

4.13.1 References.....127

4.13.2 Figures.....128

Acknowledgements:

Graduate school has provided many challenges and I wouldn't have made over all the hurdles without the help of many people. First and foremost, I'd like to thank my research director Prof. Yuan T. Lee for his support and guidance throughout my graduate career. His love for science, dedication, and encouragement has been a constant source of inspiration.

I am grateful to Rick Brudzynski and Anne-Marie Schmoltner who first introduced me to molecular beam experiments, oxygen atom reactions and the B-machine. Under their tutelage I learned many of the details of running molecular beam experiments ranging from hard soldering and filament changing to branching ratio calculations. Anne-Marie was also a tremendous help during the last minute push to generate this thesis. The move from LBL down to campus was also a great learning experience. Thankfully the B-machine didn't stay on the LBL loading dock with the salvage sign on it for long.

A number of people helped out with the collisional deactivation experiments. Rick bridged the gap between our recent endeavors and past energy transfer campaigns. Initial photodissociation studies of C_6F_6 were carried out on the RSM with Anne-Marie Schmoltner and Eric Hintsa. John Allman assisted with revamping the B-machine for the hexaflourobenzene experiments. Tsong-Tsong Miau and Manfred Vodegel were a great help with sulfur hexafluoride experiments plus all the detector modifications. Hmm... I wonder when the helium liquefier will actually cool RIII. I also benefitted from many helpful discussions with Ken Patten, from the Johnston Group.

Finally, the last few experiments would not have been possible without Simon North's energy and enthusiasm. He had many good suggestions on how to improve the experiments and his willingness to "go to the bitter end" kept me going in the final stretch. I look forward to continuing our collaboration with the methyl radical photodissociation. This thesis would also be lacking in the figure department if it wasn't for his interest in AutoCAD.

In addition to B-machine co-workers many of the Lee group members were constant sources of valuable advice. Anne-Marie Schmoltner, Deon Anex and Kim Prather provided enlightening discussions regarding the nitrobenzene photodissociation studies. For the methyl radical source development, Jim Myers, Matt Cote, Deon Anex, Floyd Davis, Laura Smoliar, David Gonsavalez and Matt Lewin offered many useful suggestions. I am also indepted to Jim's computer expertise. His new and improved version of CMLAB2 minimizes the tedious aspects of fitting photodissociation data.

The Chemistry Department and LBL staff have provided friendly and efficient support and have been an invaluable resource. Harry Chiladakis, in particular, has been a great wealth of knowledge as well as a great friend. Under his guidance, the move down to campus went smoothly and he has kept Giauque Hall running smoothly ever since. I've learned a lot from many enlightening disscussions with Harry ranging from cryogenic pumping to more philosophical subjects such as where the world will be in several hundred years.

Ann Weightman's talent for working through the bureaucratic hurdles made it much easier for us to keep the science going. She also provided a great deal of moral support. George Weber, Andy Anderson and Ron Dal Porto of the Chemistry Department Machine Shop were instrumental in having the parts we needed built or fixed with minimal delay. With their good advice and many years of experience, I was also able to develop my machining skills. Thanks to Phil Simon, Matt McErlane, and Cliff Marshall we were able

to keep the KOCH liquefier running. I appreciate all the assistance I received from Tom Lawhead and Kathy Sigler in the Glass shop.

I'd like to extend my appreciation to all the members of the Lee group. In particular I enjoyed having Barbara Balko as a machine "neighbor". I admire her dedication to D atom campaign. One could always count on Matt Cote, Jim Myers, Bob Continetti and Gil Nathanson for sound advice. Matt has also provided lots of encouragement and greatly broadened my scientific horizons. James Chesko deserves great thanks for carrying on the responsibilities of managing the microVAX.

For life outside of lab, those camping trips to Yosemite, Shasta, Trinity Alps, Death Valley, Monterey and Whitney were refreshing and rejuvinating thanks to all my camping companions. Closer to Berkeley I owe a lot to many special friends Jane, Becca, Jackie, Jeff, and Dana who have contributed to my recreational side of life. Lou in particular has been a great friend throughout graduate school.

Lynda Beck, my high school chemistry teacher first initiated my interest in chemistry. In college, Prof. Geri Richmond provided my first opportunity to discover the joys and challenges of research. I'd also like to thank the Physics Dept. at Bryn Mawr College for adopting a Chemistry major.

My family deserve a lot of credit for this thesis. Their encouragement, support, and confidence in me throughout the years has been invaluable.

Finally, I would like to thank General Electric and Bryn Mawr College for financial support my first year of graduate school. I am also indebted to the American Association of University Women for support for my final year of studies. This work was supported by the Director, Office of Energy Research, Office of Basic Energy Sciences, Materials Sciences Division of the U.S. Department of Energy under Contract No. DE-AC03-76SF00098.

Chapter 1:

1.1 Introduction:

Following thermal, optical or chemical activation a molecule can relax via a number of pathways. For example, unimolecular reactions such as isomerization and dissociation compete with intermolecular processes including collisional energy transfer and reactive encounters. Traditionally, these elementary processes have been studied by measuring overall rate constants using bulk samples . The inherent averaged nature of the conventional "bulb" experiments, however, limit the microscopic information that can be obtained.

Molecular beam techniques, on the other hand, can provide extremely detailed information regarding the dynamics of molecular collisions. Velocity, angular divergence and initial internal state can be well defined. This allows control over the collision parameters and provides an opportunity to explore the internal state and translational energy dependence of inelastic and reactive encounters. The final velocity, angular and internal state distribution of the scattered products can be measured using a variety of techniques. From this information it is possible to ascertain how energy is distributed among the product degrees of freedom. This allows insight into the reaction mechanism: whether the reaction occurs through a long-lived complex or a direct mechanism. Additionally, the single collision conditions of crossed molecular beam

experiments permits the unambiguous identification of primary products. This is particularly essential in cases where highly reactive species, such as radicals, are used as reactants or are formed as products. The secondary collisions present in bulk studies often hinder primary product identification.

This thesis focuses on the collision dynamics of highly vibrationally excited molecules using crossed molecular beams techniques. Chapter 2 describes our endeavor to study the inelastic scattering of highly vibrationally excited polyatomic molecules with rare gases. Since collisional deactivation studies of large polyatomic molecules have been primarily "bulb" experiments, only averaged values of energy transferred per collision have been measured. By taking advantage of the single collision conditions and the well-defined energies of velocity selected and supersonic molecular beams more detailed information regarding the mechanism of vibrational energy transfer can be obtained.

Since unimolecular decomposition can compete with collisional energy transfer, a logical progression from these inelastic scattering experiments was to consider how a molecule excited above the dissociation threshold relaxes under collision free conditions. Studies on the photodissociation of nitrobenzene studies are described in chapter 3. With a UV photon, nitrobenzene can be excited well above the dissociation threshold for several reaction channels. The various primary product channels for unimolecular decomposition were identified and compared to those found in thermal decomposition studies.

It is important to mention some of the motivation for choosing to study the nitrobenzene photodissociation. This experiment was, in part, inspired by our group's long interest in phenoxy radical decomposition.[1, 2, 3] Since nitro-nitrite isomerization occurs readily,[4, 5, 6] photodissociation of nitrobenzene was thought to be a potential precursor of phenoxy radical. The formation of phenoxy radical was indeed found to be

an important primary product channel and this photodissociation experiment also provided the opportunity to study the secondary decomposition of phenoxy radical.

While chapter 2 considers the inelastic scattering of highly vibrationally excited molecules and chapter 3 explores the unimolecular decomposition of highly vibrationally excited molecules, an alternative relaxation scheme of highly vibrationally excited molecules is via reactive encounters. Recent cryogenic matrix experiments studying the light induced oxygen atom transfer from NO_2 to unsaturated hydrocarbons,[7] initiated our interest in reactions of highly vibrationally excited NO_2. In the reactive scattering of vibrationally excited molecules, the relative importance of reactant vibrational and translational energy in overcoming an endothermic energy barrier is of great interest.[8] For the crossed molecular beam experiments, a highly vibrationally excited NO_2 beam was crossed with a cyclohexene beam. Unfortunately, even with a collision energy over 50 kcal/mole and NO_2 internally excited to 53 kcal/mole, the high barrier for the reaction and the low cross section of molecule-molecule reactions made it difficult to study these systems with crossed molecular beams.

To try and overcome the low probability for the reaction, the orientation of NO_2 and cyclohexene in a "collision complex" by forming NO_2-cyclohexene dimers in a molecular beam was attempted. During this "half collision" experiment, the photo-initiated unimolecular decomposition channels can be studied. If the complex is in a favorable configuration, an oxygen atom transfer to cyclohexene can compete with predissociation of the dimer. In practice, it was difficult to characterize the dimer beam and confirm the existance of NO_2-cyclohexene dimers. Photodissociation studies showed no evidence for oxygen atom transfer to the hydrocarbon. Since these "hot" NO_2 systems are not presently amenable to studies with crossed molecular beams no further discussion was included.

Finally, the properties and reactions of polyatomic radicals have been also been a focus of chemical dynamic studies. These reactive species play key roles in combustion and atmospheric chemistry. Chapter 4 describes the design considerations, characterization, and optimization of a supersonic methyl radical beam source that has successfully generated an intense beam of methyl radicals. This source was built in preparation for a number of methyl radical studies including, the photodissociation of CH_3 as well as a number of reactive scattering experiments.

1.2 References:

1. A. M. Schmoltner, D. A. Anex and Y. T. Lee, *J. Phys. Chem.* (submitted).
2. R. J. Brudzynski, Ph.D. Thesis, University of California - Berkeley, 1987.
3. S. J. Sibener, R. J. Buss, P. Casavecchia, T. Hirooka and Y. T. Lee, *J. Chem. Phys.* **72**, 4341 (1980).
4. W. Tsang, D. Robaugh and W. G. Mallard, *J. Phys. Chem.* **90**, 5968 (1986).
5. A. L. Gonzalez, C. W. Larson, D. F. McMillen and D. M. Golden, *J. Phys. Chem.* **89**, 4809 (1985).
6. A. M. Wodtke, E. J. Hintsa and Y. T. Lee, *J. Phys. Chem.* **90**, 3549 (1986).
7. D. J. Fitzmaurice and H. Frei, *J. Phys. Chem.* **95**, 2652 (1990).
8. D. J. Krajnovich, Z. Zhang, F. Huisken, Y. R. Shen, Y. T. Lee, in *Physics of Electronic and Atomic Collisions* S. Datz, Eds. (North-Holland Publishing Company, 1982), pp. 733.

Chapter 2:

Collisional Deactivation of Highly Vibrationally Excited Molecules Using Crossed Molecular Beams

2.1 Introduction:

One of the most fundamental questions of molecular dynamics and chemical kinetics involves the details of intermolecular energy transfer pathways as internally excited molecules return to equilibrium. These energy transfer processes occur when excited molecules interact with other species in gas or in condensed phases. The direct experimental measurement of collisional energy transfer in the gas phase has been an active area of research for many years and has resulted in an understanding of energy transfer at low degrees of excitation.[1, 2] Despite its importance in a wide range of chemical reactions, much less is known about collisional energy transfer processes at high excitation energies. In this case, most of the studies have been limited to "bulb" type techniques where multiple collisions and extensive averaging severely limit the dynamical information obtained. To date, most experiments have been able to measure only $\langle \Delta E \rangle$, the average energy transferred per collision.[3, 4, 5] Only recent experiments have made it possible to gain more insight in the distribution of energy transferred and its energy dependence. [6, 7] For a complete understanding of these

processes, it is important to investigate how the initial vibrational energy of the donor molecule can be distributed among all the degrees of freedom (i.e. translation, rotation, as well as vibration).

A vast amount of work has been dedicated to understanding inelastic collision processes. The experiments described in this chapter focus on the vibration to translation energy exchange of highly vibrationally excited molecules in their ground electronic state. Presented here is a brief overview that concentrates on the relevant work that has been done in this particular area of intermolecular energy transfer, with an underlying emphasis on how a crossed molecular beams experiment can contribute to a far greater understanding of the energy transfer mechanisms. The goal of the experiments described in this chapter was to measure the actual distribution of energy transferred to translation upon a single collision by exploiting the well-defined conditions of molecular beam experiments. These experiments can help generate a uniquely detailed view of the energy transfer processes and thus lead to a more complete picture of the fundamental molecular dynamics.

2.1.1 The Master Equation:

The importance of collisional energy transfer has been recognized since 1922 when Lindemann first proposed the following three step mechanism for unimolecular reactions.

$A + M \rightarrow A^* + M$	k_1: activation
$A^* + M \rightarrow A + M$	k_2: deactivation
$A^* \rightarrow$ products	k_3: reaction

In the Lindemann-Hinshelwood mechanism, a reactant molecule can undergo two processes. It can gain or lose energy through collisions or, if it has sufficient energy,

unimolecular decomposition can compete with collisional deactivation. The reactant molecule A has an initial energy E' before collisions and some final energy E after colliding with a bath gas species M. Collisions occur with frequency, Z(E)[M], and the probability distribution function P(E,E') is used to describe the transition. The excited molecules can also react with a microscopic rate coefficient k(E). The following master equation has been developed to describe the change in the reactant molecule population, g(E,t):[8]

$$\frac{d}{dt}g(E,t) = [M]\int_0^\infty [Z(E')P(E,E')g(E',t) - Z(E)P(E',E)g(E,t)]dE' - k(E)g(E). \quad (1)$$

The master equation assumes that the discrete energy levels can be approximated with a density of states function. This is justified in the vibrational quasi-continuum, which occurs at high excitation levels.

The solution to the master equation requires knowledge of k(E), Z(E), as well as P(E,E'). Unfortunately, there is only a limited amount of experimental information available, regarding these parameters. The development of RRKM theory has allowed the straightforward calculation of k(E) based on the potential energy surfaces, the transition state configuration, and the molecular properties.[9] For experiments described here, the initial excitation remained low enough that no reactive channels were present. Therefore, the k(E)g(E) term in the rate equation was essentially zero.

In contrast to the single collision experiments, the choice of collision frequency in "bulb" experiments is not as clear cut but is critical in determining the correct transition probabilities. The extensive averaging in the thermal systems only allows the experimental determination of product $Z\langle\Delta E\rangle$, which is simply the rate coefficient for energy transfer. Different Z(E)'s and P(E,E')'s can be used to generate the measured rate coefficient. For example, the following two scenarios can result in the same overall energy transfer rate: a few collisions might each transfer a large amount of energy, or

many collisions may each transfer only a small amount of energy. Comparing the overall energy transfer rates can eliminate some of the problems created by the assigning a collision frequency to each system. It is important, however, to note the collision frequency used when comparing the values of $<\Delta E>$ reported for different experiments. It is generally accepted, from both experimental evidence and trajectory calculations, that the Lennard-Jones collision frequency is an appropriate reference collision number for collision partners that do not have strong dipole-dipole interactions.[10] The Lennard-Jones collision frequency for a given molecule a struck by molecule b is given by:

$$Z_{LJ} = N_b \sigma_{ab}^2 \left(\frac{8kT}{\pi\mu}\right)^{1/2} \Omega_{ab}^{(2,2)*}, \qquad (2)$$

where the mutual collision diameter is given by the collision diameters of the two gases with themselves by $\sigma_{ab} = \frac{\sigma_{aa} + \sigma_{bb}}{2}$.[11] $\Omega_{ab}^{(2,2)*}$ is the collision integral which includes parameters to describe the interaction potential and N_b is the concentration.

The transition probabilities, P(E,E'), have yet to be determined directly from experiment. There are two restrictions on the functional form of the P(E,E'). Since this model describes microscopic events, detailed balance of the forward and backward "reaction" must be maintained. The P(E,E'), as a probability function, must also be normalized. So far, $<\Delta E_d>$ and $<\Delta E_{all}>$, the average energy transferred for deactivating collisions and the average energy transferred for all collisions, have been the most accessible experimental quantities regarding the probability distribution function

$$<\Delta E_d> = \frac{\int_0^\infty (\varepsilon - E')\, P(\varepsilon, E')\, d\varepsilon}{\int_0^\infty P(\varepsilon, E')\, d\varepsilon} \qquad \text{for } \varepsilon < E \qquad (3.1)$$

and

$$<\Delta E_{all}> = \int_0^\infty (\varepsilon - E')\, P(\varepsilon, E')\, d\varepsilon \qquad (3.2)$$

Unfortunately, the measured energy transfer rates do not contain enough information to generate the actual form of the probability function. Typically a convenient functional form has been assumed for the P(E,E'). Popular functions include the strong collision, the step-ladder, and the exponential models. Assumed functional forms coupled with the $Z<\Delta E>$ measurements and the Z_{LJ} have been used to generate P(E,E') distributions.[4, 5, 12]

Clearly, a direct measurement of the probability distribution function is necessary to further our understanding of collisional energy transfer processes. Recently progress has been made along these directions.[6, 7] New techniques have made it possible to experimentally measure $<\Delta E^2>$ as well as $<\Delta E>$. More information regarding the actual shape of the population distribution during relaxation can be extracted from these direct measurements of $<\Delta E^2>$.[6, 13]

2.1.2 Collisional Energy Transfer Experiments:

The basic experimental scheme for collisional energy transfer studies includes the initial excitation or activation of the reactants followed by monitoring the energy transfer from those reactant molecules to the bath gas. There are a number of ways to detect the amount of energy transferred. In early experiments, indirect methods monitored the changes in unimolecular rate constants as a function of bath gases and pressures. This produced some qualitative information about the energy dependence of $<\Delta E>$. More recent direct studies have been able to make real time measurements of the energy decay in molecules. For example, UV and IR absorption and IR emission have been used to track the average internal energy of the excited molecules. Other techniques probe the translational energy increase in the bath gas. For example, photoacoustic, thermal lensing, and UV absorption by tracer gas have been used to measure the energy acquired

by the bath gas through collisions. Because there is a vast amount of work covering various aspects of energy transfer, only the work directly related to the molecular beam experiments described in this chapter (the collisional deactivation of C_6F_6 and SF_6 by rare gases) will be mentioned here. More thorough descriptions of other experiments, their results, as well as the theoretical work can be found in several comprehensive reviews by Tardy and Rabinovitch,[5] Quack and Troe,[12] Yardley,[1] Gordon,[14] and Hippler.[3] To date, no molecular beam energy transfer experiments with highly vibrationally excited molecules have been reported in the literature.

Time-resolved absorption and emission spectroscopy have recently been used to monitor the internal energy of highly vibrationally excited molecules, by a number of research groups.[4] In these techniques an initial narrow distribution of vibrationally excited molecules is obtained by exciting the molecules to a high electronic level. The electronically excited molecules subsequently relax, by internal conversion, to the highly vibrationally excited ground state. Depending upon the electronic transitions (and lasers) available, between ~40-150 kcal/mole of vibrational energy can be deposited into each molecule. The average energy transferred from the excited molecules is monitored by UV or IR absorption, or IR emission. These spectroscopic techniques provide information on the internal energy content of the molecule.

The time-resolved ultraviolet absorption technique has been applied to a number of systems including: cycloheptatriene, toluene,[15, 16] CS_2,[17] azulene,[18] CF_3I,[18] benzene,[19] and hexafluorobenzene.[20] The measured transient absorption spectra, coupled with an accurate calibration of the absorption cross section as a function of temperature, gives the time-dependent average internal energy. In the C_6F_6 and C_6H_6 studies, an exponential decay function was used to model the vibrational energy as a function of time, viz.

$$E(t) = E\,(E_o)\exp\left(\frac{-Zt}{N_\tau}\right) \qquad (4)$$

Lennard-Jones parameters were used to determine the collision frequency, Z, and $\Delta E(E)$ was found to be energy-dependent. The initial value $\Delta E(E_o)$, with 639 kJ/mole excitation, was estimated to be 2.35 kJ/mole for deactivation by argon. Argon was found to be 4-5 times more efficient at deactivating C_6F_6 than C_6H_6. This difference was attributed to the lower vibrational frequency of the C-F bond compared to the C-H bond.

The time-resolved spectroscopic measurements rely heavily on accurate calibrations of the absorption and emission of the vibrationally excited molecules. Typically, the calibrations are made by measuring the absorption or emission at various known levels of internal excitation. Extrapolation of this data is used to cover the inaccessible energy regimes. The difficulty in obtaining good calibrations has led to some controversy over the energy dependence of the energy transfer for large molecules. Results for several systems suggest that the energy transfer is independent of energy[3, 8, 15, 16, 18], while other experiments suggest there is a linear dependence on energy.[19, 20, 21, 22, 23, 24] More extensive studies show that there are other factors, in addition to the calibration curves, that contribute to the observed discrepancies.[3] There are two regimes that give different energy dependences of the energy transferred. At high initial excitation energies the energy transfer is independent of internal energy. In contrast, $\langle \Delta E \rangle$ becomes linearly dependent on internal energy at lower excitation levels. The turnover point of the energy dependence was found to be dependent on the size of the vibrationally excited molecules.

Another system extensively studied and pertinent to this work is the energy transfer in the SF_6 and argon system. Time-resolved optoacoustics has been used to measure the time constant for vibrational relaxation of SF_6 by argon as a function of the average initial excitation.[25] In contrast to the time-resolved spectroscopic measurements, optoacoustics, thermal lensing, and UV absorption of a tracer gas,

measure the rate at which the translational energy in the bath gas increases. For SF_6 and argon, the energy transfer rate is found to be linearly dependent on the initial internal energy for excitation between 4,000-19,000 cm^{-1} with $\frac{<\Delta E>}{<E>} = 4.1 \times 10^{-4}$. This is an order of magnitude lower than 3.7×10^{-3} found for C_6F_6.[20, 21] The difference in these values is likely to be due to the high symmetry of SF_6, which limits the vibration to rotation energy exchange.

Great strides in experimental techniques have made it possible to obtain more detailed measurements of collisional energy transfer processes. A population determination method, using fluorescence to track the collisional deactivation of nitrogen dioxide, is sensitive to the functional form of the P(E,E') used to fit the fluorescence signal.[7] For noble gas colliders, the energy transfer is found to be symmetric about the mean energy removed per collision and is best fit by a chopped gaussian function. Another new technique uses a kinetically controlled selective multiphoton ionization scheme to detect the transient population in an energy window below the initial excitation.[6, 13] The ion signal as a function of window energy and time has been used to directly obtain both $<\Delta E>$ and $<\Delta E^2>$ and their energy dependences. These experiments directly measure the width of the probability distribution function as well as the average value.

More recently time-resolved infrared diode laser probing was used to explore how the initial energy can be distributed among all the degrees of freedom (i.e. vibration, rotation, and translation) on the single collision time scale.[26] Two distinct mechanisms were found to be responsible for deactivating a highly excited donor molecule. In collisions with resonant vibration-vibration energy transfer between the donor and acceptor molecules, very small ($<1 cm^{-1}$) amounts of rotational and translation energy is exchanged. In an alternative deexcitation channel a large amount of energy is transferred directly to translation, $\Delta E_t = 500\ cm^{-1}$.

2.1.3 Energy Transfer Trends:

The energy transfer in systems with large molecules at high excitation is quite complicated. The energy transfer rate is a combination of vibration-to-translation transfer (V→T) and vibration-to-rotation (V→R) transfer for collisions between excited molecules and rare gas atoms. For collisional energy transfer with polyatomic buffers vibration-to-vibration energy transfer is an additional channel. For the general trends of vibration to translation energy transfer, it is helpful to look at simpler systems with low excitation. The basic energy transfer propensity rules and the experimentally measured rates for the various energy exchanges suggest that V↔T is the least efficient energy transfer process.

Most of the common theories describing direct vibration to translation energy exchange are based on one proposed by Schwartz, Slawsky and Herzfeld, the SSH model.[1, 2, 27, 28] The initial model considers the head on collision between a diatomic molecule and an atom, with an exponential intermolecular potential. This theory has been further extended to include a three-dimensional treatment for both diatomics and small polyatomics and has been used for quantitative comparison with experimental measurements. For collision energies within the thermal range, the basic models for energy transfer combined with experimental results have helped establish the following general set of propensity rules for V↔T energy exchange.

i) The probability of V↔T is generally very small, particularly when the collision time is longer than the vibrational period. In this case, the approaching atom only probes the average position of a rapidly fluctuating oscillator, therefore, direct V→T relaxation is unlikely. V→T transfer should be more

likely at the repulsive part of the potential where the Fourier components of the force are closer to the vibrational frequency.

ii) The probability for V↔T transfer decreases exponentially as the energy defect between vibration and translation increases. This is commonly known as the "exponential gap" law.

iii) The probability of molecules losing 2 or more quanta of vibration is smaller than for the $\Delta v=\pm 1$ process. $\Delta v=\pm 2$, $\Delta v=\pm 3$ processes become more probable as the initial internal energy of the molecule increases.

iv) Low frequency vibrations relax more readily than high frequency vibrations.

v) At higher oscillator excitation, the probability for a deactivating collision increases as $P_{v,v-1} = vP_{1,0}$, where $P_{v,v-1}$ denotes the transition probability from the v to v-1 state.

These general rules imply that the probability distribution function for energy transfer to V→T is likely to be strongly peaked at zero. At thermal collision energies, the typical collision time is an order of magnitude longer than the vibrational period. In contrast, the thermal collision time is closer to the impulsive limit for rotational energy transfer. Therefore, R↔T is a more efficient than V↔T. Experiments have shown that the V→T transfer rate can be up to four orders of magnitude lower than R→T and R→R at low excitation energies.[1, 2]

For large polyatomic molecules, at high initial excitation, the lack of realistic potential energy surfaces and the large number of collision parameters has made it difficult to obtain a detailed picture of the transfer mechanism. The propensity rules, determined for systems with low excitation, may be applicable to the high excitation case. The resonance criterion, however, is less restrictive with the greater density of states at

high excitation energies. An increased efficiency of energy transfer from the dense quasicontinuum at high energies compared to the sparse low-energy manifold has been experimentally observed.[3]

Trajectory calculations have been used to investigate the collisional energy transfer for polyatomic molecules colliding with noble gases. The calculations indicate that the internal energy of the molecule fluctuates during the collision time and strongly depends on the initial conditions of the collision.[3, 29, 30, 31] Using a large number of trajectories, the average energy transfer behavior is found to be best represented by an exponential probability distribution function:

$$P(E_f,E_i) \approx \frac{1}{\alpha+\gamma}\exp\left(-\frac{E_i - E_f}{\alpha}\right) \text{ for } E_f \leq E_i$$

$$\frac{1}{\alpha+\gamma}\exp\left(-\frac{E_f - E_i}{\gamma}\right) \qquad \text{for } E_f \geq E_i \qquad (5)$$

where the average energy transferred in activating collisions, γ, is less than the average energy transferred in deactivating collisions, α. The $P(E_f,E_i)$ for the deactivating collisions can also be represented by a biexponential function with a dominating contribution from "weak" collisions that transfer small amounts of energy and an additional component from "strong" collisions, which transfer large amounts of energy.[32]

To acquire a complete description of the vibrational relaxation mechanism(s), it is also important to consider the role of rotations in the deexcitation scheme. Vibrations and rotations are likely to be coupled during the collision and the efficiency of rotational energy transfer has been well recognized. The first model to explore the significance of rotations was proposed by Cottrell et. al.[28] and was later extended by Moore.[33] Calculations including the interaction between a classical rotator and a quantized vibrator showed that V→R energy transfer is important for a number of small molecules with small moments of inertia and low excitation energies. The vibrational energy of a

molecule may be transferred into the rotation of its collision partner, or into its own rotation. In the cases studied, the larger V→R coupling compared to V→T coupling was attributed to a faster rotational velocity than translational velocity, therefore the V↔R energy exchange is closer to the impulsive limit than V↔T.

The importance of V↔R energy exchange has also been noted in trajectory calculations of systems at high excitation energies.[30, 31, 34] Hippler, Schranz and Troe have made extensive simulations of argon colliding with SO_2 at various initial internal energies of both E_{vib} and E_{rot} and have calculated the state-specific rate coefficients. The results showed that an initially highly vibrationally excited but rotationally cold molecule will first gain rotational energy while it cools vibrationally. Then both the rotations and the vibrations relax as the system approaches thermal equilibrium. These findings suggest that the dominant deexcitation scheme is largely a V→R→T mechanism. Although the calculated rate constants are an order of magnitude higher than the measured values, due to the classical treatment of the vibrations,[35] these calculations provide a dynamical picture of the energy transfer mechanism.

The experimental results for the collisional energy transfer of highly vibrationally excited molecules show that $\langle\Delta E\rangle$ depends on many factors including the molecular parameters of the reactant and bath gases such as the number of vibrational degrees of freedom, the initial excitation, and the temperature of the system. A few general trends have been observed in the experimental results and will be discussed in the following paragraphs.

The $\langle\Delta E\rangle$ for reactant molecules of different sizes suggest that as the molecule becomes more complex $\langle\Delta E\rangle$ decreases for V↔T and possibly V↔R.[3] The opposite trend is true for the complexity of the bath gas. A comparison of the densities of states can be used to explain these trends. A larger reactant molecule can store the internal

energy more easily than a small reactant molecule. Similarly, a large bath gas molecule has more degrees of freedom to accept the energy, therefore more energy is transferred.

The average energy transferred per collision is strongly dependent on the internal energy of the molecule. At low energies where the vibrational state densities are low, $\langle\Delta E\rangle \propto \langle E\rangle^2$. As the vibrational state density increases, there is a linear dependence on energy. At high levels of excitation, the $\langle\Delta E\rangle$ becomes independent of E.[3] Small molecules with lower state densities demonstrate higher dependences on the initial excitation energy compared to larger molecules. This energy dependence has also been predicted by trajectory calculations and statistical models.[3]

Energy transfer studies have been done with a large number of collider gases. For rare gas buffers, the tabulated data[3, 4, 5, 7] show that $\langle\Delta E\rangle$ is only slightly dependent on the size of the rare gas. $\langle\Delta E\rangle$ is between 50-100 cm^{-1} for triatomic reactant molecules with $\langle\Delta E\rangle$ typically increasing from helium to xenon. $\langle\Delta E\rangle$ is usually smaller for helium, while the values for neon, argon, krypton and xenon are quantitatively similar. Large reactant molecules follow the same trend in $\langle\Delta E\rangle$ with only a small increase in the magnitude to $\langle\Delta E\rangle$=50-250 cm^{-1}. Molecular buffer gases are more efficient colliders with the additional V-V exchange channel. Correlations of $\langle\Delta E\rangle$ with various molecular collider properties can be found in the review by Tardy and Rabinovitch. [5]

The translational energy dependence of the energy transfer can be used to distinguish what types of interactions are important. If the attractive part of the potential is responsible for the energy exchange, $\langle\Delta E\rangle$ will decrease with increasing translational energy. On the other hand, if the repulsive part of the potential is responsible for energy transfer, the opposite trend occurs. Temperature dependence studies, using laser heating and shock waves, indicate that there is no large variation in $\langle\Delta E\rangle$ in the accessible temperature ranges.[35, 36] $\langle\Delta E\rangle \propto T^n$ with $n=0\pm1$ between room temperature to

~10^3K. Rare gases tend to show a stronger positive temperature dependence than the polyatomic buffer gases.[3]

Another area of interest is the V→T energy transfer at very low collision energies (1-100 cm^{-1}), where large cross sections and mode specific energy transfer have been observed for low vibrational excitation.[37, 38] Several mechanisms have been used to explain these results. T→V excitation increases with E_{trans}. From microscopic reversibility, the V→T deexcitation process should become more important as E_{trans} approaches zero and a negative V→T temperature dependence is expected. The role of quantum mechanical resonances contributing to enhanced V→T deexcitation has also been the subject of some debate. Calculations suggest that the resonances increase the energy transfer cross sections at very low energies (0.1 cm^{-1}) and that only the attractive forces should be responsible for the energy transfer at the collision energies observed.

Although there are many extensive studies which measure the overall rates of energy transfer for various systems, it's important to emphasize that more experiments are necessary to learn more about the functional form of the P(E,E') and the degrees of freedom important in the relaxation. Crossed molecular beam experiments can help resolve some of these remaining questions.

2.1.4 Crossed Molecular Beams and Inelastic Scattering Experiments:

There are two major goals of using the crossed molecular beams method for studying inelastic collision processes. The first is to unravel the mechanism(s) responsible for the energy transfer between the different degrees of freedom. The second is to learn about the parts of the interaction potentials that are responsible for the energy transfer. In inelastic scattering experiments of highly vibrationally excited molecules in

the ground electronic state, it is possible to directly measure the velocity distribution of the scattered products by time-of-flight techniques. Changes in the translational energy, measured in the time-of-flight spectra, can be directly converted to the probability distribution function for the V-T energy transfer in the center-of-mass frame. This was the main objective of the experiments described in this chapter.

An advantage of the crossed molecular beam technique is the fact that the particles undergo only one collision when crossing the interaction region. Therefore the collision dynamics can be studied without the interference of multiple encounters which can severely complicate the results. Using velocity selectors or the seeded beam technique, it is straightforward to control the collision conditions and to obtain a translational energy dependence of the inelastic processes. A comparison of effusive beams, which have a thermal rotational population distribution, with supersonic beams, where the rotational distribution is cooled by the expansion, can also be used to investigate the role of rotational energy in the scattering. One can also obtain the angular dependence of the energy transfer by using a molecular beam apparatus equipped with two fixed sources combined with a rotating detector. These features of crossed molecular beams experiments offer a unique opportunity to study the detailed mechanisms for energy transfer.

Molecular beam techniques have been used to study inelastic collisions at low vibrational energies. A variety of detection methods have been used including product velocity analysis and laser induced fluorescence. With optical detection methods, one can directly probe the final vibrational and rotational state distributions of the scattered products and can detect low levels of energy exchange. One great limitation of these techniques, however, is the requirement that the monitored species must have an optical transition within the wavelength range of a tunable dye laser. The universality of an electron bombardment and mass spectrometer detector combined with product velocity

analysis, on the other hand, makes it possible to study an unrestricted range of molecules.

In inelastic scattering experiments, where the product masses remain identical to the reactant masses, the final velocity in the center-of-mass frame (CM) is dependent on the energy transferred, ΔE, to or from the translational degree of freedom by:

$$u'_1 = u_1\left(1 - \left(\frac{\Delta E}{E_{tr}}\right)\right)^{1/2} \qquad (6)$$

where u_1 is the initial CM velocity, u'_1 is the final CM velocity and E_{tr} is the initial translational energy. ΔE is the collision induced change in the internal energy. For a deactivating collision, internal energy is released to the translational degree of freedom and ΔE has a negative value. An example of a Newton diagram with the velocities in both the laboratory and center-of-mass frame for a deactivating collision is shown in figure 2.1.

The velocity resolution of the apparatus is the limiting factor of the translational energy exchange method. To maintain a high resolution experiment, the two colliding beams must have well-defined velocities and angular distributions. It is possible to resolve the inelastic transitions with a long flight path between the collision zone and the detector. Of course, this resolution is achieved at the expense of the signal to noise ratio. The resolution is also dependent on the initial collision energy and ΔE. At higher collision energies, it is more difficult to resolve small changes in translational energy for the same given flight length. With this method, it is also difficult to distinguish between different types of inelastic processes which give rise to the same amount of translational energy gain or loss. For example it is not always possible to determine whether V$\leftrightarrow$T or R$\leftrightarrow$T exchanges are responsible for changes in the time-of-flight spectrum.

Crossed molecular beam experiments have made many significant contributions to our understanding of inelastic processes at low vibrational energies. Not surprisingly, the majority of these experiments have focused on rotational energy exchange, one of the

most effective inelastic processes. The differential cross section measurements obtained for rotational energy transfer in hydrogen and some small molecule systems, together with progress in the theoretical descriptions, have led to a much clearer picture of these processes.[39] On the other hand, less is known about the vibrational energy transfer mechanisms. These processes have cross sections usually a factor of 10^2-10^3 smaller than rotational energy transfer due to the larger energy gaps and weaker coupling processes. Well-resolved experiments on vibrationally inelastic processes have been performed predominantly with ions.[40] In this case, it is simpler to control and resolve the ion beam energy. Additionally, it is easier to accelerate an ion beam and to get the high collision energy necessary for vibrational excitation. Only a few experiments based on the velocity analysis methods are available for vibrational excitation in neutral particle collisions.[41] Typically, the experimental resolution is not good enough to resolve the inelastic processes, therefore, it is difficult to distinguish between vibrational and rotational channels. Review articles by Krajnovich et. al.[40] and Gordon[14] give more complete descriptions of the recent single-collision energy transfer experiments.

Crossed molecular beam investigations of the inelastic scattering of highly vibrationally excited molecules using the translational energy exchange method have been ongoing in the Lee group for several years.[42] The goal of these experiments was to elucidate the vibrational deexcitation mechanisms by measuring the distribution of energy transferred from vibration to translation. This would clarify whether the bulk rates of vibrational deexcitation represent a situation where a few collisions each transfer a large amount of energy or one where many collisions each transfer only a small amount of energy to translation.

Since the collision efficiency for V↔T transfer depends strongly on the lowest vibrational frequency ν_{min} and increases as ν_{min} decreases[1], large molecules with many low frequency modes were used rather than simple diatomics, that have only one

vibration at high frequency. To enhance the likelihood of V↔T energy transfer, conditions were chosen to exaggerate the disparity between the vibrational energy of the molecular beam and the collision energy. The molecular beam was excited with a laser to a vibrational temperature, ~3000K. The translational temperature of the collision was kept much lower, ~250K, by using a velocity selected effusive source for the molecular beam and a liquid nitrogen cooled atomic beam source.

The earlier experiments used two different methods to form the excited molecular beam.[42] One attempt utilized the 515 nm and 488 nm radiation from an argon ion laser to electronically excite azulene. The azulene subsequently isomerized and relaxed to the vibrationally excited ground electronic state of naphthalene via internal conversion. The 18 Watt output of the CW argon ion laser was focussed to a 2 mm diameter spot size and reflected by mirrors to generate 10 passes across the molecular beam. Even with the multi-pass configuration, it was estimated only ~1.5% of the molecular beam was excited and no differences in the time-of-flights were detected for the laser on (excited molecules) and laser off (unexcited molecules) experiments.[43]

The second experiment used the 266 nm output from a Nd:YAG laser to excite 1,3,5-cycloheptatriene and 7-isopropyl-cycloheptatriene. Brudzynski and co-workers found that the highly vibrationally excited cycloheptatrienes isomerized to form toluenes. It was originally hoped that these highly vibrationally excited alkyl substituted benzenes could be used in the collisional deactivation experiment. This series of experiments showed, however, that the hot toluenes subsequently decomposed with a lifetime on the order of 10 μsec. Since the transit time across the 2 x 2 x 3 mm collision volume for a typical beam velocity of 5×10^4 cm/s is ~10 μsec, a large fraction of excited cycloheptatriene would dissociate as it crossed the interaction region. It was concluded that the excited cycloheptatrienes are likely to dissociate long before they reach the

detector, therefore, they would not be feasible molecules for the collisional deactivation studies.

In the series of experiments reported in this thesis, hexafluorobenzene (C_6F_6), excited with a UV photon, and sulfur hexafluoride (SF_6) excited by infrared multi-photon excitation (IRMPE) techniques, were used to explore the collision dynamics of highly vibrationally excited molecules. With these molecules and excitation schemes, it was possible to excite a larger fraction of the molecular beam than in the previous experiments; it was therefore more feasible to detect small changes in the translational energy with these systems.

2.2 Experimental

2.2.1 Apparatus:

The following experiments were designed to measure the distribution of energy transferred to the translational mode in a single collision encounter. A beam of highly vibrationally excited molecules in their ground electronic state was generated using various laser excitation schemes. This beam was then crossed with a translationally cold rare gas beam. Time-of-flight of the scattered particles, using a "universal" electron bombardment ionizer and mass spectrometer detector, were measured as a function of laser excitation. Changes in the scattering as a result of the additional vibrational energy were monitored by comparing the time-of-flight spectra of the scattered molecules with the laser on and with the laser off.

These experiments were performed with a crossed molecular beams apparatus that has been described in detail previously.[44] The apparatus, shown in figure 2.2, consisted of two differentially pumped beams crossed at 90° in the main vacuum chamber

which was maintained at ~1x10^{-7} Torr. A triply differentially pumped detector, consisting of an electron impact ionizer, [45] a quadrupole mass spectrometer, and a Daly type ion detector [46] measured the products. The detector could be rotated in the plane of the two beams and about the 2x2x3 mm collision volume. Time-of-flight spectra of the scattered molecules were measured by triggering the counting electronics off of pulses from the velocity selector chopper wheels. Several modifications were made, throughout the course of these experiments, to further improve the signal to noise ratio and to accommodate the laser needed for the excitation of the molecular beam.

The details of the laser excitation schemes used to prepare the vibrationally excited C_6F_6 and SF_6 beams are described in a later section. A variety of conditions were used to prepare the molecular beam. In the initial studies, an effusive beam coupled with a velocity selector was used to maintain low and well-defined collision energies. The effusive source consisted of a tube with a 0.030" x 0.040" aperture with ~1 Torr backing pressure. The beam then passed through a differential pumping region which was defined by two 0.050" x 0.060" apertures located 1.00" and 3.75" from the source. The resulting beam had a 2° angular divergence.

The velocity selector, mounted in the differential pumping region, consisted of two 7.0" diameter and 0.040" thick aluminum alloy wheels. Each wheel had two slots 0.080" wide and 0.30" deep and 180° apart. The wheels were milled down at the slots to obtain a knife edge to minimize the reduction in transmission due to the wheel thickness. The velocity selector assembly was mounted with two bearings and connected to a three phase motor by a flexible coupling shaft. The relative orientation of the wheels, the distance between the wheels, and the wheel frequency were adjusted to transmit the desired beam velocity and velocity spread. The resolution of a mechanical velocity selector is given by $\Delta v/v=l/d$ where l is the slit width and d is the offset distance of the two slits. For room temperature effusive beams of C_6F_6 and SF_6, the peak velocities

were ~$2x10^4$ cm/sec. The wheels were offset by 13°, positioned 1.54" apart, and spun at 185 Hertz to transmit the peak velocity and obtain a $\Delta v/v$ of 0.1.

A slotted optical switch containing an LED and photodiode was mounted at the back velocity selector wheel assembly to monitor the frequency of the wheels and the timing of the modulated molecular beam. Since there were two slots in the wheels, the velocity selector generated a 400-800 Hz chopped beam and trigger pulse. The maximum laser repetition rate was 100 Hz, therefore, the velocity selector pulses were divided by an appropriate factor before sending the pulses to trigger the laser and the ion counting electronics. See figure 2.3 for an illustration of the timing schematics. A variable time delay generator was adjusted so that the laser fired when the molecular beam pulse was at the laser interaction volume. To set the timing electronics, the on axis beam time-of-flight was monitored while using high laser powers to dissociate the molecular beam by multiphoton processes. The laser trigger time delay was then adjusted to give the largest depletion signal in the on axis beam time-of-flight.

A supersonic beam source accompanied by laser excitation was used to investigate the collision dynamics of vibrationally hot but rotationally cold molecules. A nozzle with a 0.006" aperture and ~400 Torr backing pressure was used for this beam source. Since the velocity distribution of the supersonic beam is significantly narrower than that of an effusive beam, the velocity selector was no longer necessary. Only one wheel in the primary differential region was used to modulate the beam and trigger the laser and counting electronics. This permitted the source to be moved closer to the collision region, significantly increasing the number density at the collision region. See for example figure 4.4.

The laser/molecular beam interaction region was located 1.90" from the collision zone. With the 0.080" velocity selector slit widths, the 0.060" high defining apertures, and the wheel spinning at 200 Hz, the resulting chopped molecular beam was ~35μsecs

to reduce the beam background in the main chamber. With a $2x10^4$ cm/sec beam velocity, the corresponding beam pulse was ~6mm long. In order to radiate a large fraction of the molecular beam pulse, a wide laser spot was maintained to generate a significant overlap between the two beams. For the UV excitation, the output from a Lambda Physik Excimer laser was typically focused to a 5mm wide by 3mm tall rectangle with a Suprasil lens. For the infrared multiphoton excitation scheme, the output of the Lumonics CO_2 laser was focused to a 4x4 mm spot with a ZnSe lens. A variety of other wheel slits, defining slits, and laser spot sizes were used to further improve the laser beam/molecular beam overlap. The transit time between the laser/molecular beam interaction point and the collision zone was ~250μsec. This allowed time for the dissociation fragments, of any molecules that absorbed more than one UV photon (or enough infrared photons to pass the dissociation threshold in the IRMPE case), to recoil out of the beam before the beam pulse reached the collision zone.

To improve the signal to noise ratio and increase the chance of detecting small amounts of energy transfer, the continuous supersonic beam source was replaced by a pulsed molecular beam source. A piezoelectric translator based pulsed valve[47, 48] was set to generate a 100 μsec FWHM beam pulse with a 100 Hz repetition rate. With this configuration, the duty cycle of the pulsed beam was one percent of a continuous beam. As shown above, only a small fraction of a continuous molecular beam is excited and transmitted by the chopper wheel. The 100μsec long pulses reduced the portion of the beam blocked by the chopper wheel. The short pulses also permitted an increase in the number density of the transmitted beam, therefore the source pumping speed was used more effectively. In this case, the laser and counting electronics ran at 50 Hz to obtain the laser on vs. laser off spectra.

The secondary beam was produced by expanding ~500 Torr of neon, argon, or xenon through a 0.006" aperture. The beam was defined to a 1.5° full width half

maximum angular divergence with a 0.020" diameter stainless steel conical skimmer 0.400" from the source. The source was attached to a copper block which could be cooled by liquid nitrogen as well as heated by a series of coaxial heating elements. The velocity of the atomic beam could be varied by controlling the temperature of the nozzle tip. The beam temperature was monitored by a Chromel-Alumel thermocouple clamped to the nozzle tip. As shown in figure 2.2, only one region of differential pumping for the atomic beam was used for the majority of these experiments.

The mechanical velocity selector (or chopper wheel in the supersonic beam case) determined the timing for the entire experiment. The flight lengths were calibrated with supersonic rare gas beams with known velocities. The time-of-flight signal at the parent and fragment masses of the primary beam was monitored to examine the vibration to translation energy exchange as a function of laser excitation. There were two advantages of tracking the molecular beam rather than the rare gas beam. First, this beam was less intense than the atomic beam, therefore the chamber background at the corresponding masses was significantly lower. Secondly, since the center-of-mass recoil velocity is inversely proportional to the mass, the heavier molecules scatter with a smaller CM velocity concentrating the products in a smaller area.

2.2.2 Background Reduction:

In crossed molecular beams experiments, there are two sources of background: the inherent background in the detector and the background caused by the molecular beam gases. This second background source is particularly significant in elastic and inelastic scattering experiments where the product fragment ions match those of the initial beam. In this case, the mass spectrometer can not be used to separate the products from the reactants and there is a large contribution to the background due to the beams. The

detector slits must be perfectly aligned to detect the scattered products, therefore, molecules that are directed straight through the detector slits determine the background in the detector at the beam masses. With the main chamber pressure held at $2x10^{-7}$ Torr, the molecular mean free path is larger than the dimensions of the chamber, therefore the "straight through" molecules are generated from surfaces viewed by the detector .

In order to reduce the wall reflected background, cryopumping panels were fabricated for the main chamber as shown in figure 2.2. The copper heat exchanger was made by soldering flattened 3/8" copper tubing to a 1/16" thick copper plate. To minimize the heat exchange between the cryopanel and the warm surfaces of the chamber, the cryopanel was mounted to the differential wall with fiberglass standoffs. Needles soldered to the panel were also used for further isolation. This insured that if the cryopanel shifted during cooling, large surface areas still would not come in contact with the warm differential wall. The cryopanel dimensions were chosen so that the detector viewed only cold surfaces, except when the detector was within 15 degrees of the molecular beams. Cooling was achieved by circulating ~10K helium, generated by a Koch closed cycle helium refrigerator, through the copper tubing. The addition of the cryopanel reduced the background count rates by a factor of 10-20, depending on the molecular masses. A similar smaller cryopanel cooled by a Air Products closed cycle cryopump was extensively used in recent reactive scattering experiments on the B-machine[49].

Another cryopanel was installed in the primary differential region to increase the pumping speed of the differential chamber. This was particularly helpful in decreasing the main chamber background when the velocity selector and pulsed valves were used in the differential region. This cryopanel reduced the slow effusive background that was generated due to pressure building up just behind the differential wall defining slit.

Additional modifications were underway throughout these projects to enhance the sensitivity of the crossed molecular beams machine. Three Seiko-Seiki STP-400 magnetically-suspended turbomolecular pumps with 300 l/sec pumping speed replaced the ion pumps on each of the three differential pumping regions of the detector. The three magnetically-suspended pumps were backed by a Leybold Heraeus grease-sealed turbomolecular pump followed by an Edwards 63/150 diffusion pump with a 135 l/s pumping speed at $5x10^{-8}$ Torr. Finally, a 1397 Sargent Welch mechanical pump backed the entire system.

To further increase the pumping speed in region three of the detector another, cryopanel, in addition to the existing liquid nitrogen cooled copper dewar, was installed in the ionization region.[50] This second cryopanel will be cooled by liquid helium generated by a high pressure expansion of cold helium through a Joule-Thompson valve located in a vacuum insulated dewar on the top of the rotating detector. The cold helium will be generated by the Koch closed cycle helium refrigerator adjacent to the crossed molecular beam chamber. To protect the liquid helium cooled cryopanel from the 10 Watts of heat generated by the ionizer filament, an extra copper chevron baffle was attached to the existing liquid nitrogen cooled copper cold shield. Although not used in the experiments reported here, this new cryopanel should significantly increase the sensitivity of the detector.

2.2.3 The Vibrationally Excited Molecular Beam:

The two potential methods available to us for forming a highly vibrationally excited molecular beam included electronic excitation followed by internal conversion to the vibrationally excited ground electronic state and infrared multiphoton excitation. Ideally, one would like to prepare a molecular beam with a well defined internal energy,

therefore, the first method is more attractive than the latter. With the second method, however, it was easier to excite a higher percentage of the molecular beam. Both of these techniques have been used extensively in many collisional deactivation studies. This next section describes the characterization of the excitation as well as some of the problems encountered. Recently, with the significant advances and greater availability of lasers, new techniques including stimulated emission pumping (SEP) make it more feasible to generate molecular beams with higher concentrations of vibrationally excited molecules and with greater selectivity of the initially prepared state. These advances will allow the opportunity to explore the effects of vibrational energy in both inelastic and reactive scattering mechanisms in the near future.

2.2.4 UV Excitation of Hexafluorobenzene:

Since it is most desirable to have a well-defined internal energy exciting the molecular beam via electronic excitation using one UV photon and allowing the molecule to internally convert to the ground electronic state was by far the most appealing of our options. The spread in the internal energy is essentially only the Maxwell-Boltzmann spread in the initial internal energy of the molecular beam at 300K before the excitation. Typically, a room-temperature thermal distribution has a half-width of a few hundred wavenumbers. The spread in the photon energy is insignificant compared to the spread in the beam energy and the final distribution is a near-delta function.

Hexafluorobenzene was the initial candidate for the UV excitation scheme. C_6F_6 has a high absorbance at 248 and 193 nm, 300 $M^{-1}cm^{-1}$ and 5160 $M^{-1}cm^{-1}$ respectively.[20] These transitions result from a $\pi\ (1e_{1g}) \rightarrow \pi^*(1e_{2u})$ electron promotion to obtain the excited B_{2u} (at 248nm) and B_{1u} (at 193nm) singlet states. [51] Small quantum yields for fluorescence (0.02), intersystem crossing (0.05), and isomerization

to the fulvene isomer (0.08), as well as the short fluorescence lifetime imply that internal conversion to the ground electronic state occurs very efficiently. [52, 53, 54] With the high pulse powers available at 248 nm and 193 nm from a Lambda Physik excimer laser, it should be possible to excite a large fraction of the molecular beam compared to the azulene, as previously discussed. C_6F_6 has also been used for several collisional deactivation studies.[20, 21, 55]

One factor that limits the number of molecules one can excite with UV photons is the high probability of multiphoton absorption. A continuous band has been observed for the UV absorption spectra of a number of highly vibrationally excited molecules, ranging from diatomics and triatomics such as Cl_2, CS_2, and SO_2, to large polyatomics such as benzene, hexafluorobenzene, toluene, cycloheptatriene and azulene.[18, 56] This broad feature can be attributed to either of two possible mechanisms: the absorption is continuous and/or the large number of hot bands generates a highly congested spectrum. Experimental calibrations of the UV absorption spectra as a function internal energy has been an central part of many direct energy transfer investigations. When the absorption cross section shows a pronounced temperature dependence, it can be used as a fast "thermometer" to measure the changes in the internal energy of the excited molecules. The temperature dependence of the UV absorption spectra have been successfully exploited for monitoring the collisional deactivation in many of the bulb type experiments. In our crossed molecular beam experiments, however, the large photon absorption cross section of the highly vibrationally excited molecules severely limits the percentage of molecules that can be prepared by UV excitation. Unfortunately, this increased the difficulty of detecting events with small collision cross sections.

To obtain conditions where the largest percentage gain in excited hexafluorobenzene is expected, it was necessary to estimate the absorption cross section for the second photon. Theoretical predictions of the temperature dependence of UV

absorption spectra of large polyatomic molecules is difficult since little is known about the details of the excited states. For simple diatomics the temperature dependence has been estimated by the Franck-Condon principle.[57] With increasing temperature and the subsequent increase in population in the higher rovibrational states, the absorption coefficient tends to decrease at the maximum of the absorption band while it increases at the wings. This trend for diatomic molecules has been described with a simple analytical formula by Sulzer and Wieland: [58]

$$\varepsilon(\nu,T) = \varepsilon_0^{max}\sqrt{\tanh(\theta/2T)}\,\exp[\tanh(\theta/2T)[(\nu-\nu_0)/\Delta\nu_0]] \qquad (7)$$

where ε_0^{max} is the maximum absorption coefficient at 0K, ν_0 is the origin of the electronic transition in cm^{-1} at 0K, $\Delta\nu_0$ is the spectral width of the electronic transition, and θ is the characteristic temperature of the vibration inducing the spectral broadening.

It has been found that the temperature dependences of UV absorption spectra for polyatomic molecules behave similarly to those of diatomic molecules. Experimentally determined temperature dependences of the UV spectra have been successfully simulated by a modified version of the Sulzer-Wieland model for several large polyatomic molecules. Therefore, the results from the Sulzer-Wieland model should give us a reasonable estimate for the second photon absorption cross section.

Yoshihara and co-workers[20] compared their observed transient absorption spectra of hexafluorobenzene after 193 nm excitation to a simulated spectrum using a modified version of the Sulzer-Weiland model with the following formula:

$$\varepsilon(\nu,T) = \varepsilon_0^{max}\sqrt{\tanh(\theta/2T)}\,\exp[\tanh(\theta/2T)[(\nu-\nu_0(T))/\Delta\nu_0]^2\nu/\nu_0(T)] \qquad (8)$$

where, $$\nu_0(T) = \nu_0 - \theta(k/hc)[\exp(\theta/T)-1]^{-1} \qquad (9)$$

and θ, ν_0, and $\Delta\nu_0$ have the same assignments as in equation (7). This modified model includes the band origin as a function of temperature, $\nu_0(T)$, to account for the red shift

observed in the excited spectra. θ was treated as an adjustable parameter. The total absorption coefficient is given by:

$$\varepsilon(\nu,T)=\varepsilon_1(\nu_1,T)+\varepsilon_2(\nu_2,T) \qquad (10)$$

ε_1 represents the $^1B_{1u}\leftarrow {}^1A_{1g}$ transition centered at ν_0=50,000 cm^{-1} with ε_{1max}=5,000 $M^{-1}cm^{-1}$. ε_2 represents the $^1E_{1u}\leftarrow {}^1A_{1g}$ transition centered at ν_0=57,400 cm^{-1} with ε_{2max}=47,000 $M^{-1}cm^{-1}$. $\Delta\nu_0$ was assigned 1900 cm^{-1} for both of these transitions. Assuming there is a complete redistribution of the electronic energy to vibrational energy after the 193 nm excitation, the final vibrational temperature of the hot hexafluorobenzene is 3050K. Yoshihara et. al. obtained excellent fits to their observed t=0 transient absorption spectra after 193 nm excitation of hexafluorobenzene with θ = 135 K. The absorption of the hot C_6F_6 is attributed to the $^1E_{1u}\leftarrow {}^1A_{1g}$ transition which becomes accessible with the additional vibrational energy. The $^1E_{1u}\leftarrow {}^1A_{1g}$ transition has a cross section an order of magnitude larger than the cross section for the $^1B_{1u}\leftarrow {}^1A_{1g}$ transition. The latter is a symmetry forbidden transition for the D_{6h} point group.

We used this modified Sulzer-Wieland model to estimate the transient absorption cross section for a second photon following 193 and 248 nm excitation. In the later case the vibrational temperature of the hot hexafluorobenzene was assumed to be 2400K, the energy of a 248 nm photon plus the initial vibrational energy of C_6F_6 at 300K. The absorption cross section for a second 193 nm photon was approximately 7,500 $M^{-1}cm^{-1}$ while the absorption cross section for a second 248 nm photon was approximately 1,500 $M^{-1}cm^{-1}$. Both of these values are significantly larger than the initial cross sections for the unexcited C_6F_6. Therefore, once C_6F_6 has absorbed one photon, there is a high probability it will absorb a second photon. With two 193 nm or two 248 nm photons (296 and 230 kcal/mole), C_6F_6 is likely to dissociate. To minimize the multiphoton effects, it was necessary to maintain the laser at low powers, ≤25 mJ/cm^2. Under these conditions only ~10% of the molecular beam could be excited.

For the present work, the C_6F_6 beam was excited with 248 nm and 193 nm photons from a Lambda-Physik excimer laser running KrF and ArF. The laser molecular beam interaction region was located 1.90" from the collision center to allow time for dissociation fragments to recoil out of the beam. Photofragmentation translational spectroscopy was used to check for multiphoton effects. For these photodissociation experiments, the laser molecular beam interaction center was moved to the detector's center of rotation in the main chamber. With laser powers ≥25 mJ/cm^2, a significant amount of signal at mass-to-charge ratios corresponding to CF_2^+ and $C_5F_3^+$ was observed 15° away from the beam. Isomerization to a fulvene form of benzene followed by cleavage of the C=C bond, to form CF_2 and C_5F_4, is likely to be the main dissociation channel. Power dependences of the $C_5F_3^+$ signal at 15° showed that C_6F_6 dissociates through a multiphoton process.

2.2.5 Infrared Multiphoton Excitation of SF_6:

Infrared multiphoton excitation is an alternative technique for generating a vibrationally excited beam. Unlike the internal conversion method, infrared multiphoton excitation prepares excited molecules with a distribution of vibrational energy. A model, based on experimental results, has been developed to describe the multiphoton excitation mechanism and the final excited distribution of molecules.[59] There are three distinct stages in the excitation process. First, a polyatomic molecule, with low initial internal energy and therefore a low density of states, must be excited over the discrete region. This is accomplished by a near resonant absorption of 3-6 infrared photons in a single vibrational mode. At higher internal energies, the density of states and intermode coupling increase to the extent that the energy states form a quasi-continuum. Excitation at this level can continue through stepwise resonant transitions. At energies above the

dissociation limit, where the energy is statistically randomized, the molecule dissociates at the unimolecular decomposition rate given by RRKM theory. In the first region, the excitation is dependent on the laser intensity, while in the quasi-continuum, the excitation is determined by the laser fluence.

The rate equation for the infrared excitation is given by:

$$\frac{dN_m}{dt} = \frac{I(t)}{h\nu}\left(\sigma_{m-1}N_{m-1} + \frac{g_m}{g_{m+1}}\sigma_m N_{m+1} - \left(\frac{g_{m-1}}{g_m}\sigma_{m-1} + \sigma_m\right)N_m\right) - k_m N_m \quad (11)$$

where N_m is the normalized population in level m at energy mhν, I(t) is the laser intensity, g_m is the density of states of level m, σ_m is the absorption cross section from level m to level m+1, and k_m is the dissociation rate constant from level m.[59] To account for the intensity dependent excitation over the initial discrete levels of SF_6 an additional term, dependent on $I^3(t)$ was included in equation 11. This assumed that a single, three photon process excited molecules in the J^{th} rotational level of the ground vibrational state to the quasicontinuum.

For our collisional deactivation experiments, it was important to excite a large fraction of the beam with the peak of the final distribution centered just below the dissociation limit. This required a high peak laser intensity to excite a large percentage of SF_6 out of the discrete states with a low laser fluence to maintain the excited distribution below the dissociation threshold. A computer algorithm, to model the multiphoton dissociation of SF_6 [60], was used to estimate the distribution of excited SF_6 as a function of laser power and the Lumonics CO_2 laser pulse profile. At 3 J/cm^2, 10% of the beam was excited over the dissociation threshold and dissociated before reaching the collision zone. Approximately 50% of the remaining beam was excited out of the ground vibrational state. The excited distributions for a number of laser powers is shown in figure 2.4

In the actual experiments, the Lumonics CO_2 laser was tuned through the ν_3 resonance of SF_6 using the laser lines between 935 cm^{-1} to 953 cm^{-1}. As in the C_6F_6 experiments, the laser/molecular beam interaction center was 1.90" from the collision zone to allow dissociation products time to recoil out of the beam. The time delay was optimized at high laser powers to give the largest SF_5^+ ion depletion. (SF_5^+ is the major fragment ion of SF_6.) For the crossed beams experiments the power was then reduced to give ~5-10% total ion depletion in the on axis signal. It is also possible to further tune the laser pulse profile with a plasma shutter.[60] The model calculations of sharper pulse profiles showed no dramatic improvement in the final percentage of excited SF_6 in the beam, compared to the initial Lumonics laser pulse.

2.3 Results and Discussion:

In these scattering experiments, we concentrated on attempting to observe changes in the time-of-flight (TOF) of the scattered molecular beam at three different areas of the Newton circle including: the lab angle corresponding to the center-of-mass of the system, a lab angle close to the initial molecular beam, and a lab angle just beyond the Newton circle for elastic scattering. Only "superelastic" collisions, where there is an increase in translational energy, will generate signal at angles greater than the elastic scattering circle. Therefore, only signal in the laser excited TOF spectrum is expected at these angles. At the center-of-mass angle, which corresponds to collisions with large impact parameters, R$\leftrightarrow$T energy exchange will also contribute to changes in the translational energy. Small impact parameter collisions, where one might expect to see the greatest V$\leftrightarrow$T inelasticity, were detected at angles close to the initial molecular beam. Unfortunately, the differential wall used for these experiments, prevented the detector from reaching angles where only "superelastic" collisions would be detected on this side

of elastic circle. See figure 2.1 for details. The specific details of the C_6F_6 and SF_6 experiments are discussed in the following sections.

2.3.1 Hexafluorobenzene:

For the hexafluorobenzene experiments, the velocity selector transmitted $2x10^4$ cm/s, the peak in the distribution of the effusive C_6F_6 beam. The rotational temperature of the C_6F_6 beam was ~300K. Assuming the energy from the UV photon is distributed among all the vibrational degrees of freedom, a vibrational temperature can be assigned to the excited C_6F_6. At thermal equilibrium, the vibrational energy is:

$$U_{vib}(T) = \sum_{i=1}^{30} \frac{\nu_i \exp\frac{-h\nu_i}{kT}}{\left(1-\exp\frac{-h\nu_i}{kT}\right)} \qquad (12)$$

where ν_i is the i^{th} vibrational frequency taken from the literature.[61] The vibrational energy is equal to the sum of $U_{vib}(298K)$, the initial vibrational energy of the effusive beam, and the photon energy. For 248 nm and 193 nm excitation, the calculated vibrational temperature for C_6F_6 was 2500 and 3050 K, respectively.

The secondary beam source was cooled to 100K with liquid nitrogen. The peak velocity of the cold argon beam was $3.2x10^4$ cm/s. Under these conditions, the resulting collision energy was 0.57 kcal/mole which corresponds to ~250K. The ordering of the energy in each degree of freedom was V>>R~T. A similar ordering of energy in each degree of freedom was obtained in the IRMPE sulfur hexafluoride experiments.

Yoshihara et. al. found $\langle\Delta E\rangle$=2.35 kJ/mole ≡ 0.56 kcal/mole with $\frac{\langle\Delta E\rangle}{E}$ =$3.7x10^{-3}$ for the collisional deactivation of 193nm excited C_6F_6 by argon using the Lennard-Jones collision frequency.[20] It is important to emphasize that this is an overall energy transfer rate. Every collision may transfer 0.56 kcal/mole or one out of

ten collisions may transfer ten times this amount of energy. Simulated time-of-flight spectra, shown in figures 2.5 and 2.6, were calculated to demonstrate how the signal in the crossed beams experiment will change assuming every collision transfers 0.5 kcal/mole of energy directly to translation.

For the purpose of the simulation, the change in translational energy was assumed to be 175 $cm^{-1} \equiv 0.5$ kcal/mole, which is corresponds to the lowest vibrational frequency of hexafluorobenzene.[61] By the propensity rules for V→T transfer in systems with low excitations, this is the most likely mode to be deactivated.[1, 2] At high excitation levels, the anharmonicity of the vibrations and the coupling between the normal modes is likely to reduce the energy transferred. Therefore, ΔE_{trans} is likely to be less than 0.5 kcal/mole. Yoshihara et. al. were only able to measure the overall rates of energy transfer,[20], therefore it is difficult to discern which vibrational modes lose the energy and the actual magnitude of ΔE_{trans} for a single collision. Calculated time-of-flight spectra were generated by GMTHRASH, a fortran program which convolutes the assumed product translational energy and angular distributions, $P(E_t)$ and $T(\Theta)$ respectively, over the experimental beam distributions, the collision angles, as well as the detector acceptance angle and ionizer length.[62] In the calculations, the C_6F_6 velocity was 2.0×10^4 cm/s with a speed ratio of 7.0. The argon beam velocity was 3.2×10^4 cm/s with a speed ratio of 7.0. The angular divergence of each beam was 1.0° full width half maximum.

For the "elastic" scattering case, with no laser excitation, the distribution of collision energies was used for the $P(E_t)$. The width of this $P(E_t)$ will induce some additional broadening in the time-of-flight spectrum since in truly elastic collisions the $P(E_t)$ for each collision is simply a delta function at the collision energy. Extra broadening is also expected, due to the R↔T inelastic scattering of the vibrationally cold molecules. For the laser excited spectrum, the "elastic" $P(E_t)$ was offset by 0.5

kcal/mole and peaked at 1.0 kcal/mole. Figure 2.5 shows there is a significant difference in the calculated time-of-flight at 10° in the laboratory frame for the two different $P(E_t)$'s. This time-of-flight spectrum represents the changes expected for lab angles between 10° and 30° assuming every collision transfers 0.5 kcal/mole directly to translation. At the wide angles, -10° and 45° in the laboratory frame, signal would be expected only in the laser excited case.

It was also necessary to consider the percentage of the beam initially excited, particularly for the time-of-flight spectra between 10° and 30° where both the elastic and the superelastic collisions contribute to the signal. For the 193 nm and 248 nm excitation of C_6F_6, it was possible to excite ~10% of the beam before the multiphoton processes dominated the pumping scheme. Figure 2.6 compares the calculated spectra for the laser on and laser off experiments. In the laser on spectrum, 10% of the collisions scatter with a $P(E_t)$ peaked at 1.0 kcal/mole while the remaining 90% scatter with a $P(E_t)$ peaked at 0.5 kcal/mole. These simulations demonstrate that there will be a small, but distinct change in the time-of-flight spectra if every excited molecule transfers 0.5 kcal/mole directly to translation.

An example of the time-of-flight obtained at 10° for C_6F_6 scattering with argon is shown in figure 2.7. The calculated time-of-flight spectrum was broader than the experimental spectrum, in figure 2.7. This discrepancy is due to the width of the "elastic" $P(E_t)$ and the speed ratios used in the model. The speed ratio for the velocity selected C_6F_6 beam was typically 15. The calculation represents a "worst" case scenario where the initial beam resolution is lower than the actual experimental value. Even with the additional broadening, the simulated spectra show it is possible to resolve laser correlated changes in the time-of-flight for ΔE_t=0.5 kcal/mole.

TOF spectra were also measured at 18° and 45°. No laser correlated signal was detected, proving the $\langle \Delta E \rangle$ measured by Yoshihara et. al.[20] is likely to be distributed

between the rotational as well as translational degrees of freedom, with ΔE_{trans} peaked at zero. Although the bulb type experiments indicate $<\Delta E>$ is not strongly dependent on the rare gas, experiments were also performed with neon and krypton collider gases. As in the argon case, no differences in the TOF spectra were observed. This confirms the argon results, that ΔE_{trans} is peaked at zero.

As demonstrated by the calculations, very small changes in the time-of-flight spectra are expected with only 10% of the initial C_6F_6 beam excited. Unfortunately, very long counting times were required to obtain reasonable signal to noise in the laser excited spectrum. This was particularly a problem with the velocity selected effusive C_6F_6 beam. In this case the number density of the C_6F_6 beam was low due to the required low backing pressure, the velocity selection, and the long distance between the source and the collision zone. It was possible to obtain better signal to noise for the laser off spectra over the counting time. With the 4096 channel scaler running at 2.5μsec per channel, the laser at 90 Hz, and the molecular beam pulses at ~400 Hz, several time-of-flight spectra were collected with the laser off for each laser on spectrum. As mentioned in the experimental section, the chopped portion of the beam was ~35 μsec long. With the laser running at 90 Hz, three hours of counting time in this pulsed experiment is equivalent to only ~30 sec counting time in a continuous experiment. These factors made detecting small changes in the time-of-flight challenging. To improve the signal to noise by a factor of five would require 75 hours of counting. Long signal averaging was not feasible with the instability and the poor reliability of the laser.

It is important to mention that the addition of the cryopanels were an ongoing project throughout these experiments. The cryopanels cooled by the Koch helium compressor were not installed for the C_6F_6 experiments. For these experiments, a small cryopanel attached to an Air Products helium compressor was used to reduce the background.

2.3.2 Sulfur Hexafluoride:

The initial experiments with sulfur hexafluoride were performed under similar conditions to thoses just described for the hexafluorobenzene experiments. A velocity selected room temperature SF_6 beam was collided with a cryogenically cooled argon beam. In the SF_6 case, IRMPE was used to obtain a vibrationally excited distribution, as shown in figure 2.4. The model calculations and on axis SF_6 mass spectrum indicate that ~50% of the beam was excited. With this high fraction of the beam excited, changes in the translational energy resulting from V→T energy transfer should be more obvious than for the C_6F_6 case where only 10% of the beam was excited. The lowest frequency vibration for SF_6 is $\nu_6 = 347\ cm^{-1}$. If this mode is the "doorway" for V-T relaxation,[14] the time-of-flight spectra should also reflect larger laser correlated changes than for the C_6F_6 case. This mode also has a small anharmonic constant, $\chi_6 = -0.1\ cm^{-1}$. At high excitation levels, the ΔE for a $\Delta v = -1$ change will not be significantly reduced by the anharmonicity. As mentioned in the hexafluorobenzene case, the intermode coupling at the high excitation levels is likely to reduce ΔE_{vib}.

Beck et. al., using time-resolved optoacoustics to monitor SF_6 relaxing in argon, found $\frac{\langle \Delta E \rangle}{\langle E \rangle} = 4.1 \times 10^{-4}$ for SF_6 excited between 4,000-19,000cm^{-1}. [25] Again, it is important to emphasize that this is an overall energy transfer rate; the magnitude of the $\langle \Delta E_{up} \rangle$ and $\langle \Delta E_{down} \rangle$ collisions might be significantly larger. In our molecular beams experiment, the SF_6 absorbs an average of 25-30 934 cm^{-1} photons with the laser power at 3 J/cm^2. This corresponds to an average excitation of ~25,000 cm^{-1} and a $\langle \Delta E \rangle = 10$ cm^{-1} per Lennard-Jones collision, if Beck's value is used.

It would only be possible to detect changes in the time-of-flight if $<\Delta E_{down}>$ is larger than $<\Delta E>$and if the measured rate represents a case where only a few collisions transfer a much larger amount of energy. As in the C_6F_6 case, time-of-flight spectra were measured at three different lab angles corresponding to small impact parameter collisions, large impact parameter collisions, and areas beyond the elastic circle. No laser correlated changes were detected within the signal to noise. Again, this demonstrates that the ΔE_{trans} is peaked at zero.

To investigate the possibility of enhanced T↔R exchange with the vibrationally hot molecules, the effusive SF_6 beam was replaced by a supersonic beam and the argon beam was kept at room temperature. Under these conditions, the rotations of the SF_6 were cooled in the expansion so that V>>T>R. This should increase the likelihood of T→R energy transfer. In this case, if energy is transferred from translation to the rotations, a shift to longer flight times in the TOF spectra is expected. Figure 2.8 shows the Newton circles for elastic scattering, V→T transfer, and T→R transfer. The time-of-flight spectrum at 22°, the center of mass angle where the greatest T↔R exchange was expected, is shown in figure 2.9. Again, no laser correlated changes in the time-of-flight were detected indicating T→R energy transfer is not affected by the additional vibrational energy in the laser excited case.

Unfortunately, it was difficult to quantify how effectively the initial molecular beam was excited in both the C_6F_6 and the SF_6 experiments. If laser correlated changes in the time-of-flights dependent on both the laser power and on the secondary beam had been detected, the initial vibrational excitation of the molecular beam would also have been confirmed. Since there were no detectable differences, the lack of signal can be attributed either to very small amounts of translational energy exchange or to inefficient preparation of the excited molecular beam.

A thorough characterization of the excited molecular beam facilitates the determination of whether the lack of laser correlated signal was due to a problem in the preparation of the vibrationally excited beam. In both the UV and IRMPE excitation the lasers were set at a range of powers including where the largest percentage of excited molecules was expected, as well as a variety of other powers. The on-axis mass spectrum of the C_6F_6 and SF_6 beams showed a shift to the smaller ion fragments as a function of laser power and laser time delay. It was also possible to deplete >70% of the total on axis fragment ion counts by multiphoton dissociation at high laser powers. This indicated that there was a reasonable overlap between the laser beam and the molecular beam pulse. The cracking patterns are expected to change as a function of vibrational energy,[63] therefore, the on axis diagnostics suggested that a significant amount of the molecular beam was vibrationally excited. The off axis TOF spectra were measured at both the major ion fragments of C_6F_6 ($C_6F_6^+$ and $C_5F_3^+$) and SF_6 (SF_5^+) as well as the smaller ion fragments since the vibrationally hot molecules are likely to fragment to smaller ions in the ionizer, especially if only a small amount of energy is transferred in the collision. Both the on axis beam diagnostics and the excitation models indicated that a significant fraction of the beam was vibrationally excited. Unfortunately, however, it was not possible to directly measure the total vibrational energy that was deposited into the beam and therefore the model predictions for the UV and IR excitations schemes could not be confirmed.

2.4 Conclusion:

This series of crossed molecular beam experiments was designed to directly measure the probability distribution function for V→T energy transfer under single collision conditions. Two techniques, UV excitation followed by internal conversion and

IRMPE, were used to generate molecular beams of highly vibrationally excited C_6F_6 and SF_6. The V→T and T→R energy transfer processes for collisions between the excited molecules and rare gas atoms were monitored by time-of-flight techniques. Both of these studies indicate that very little energy is exchanged to or from the translational degree of freedom in one collision. The ΔE_{trans} is likely to be peaked at zero.

These crossed molecular beam studies combined with the propensity rules and the models for V→T energy transfer indicate that the relaxation of a highly vibrationally excited molecule by a rare gas atom is likely to occur through a rotationally mediated process. The first collision must induce a V→R energy exchange and R→T deexcitation occurs during subsequent collisions. In this case, no laser correlated changes in the time-of-flight spectra are expected or observed for the single collision experiment where only the product velocity is monitored.

2.5 References:

1. J. T. Yardley, *Introduction to Molecular Energy Transfer* (Academic Press, New York, 1980).

2. J. D. Lambert, *Vibrational and Rotational Relaxation in Gases* (Clarendon Press, Oxford, 1977).

3. H. Hippler and J. Troe, in *Advances in Gas-Phase Photochemistry and Kinetics* M. N. R. Ashfold and J. E. Baggott, Eds. (The Royal Society of Chemistry, 1989), pp. 209.

4. I. Oref and D. C. Tardy, Chem. Rev. **90**, 1407 (1990).

5. D. C. Tardy and B. S. Rabinovitch, Chem. Rev. **77**, 369 (1977).

6. K. Luther and K. Reihs, Ber. Bunges. Phys. Chem. **92**, 442 (1988).

7. K. Patten, Ph.D., University of California - Berkeley, 1991.

8. J. Troe, J. Chem. Phys. **77**, 3485 (1982).

9. P. J. Robinson and K. A. Holbrook, *Unimolecular Reactions* (Wiley, New York, 1972).

10. J. Troe, J. Phys. Chem. **83**, 114 (1979).

11. J. Hirschfelder, C. F. Curtiss and R. B. Bird, *Molecular Theory of Gases and Liquids* (John Wiley and Sons Inc., New York, 1954).

12. M. Quack and J. Troe, in *Gas Kinetics and Energy Transfer* P. G. Ashmore and R. J. Donovan, Eds. (The Chemical Society, London, 1977).

13. H. G. Lohmannsroben and K. Luther, Chem. Phys. Lett. **144**, 473 (1988).

14. R. J. Gordon, Comments At. Mol. Phys. **21**, 123 (1988).

15. H. Hippler, J. Troe and H. J. Wendelken, J. Chem. Phys. **78**, 5351 (1983).

16. M. Heymann, H. Hippler and J. Troe, J. Chem. Phys. **80**, 1853 (1984).

17. J. E. Dove, H. Hippler and J. Troe, J. Chem. Phys. **82**, 1907 (1985).

18. M. Damm, H. Hippler and J. Troe, J. Chem. Phys. **88**, 3564 (1988).

19. N. Nakashima and K. Yoshihara, J. Chem. Phys. **79**, 2727 (1983).

20. T. Ichimura and Y. Mori, J. Chem. Phys. **83**, 117 (1985).

21. T. Ichimura, M. Takahashi and Y. Muri, Chem. Phys. **114**, 116 (1987).

22. J. Shi, D. Bernfeld and J. R. Barker, J. Chem. Phys. **88**, 6219 (1988).

23. J. Shi, D. Bernfeld and J. R. Barker, J.Chem. Phys. **88**, 6211 (1988).

24. M. J. Rossi, J. R. Pladziewicz and J. R. Barker, J. Chem. Phys. **78**, 6695 (1983).

25. K. M. Beck and R. J. Gordon, J. Chem. Phys. **87**, 5681 (1987).

26. L. Zhang, J. Chou and G. Flynn, (to be published).

27. R. N. Schwartz, Z. I. Slawsky and K. F. Herzfeld, J. Chem. Phys **20**, 1591 (1952).

28. T. L. Cottrell, R. C. Dobbie, J. McLain and A. W. Read, Trans. Faraday Soc. **60**, 241 (1964).

29. K. F. Lim and R. G. Gilbert, J. Chem. Phys. **84**, 6129 (1986).

30. H. Hippler, H. W. Schranz and J. Troe, J. Phys. Chem. **90**, 6158 (1986).

31. W. L. Hase, N. Date, L. B. Bhuiyan and D. Buckowski, J. Phys. Chem. **89**, 2502 (1985).

32. N. J. Brown and J. A. Miller, J. Chem. Phys. **80**, 5568 (1984).

33. C. B. Moore, J. Chem. Phys. **43**, 2979 (1965).

34. H. W. Schranz and J. Troe, J. Phys. Chem. **90**, 6168 (1986).

35. M. Heymann, H. Hippler, D. Nahr, H. J. Plach and J. Troe, J. Phys. Chem. **92**, 5507 (1988).

36. M. Heymann, H. Hippler, H. J. Plach and J. Troe, J. Chem. Phys. **87**, 3867 (1987).

37. W. R. Gentry, J. Chem. Phys. **81**, 5737 (1984).

38. S. K. Gray and S. A. Rice, J. Chem. Phys. **83**, 2818 (1985).

39. U. Buck, in *Atomic and Molecular Beam Methods* G. Scoles, Eds. (Oxford University Press, New York, 1988), pp. 525.

40. D. J. Krajnovich, C. S. Parmenter and D. J. Catlett, Chem. Rev. **87**, 237 (1987).

41. J. Eccles, G. Pfeffer, E. Piper, G. Ringer and J. P. Toennies, Chem. Phys. **89**, 1 (1984).

42. R. J. Brudzynski, Ph.D., University of California, Berkeley, 1987.

43. R. J. Brudzynski, personal communication.

44. Y. T. Lee, J. D. McDonald, P. R. LeBreton and D. R. Herschbach, Rev. Sci. Inst. **40**, 1402 (1969).

45. G. O. Brink, Rev. Sci. Instrum. **37**, 857 (1966).

46. N. R. Daly, Rev. Sci. Instrum. **31**, 264 (1960).

47. R. E. Continetti, Ph.D., University of California Berkeley, 1989.

48. D. Proch and T. Trickl, Rev. Sci. Inst. **60**, 713 (1989).

49. A. M. Schmoltner, P. M. Chu, R. J. Brudzynski and Y. T. Lee, J. Chem. Phys. **91**, 6926 (1989).

50. Liquid helium dewar and transfer lines were designed by C. Chiladakis.

51. J. Philis, A. Bolovinos, G. Andritsopoulos, E. Pantos and P. Tsekeris, J. Phys. B: At. Mol. Phys. **14**, (1981).

52. D. Phillips, J. Chem. Phys. **46**, 4679 (1967).

53. D. V. O'Connor, M. Sumitani, J. M. Morris and K. Yoshihara, Chem. Phys. Lett. **93**, 350 (1982).

54. I. Haller, J. Chem. Phys. **47**, 1117 (1967).

55. N. Nakashima and K. Yoshihara, J. Chem. Phys. **79**, 2727 (1983).

56. H. Hippler, Ber. Bunsenges. Phys. Chem. **89**, 303 (1985).

57. G. Herzberg, *Molecular Spectra and Molecular Structure* (Van Nostrand, Princeton, NJ, 1950).

58. P. Sulzer and K. Weiland, Helv. Phys. Acta **25**, 653 (1952).

59. P. A. Schulz, A. S. Sudbo, D. J. Krajnovich, H. S. Kwok, Y. R. Shen and Y. T. Lee, Ann. Rev. Phys. Chem. **30**, 379 (1979).

60. P. A. Schulz, Ph.D., University of California Berkeley, 1979.

61. D. Steele and D. H. Whiffen, Trans. Faraday Soc. **55**, 369 (1959).

62. R. Buss, Ph.D. Thesis, University of California, Berkeley, 1979.

63. H. G. Rubahn, J. P. Toennies, M. Wilde and J.Wanner, Chem. Phys. Lett. **120**, 11 (1985) and references therein.

2.6 Figures:

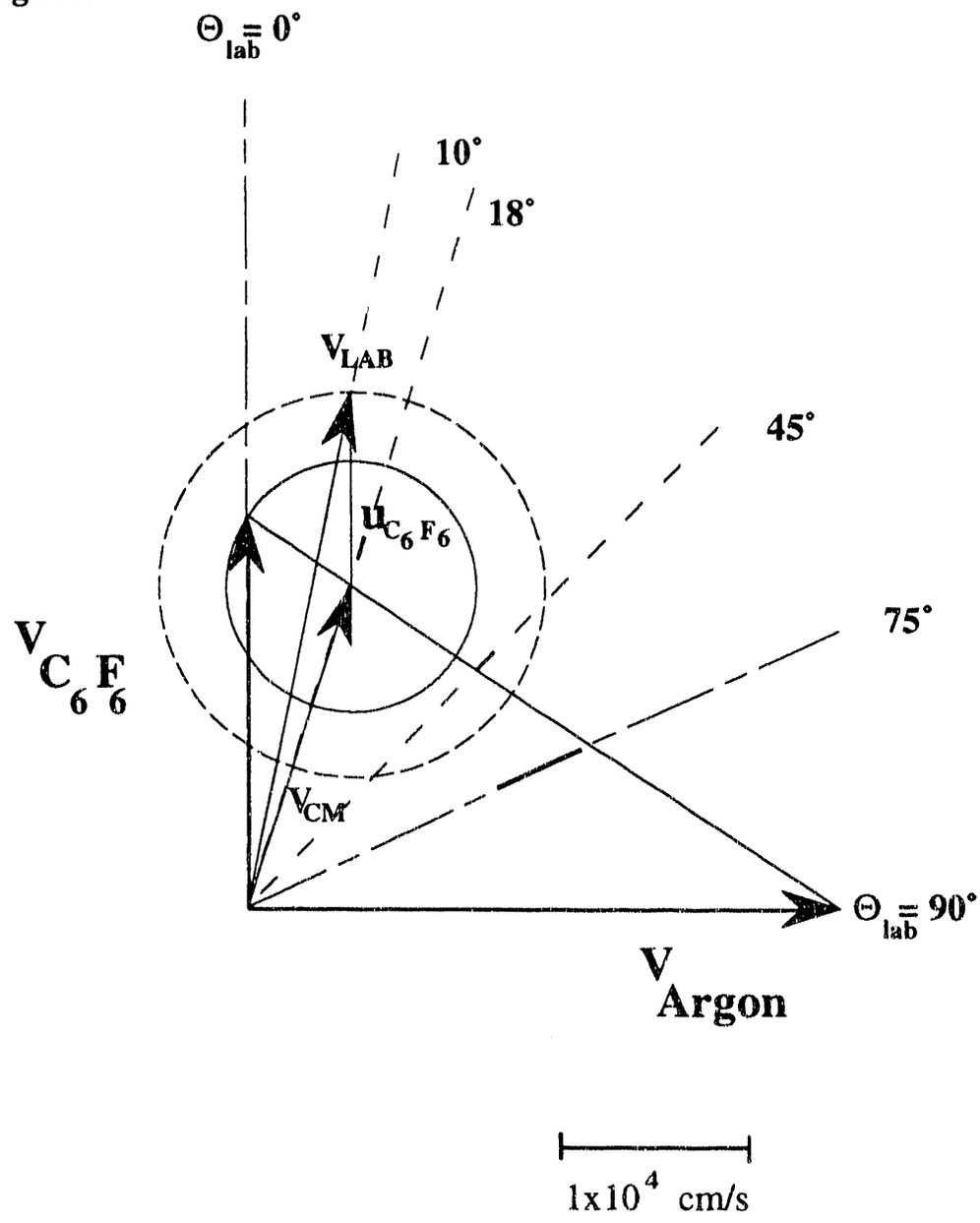

Figure 2.1: Newton diagram of hexafluorobenzene and argon at 0.5 kcal/mole collision energy. Solid circle represents elastic scattering of C_6F_6. Dashed circle represents inelastic scattering of C_6F_6 with 0.5 kcal/mole V→T energy transfer. Dashed lines represent lab angles measured. Centered dashed lines show detector viewing range. $\mathbf{u_{c6f6}}$= center of mass frame velocity of inelastically scattered hexafluorobenzene. $\mathbf{V_{cm}}$ = center of mass velocity. $\mathbf{V_{lab}}$= velocity of inelastically scattered hexafluorobenzene in the lab frame.

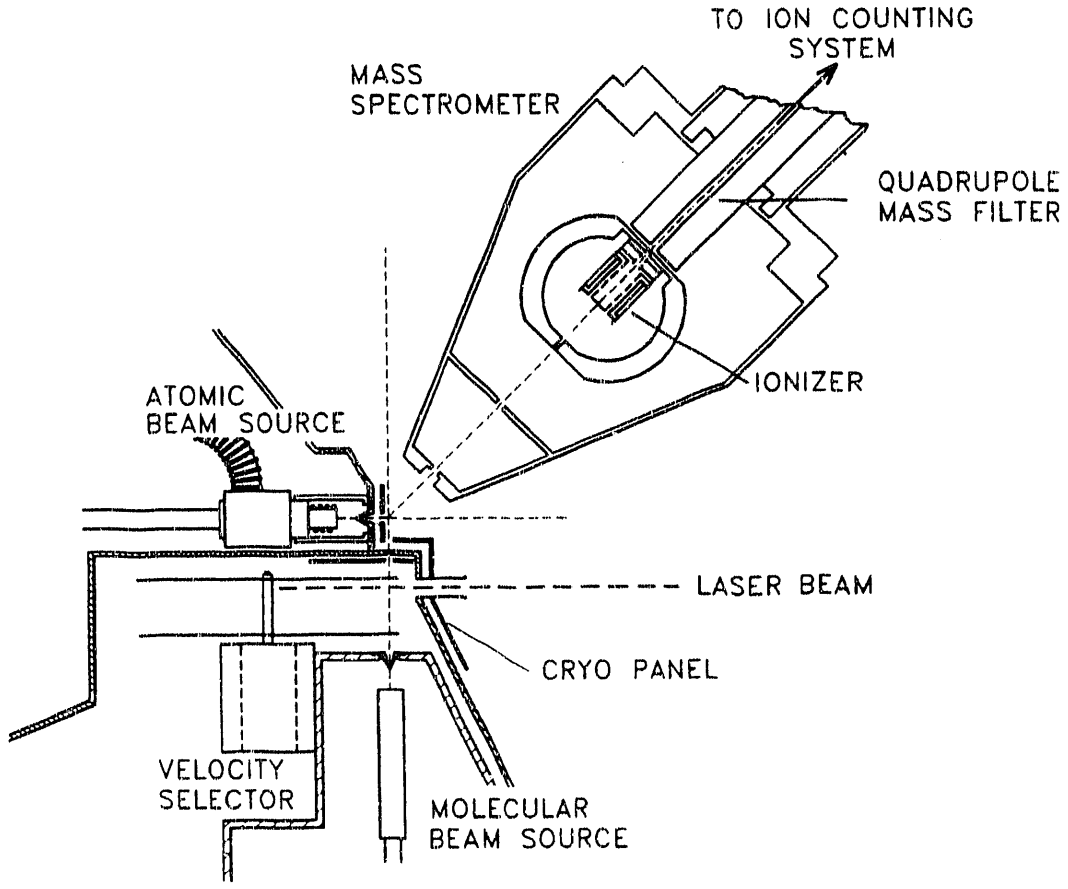

Figure 2.2: Schematic view of crossed molecular beams apparatus with differentially pumped beams and rotatable mass spectrometer detector. Primary beam is velocity selected by two chopper wheels in the differential chamber. Secondary beam temperature was adjusted with a heating element and liquid nitrogen cooling. Dashed lines indicate the reactant beams, the laser beam, and products entering the detector.

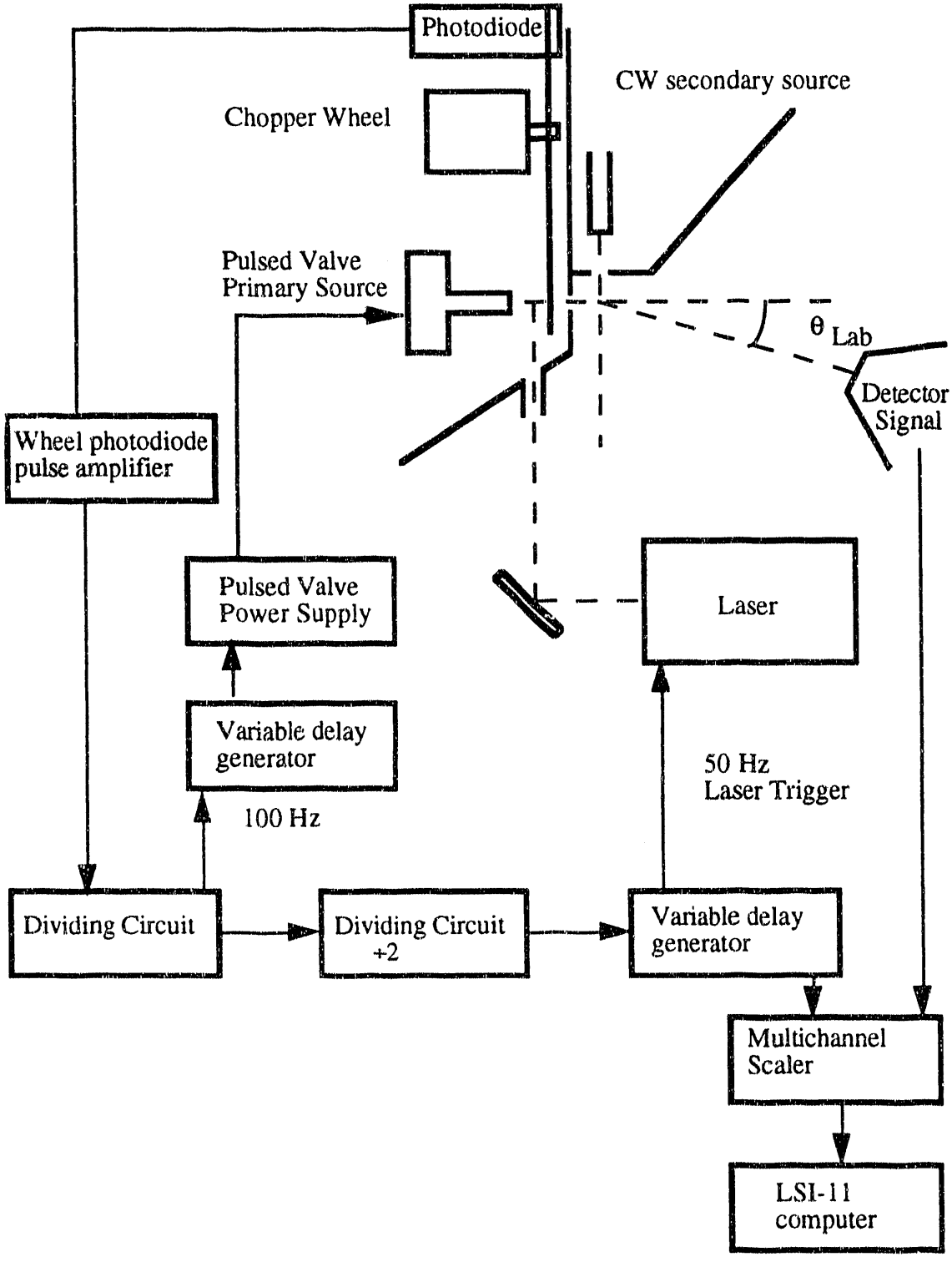

Figure 2.3: An example of the timing electronics with pulsed valve as primary beam source. A photodiode monitors the chopper wheel and initiates the timing for the experiment.

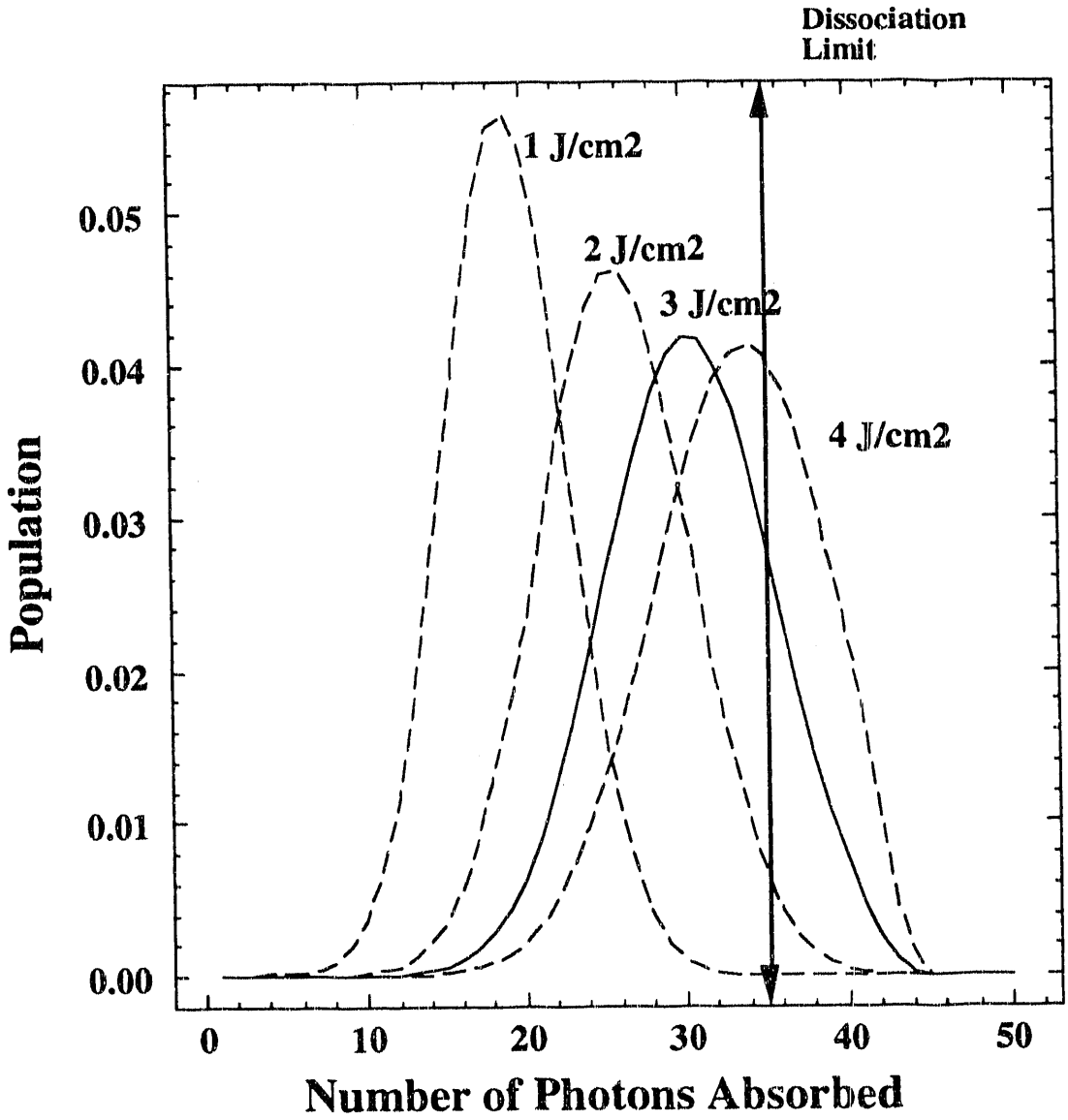

Figure 2.4: The modeled population distributions SF_6 excited by IRMPE.The quasicontinuum distributions are shown as a function of laser fluence for the Lumonics laser pulse profile. The portion of the distributions which absorb >35 photons will dissociate before reaching the collision zone. The solid line represents the distribution used for the majority of the experiments.

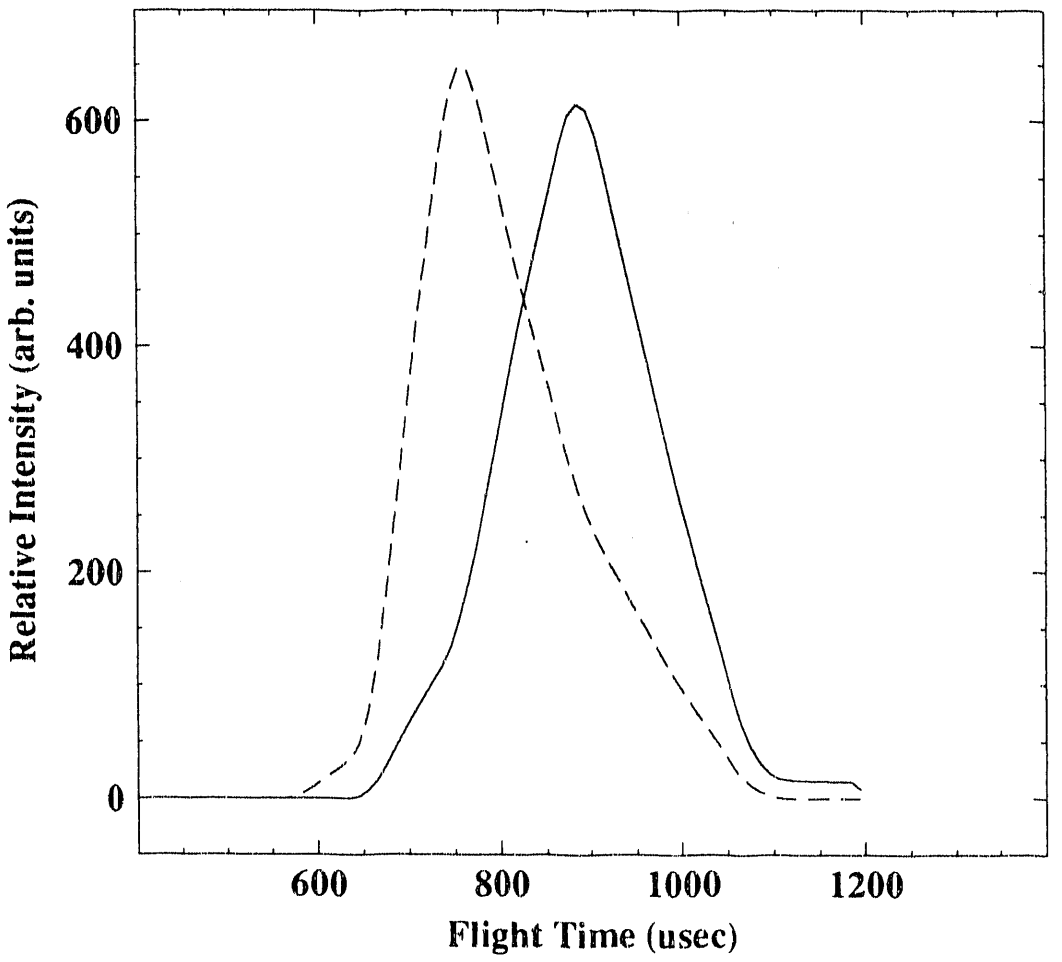

Figure 2.5: Simulated time-of-flight spectra for C_6F_6 and argon at 10°. Solid line represents "elastically" scattered C_6F_6. Dashed line represents inelastically scattered C_6F_6 with 0.5 kcal/mole transferred directly from vibrations to translation.

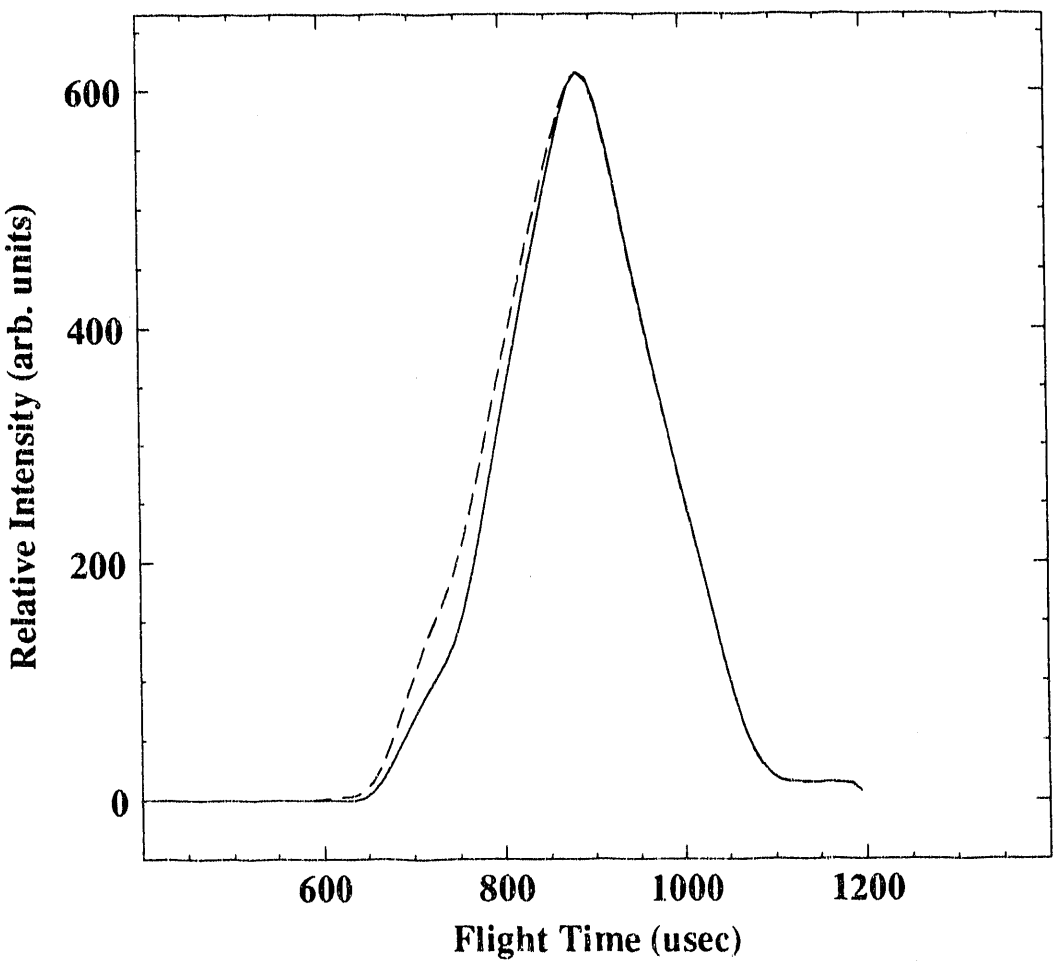

Figure 2.6: Simulated time-of-flight spectra for C_6F_6 and argon. Solid line represents "elastically" scattered C_6F_6. Dashed line represents inelastically scattered C_6F_6 with 10% of the collisions recoiling with a $P(E_t)$ peaked at 1.0 kcal/mole and 90% of the collisions recoiling with a $P(E_t)$ peaked at 0.5 kcal/mole.

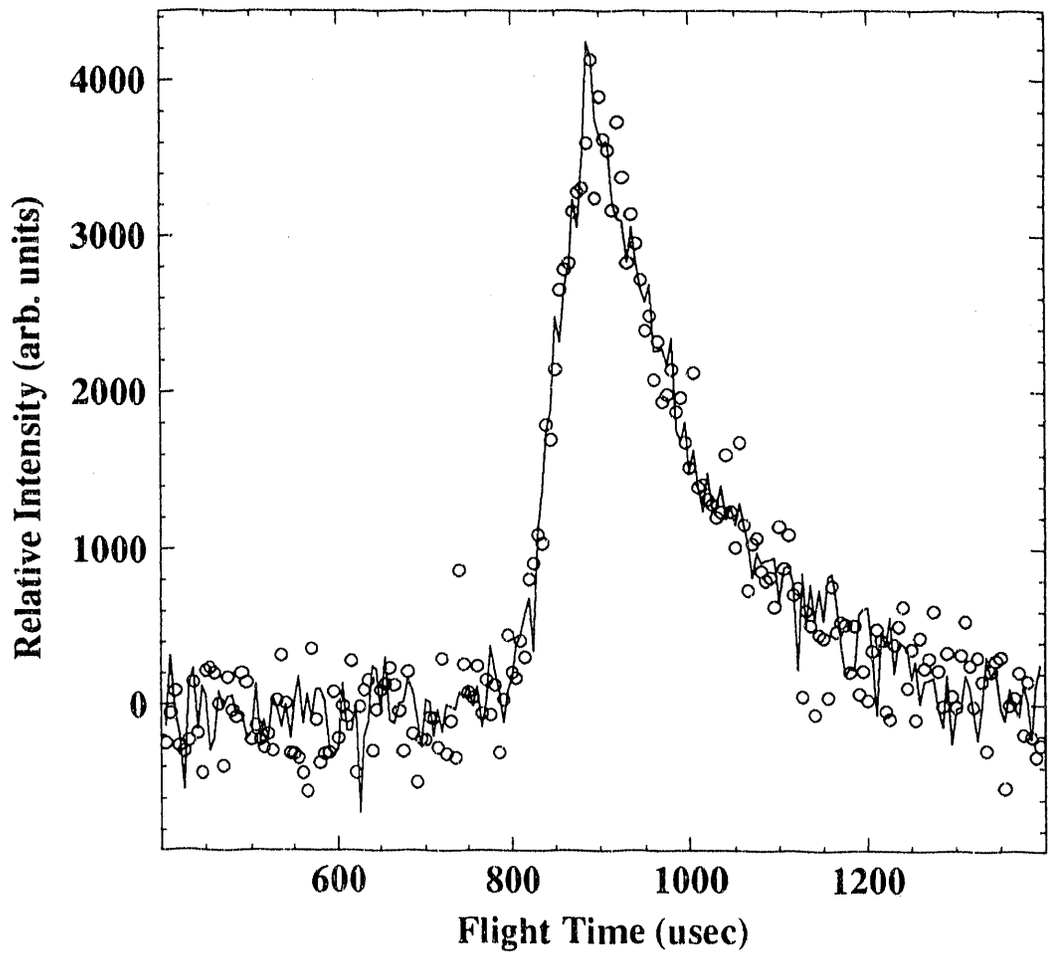

Figure 2.7: TOF spectrum of $C_5F_3^+$ (at Lab angle=10°) for C_6F_6 scattering with argon at 0.5 kcal/mole collision energy. The laser power was maintained at 20 mJ/cm^2. The solid line represents the laser off spectrum. The open circles show the laser on spectrum. Total counting time was three hours.

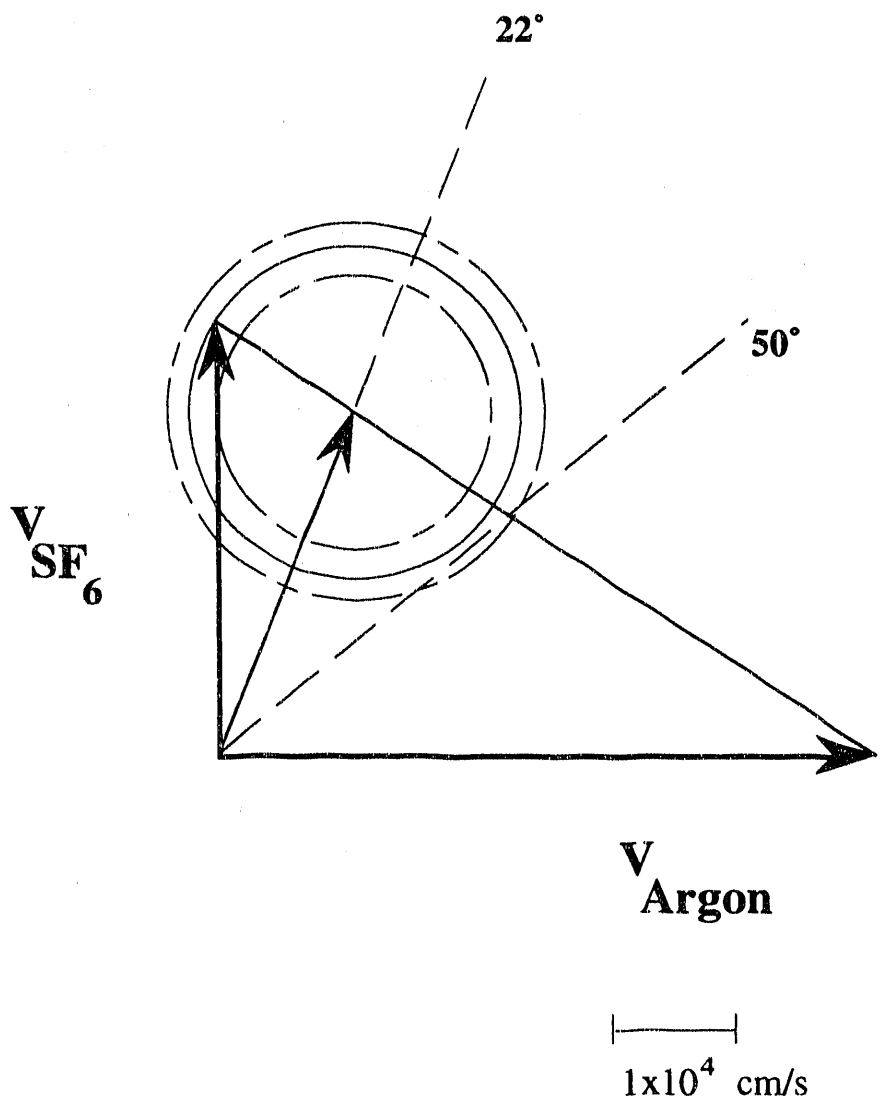

Figure 2.8: Newton diagram of sulfur hexafluoride and argon (supersonic beams) at 1.7 kcal/mole collision energy. Solid circle represents elastic scattering of SF_6. Large dashed circle represents inelastic scattering of SF_6 with 0.5 kcal/mole going into translation. Small dashed circle represents a 0.5 kcal/mole energy transfer from translation to rotation.

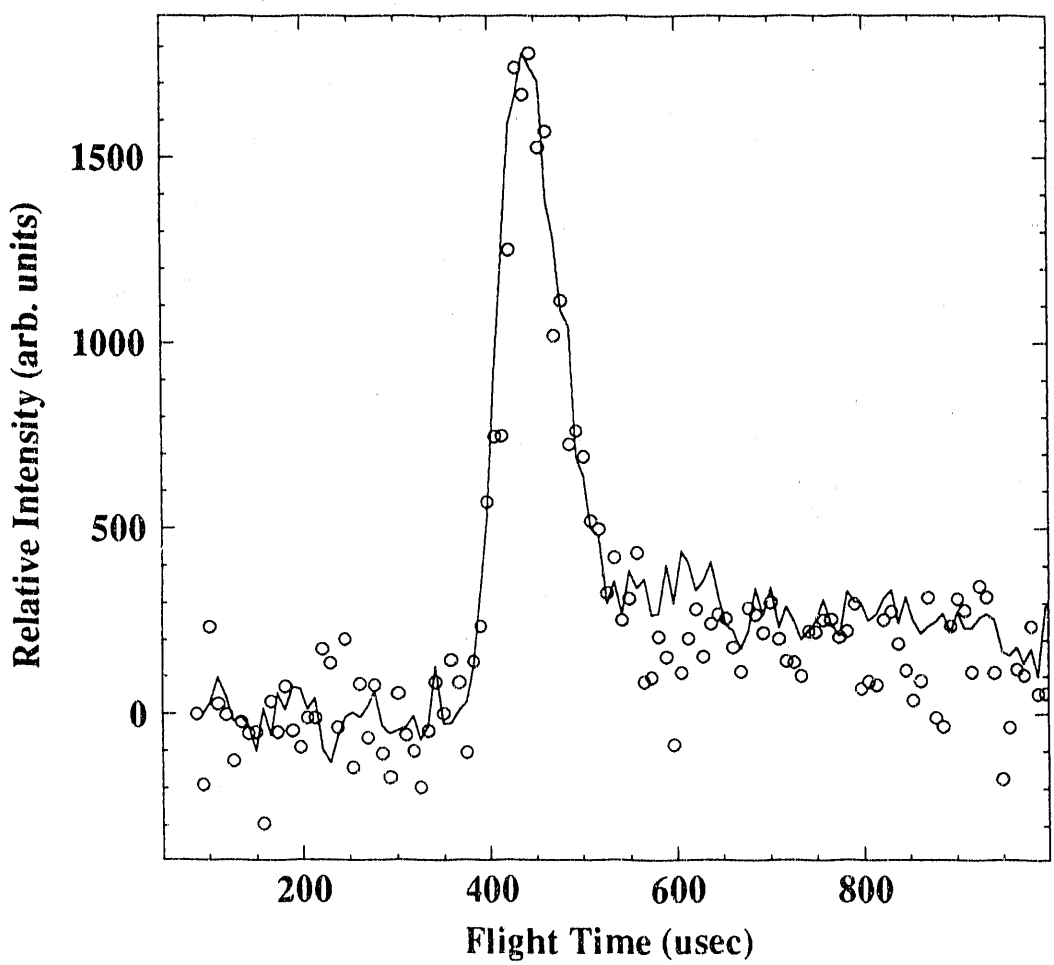

Figure 2.9: TOF spectrum at 22°, the center of mass angle, for SF_6 scatteringwith argon at a collision energy of 1.7 kcal/mole . The signal was monitored at SF_3^+. The CO_2 laser power was maintained at 3 J/cm^2. The solid line represents the laser off spectrum. The open circles show the laser on spectrum. Total counting time was three hours.

Chapter 3:

Photodissociation of Nitrobenzene at 266 nm:

3.1 Introduction:

Although the thermal decomposition of aromatic nitrocompounds has been an active area of research, the primary dissociation processes are still poorly understood. It has been well established that C-N bond scission to form phenyl radicals and NO_2 is the dominant process.[1, 2] There are, however, additional possible channels including isomerization and molecular elimination. Analogous unimolecular decomposition pathways have been observed for the infrared multiphoton dissociation of several nitroalkanes under molecular beam conditions.[3] In the present study, photofragmentation translational spectroscopy was used to examine the unimolecular decomposition of nitrobenzene following 266nm excitation. Primary dissociation products from excited electronic states as well as from the highly vibrationally excited ground electronic state were detected using time-of-flight and mass spectrometry.

There has been some controversy regarding the primary dissociation mechanism(s) for the thermal decomposition of nitroaromatic compounds.[4] Recent

investigations, however, have concluded that surface catalyzed reactions can influence the primary product identification. To minimize surface interactions, Gonzalez et. al. examined the thermal decomposition of nitrobenzene using laser-powered homogeneous pyrolysis.[1] Under these conditions nitrobenzene was found to decompose via two different mechanisms. The principal initial step is C-NO_2 bond scission to give phenyl radical and NO_2. The C-NO_2 bond dissociation energy was found to be 71.4 kcal/mole. A second channel which includes a nitro→nitrite rearrangement followed by O-NO bond scission to give phenoxy radical and NO was also identified. The branching ratio for these two channels was found to be 4:1 in favor of the simple bond rupture reaction. Shock tube studies by Tsang et. al. have confirmed that these two channels are important primary processes with the bond cleavage reaction favored over the NO_2 isomerization by at least 2:1.[2]

Infrared multiphoton dissociation (IRMPD) studies of nitroalkanes have also identified several possible reaction channels for nitro compounds.[3] As a result of the rapid intramolecular vibrational energy redistribution following the absorption of many IR photons, infrared radiation can be used to prepare molecules in highly vibrationally excited ground electronic state similar to a thermal excitation scheme. IRMPD coupled with molecular beam techniques has been extensively used to elucidate the primary unimolecular decomposition products under collision free conditions.[3, 5, 6, 7, 8, 9, 10] In the IRMPD studies by Wodtke et. al.,[3] three possible unimolecular decomposition channels were found for vibrationally excited nitroalkanes. The channels include simple bond rupture, nitro-nitrite isomerization followed by O-NO bond dissociation, as well as molecular elimination of HONO. The branching ratios for these competitive channels is dependent on the activation barriers, A factors and the IR absorption cross section.

Since electronically excited molecules can relax via both radiative and nonradiative pathways, UV excitation is an alternative method of preparing highly vibrationally excited molecules in the ground electronic state. Many of the nitroaromatic compounds do not exhibit fluorescence or phosphorescence after electronic excitation[11], suggesting the excited singlet states relax predominantly through non-radiative channels. Possible pathways include dissociation of the initially prepared state as well as internal conversion and/or intersystem crossing followed by dissociation from lower lying electronic surfaces. High internal conversion rates in nitro aromatic compounds have been attributed to strong vibronic coupling between the excited and ground electronic states due to the NO_2 group.[11] The decomposition channels following UV excitation and rapid internal conversion should be similar to the channels found for thermal dissociation processes. In the studies presented here, the primary products for unimolecular decomposition of nitrobenzene following 266 nm excitation were identified. The energetically available product channels are shown in table 3.1.

The gas phase UV absorption spectrum of nitrobenzene has been the subject of numerous experimental and theoretical investigations.[11, 12, 13, 14] Theoretical calculations have been used to predict the ordering of the energy levels and the charge distributions of the lower excited electronic states. The first two excited singlet states are assigned to the strong absorptions between 240-280 nm. The band at 283 nm corresponds to a $\pi \rightarrow \pi^*$ transition in the phenyl ring, similar to the $A_{1g} \rightarrow B_{2u}$ transition in benzene, as well as a charge transfer from the benzene ring.[12] The band at 240 nm has been assigned exclusively to a $\pi \rightarrow \pi^*$ electron charge transfer from the benzene ring to the nitro group.[12] With the 266nm photon, both the 283nm and 240nm bands are likely to be excited. Additionally, calculations indicate there are seven triplet states between 270-500 nm.[13]

In addition to identifying the primary decomposition products of nitrobenzene, the photodissociation of nitrobenzene at 266 nm also provided an opportunity to study the unimolecular decomposition of phenoxy radicals. Phenoxy radicals are an important intermediate in the combustion of aromatic hydrocarbons. Previous studies have shown that vibrationally excited phenoxy radicals unimolecularly decompose to carbon monoxide and cyclopentadienyl radical.[6, 15, 16] This process has recently been observed in infrared multiphoton dissociation studies of anisole under molecular beam conditions.[6] In the present study, there are two sources of phenoxy radical decomposition spontaneous secondary dissociation and secondary photodissociation.

3.2 Experimental:

The universal crossed molecular beams apparatus used in this study is described in chapter 2. For these photodissociation experiments, a supersonic molecular beam was crossed at 90° in the main vacuum chamber with the output of a Quanta Ray Nd:YAG laser, as shown in figure 3.1. The photodissociation products were detected in the plane of the laser and molecular beams by a rotatable quadrupole mass spectrometer detector coupled with time-of-flight techniques.

The molecular beam was formed by bubbling nitrogen through nitrobenzene maintained at 60° C by a temperature regulated heat bath. The vapor pressure of nitrobenzene is 5 Torr at 60° C.[17] The gas mixture was delivered to the molecular beam apparatus through copper tubing heated to ~75° C to prevent condensation. The gas was expanded through a 0.020 in diameter stainless steel nozzle which was held at 200° C to minimize dimer formation. The total stagnation pressure was 80 Torr. Finally, the molecular beam passed through a 0.020 in diameter skimmer and was

defined by a 0.060" x 0.070" aperature to give a 2° beam divergence. The resulting beam velocity was 9.6×10^4 cm/s with a speed ratio of 5.

As in the experiments described in chapter 2, the molecular beam was modulated by a 7" diameter chopper wheel with two 0.120" slits. The wheel was mounted in the differential pumping region to reduce the main chamber background at the nitrobenzene fragment masses. ~20 μsec beam pulses were generated by spinning the wheel at 300 Hz. With a 9.6×10^4 cm/s nitrobenzene peak beam velocity, the corresponding beam pulse was 1.7 cm long. An optical switch was used to monitor the chopper wheel and to initiate the trigger signals for the laser and ion counting electronics. The overlap between the laser and molecular beam was optimized by adjusting the laser trigger time delay to give the largest photodissociation signal.

266 nm photons were generated by a Quanta-Ray DCR 2A Nd:YAG laser equipped with a harmonic generator. A Pellin-Broca prism separated the 266nm output from the fundamental and second harmonic, 1064 and 532 nm, respectively. The laser was coupled into the main vacuum chamber through a 1" diameter suprasil flat. A UV grade fused silica lens with a 75 cm focal length in the vacuum chamber was used to focus the laser to a 2.5 mm diameter spot at the interaction region. Average pulse energies were ~32 mJ corresponding to a fluence of 620 mJ/cm^2 per pulse. The polarization of the laser light was parallel to the plane of the molecular beam and the detector.

The flight length between the interaction zone and the ionizer was 20.8 cm. The measured time-of-flight distributions (TOF) included the product flight time over this 20.8 cm path as well the ion flight time between the ionizer and the Daly type ion counter. The true neutral product flight time was obtained by subtracting the ion flight time from the measured TOF. The ion flight time for a singly charged ion with mass m is given by the formula, $\alpha\sqrt{m}$, where α is a function of the detector conditions and was

determined by calibration experiments.[8] The TOF's were recorded by a multi-channel scaler (MCS) set at a 2μsec dwell time. The TOF's shown were averaged over 50,000-100,000 laser shots with the Nd:YAG laser operating at 15 Hz. Timing of the MCS was initiated by a reference pulse from the laser. Data acquisition and storage was handled by an LSI-11/73 computer.

Nitrobenzene was obtained from Aldrich and was degassed by several freeze-pump-thaw cycles at liquid nitrogen temperatures. A GC-MS analysis indicated the sample was 99.99% pure.

3.3 Results and Analysis:

To identify the primary dissociation channels time-of-flight spectra were measured at laboratory angles between 10° and 30° for m/e 16, 17, 30, 39, 46, 47, 65, 76, 77, 93, 106 and 107 which correspond to O^+, OH^+, NO^+, $C_3H_3^+$, NO_2^+, $HONO^+$, $C_5H_5^+$, $C_6H_4^+$, $C_6H_5^+$, $C_6H_5O^+$, $C_6H_4NO^+$and $C_6H_5NO^+$. The products were found to extensively fragment in the ionizer of the mass spectrometer detector. By recognizing common features in the TOF spectra, it was possible to identify the parent-daughter ion fragments. Neutral product recoil partners were found based on the conservation of momentum in the center-of-mass frame.

The time-of-flight spectra were fit by assuming a translational energy distribution $P(E_{trans})$ and angular distribution $\omega(\theta)$ in the center-of-mass frame (CM). The CM angular distribution for a single photon process in the dipole approximation is given by $\omega(\theta) = \frac{1}{4\pi}[1 + 2\beta P_2(\cos\theta)]$ where θ is the angle between the electric vector of the laser light and the CM recoil direction of the products. β, the anisotropy parameter, is between $-1 \leq \beta \leq 2$. When $\beta = 2$ the transition dipole is parallel to the reaction coordinate and

when $\beta = -1$ the transition is perpendicular to the reaction coordinate. The experimental time-of-flight spectra were fit assuming a trial $P(E_{trans})$ and β parameter. These values were convoluted over the initial beam velocity distribution, the dimensions of the interaction zone, the ionizer length, and the Jacobian transformation factor to convert from the center of mass distribution to the laboratory distribution using CMLAB2.[18] The $P(E_t)$ and β were adjusted until a "best" fit for the time-of-flight spectrum was obtained. The time-of-flight distributions were not strongly dependent on β, suggesting the products were isotropically distributed in the center-of-mass frame.

The intense signal found at m/e 46 and m/e 77, NO_2^+ and $C_6H_5^+$, indicates the dominant primary process in the photodissociation of nitrobenzene at 266nm is C-N bond cleavage to form phenyl and NO_2 radicals.

$$C_6H_5NO_2 \xrightarrow{266\ nm} C_6H_5 + NO_2 . \qquad (1)$$

The TOF distributions are shown in figures 3.2 and 3.3 and were most easily fit assuming two different $P(E_{trans})$s in figure 3.4. This suggests that reaction (1) is formed via two distinct mechanisms. In one case, the $P(E_{trans})$ is peaked at zero with an average of 0.9 kcal/mole released to translation. This $P(E_{trans})$ indicates that the dissociation occurs through simple bond rupture from highly vibrationally excited nitrobenzene in the ground electronic state. In this case, the initial photon energy is statistically distributed throughout the molecule. With the reaction coordinate lying along one of many vibrational degrees of freedom, only a small amount of energy is expected to remain along the C-N bond. The resulting $P(E_{trans})$ is peaked at zero translational energy for a simple bond rupture reaction with no exit barrier.[3, 5, 7] The second channel producing phenyl and NO_2 has a slightly higher translational energy release. A $P(E_{trans})$ peaked at 2 kcal/mole was used to fit the faster m/e 46 and m/e 77 data. A $P(E_{trans})$ peaking away from zero indicates there is a small exit barrier or some repulsion which couples energy

into translation of the products. In this case, the dissociation is likely to occur from an excited electronic state.

A comparison of the time-of-flight spectra for m/e 77 ($C_6H_5^+$) and m/e 76 ($C_6H_4^+$), in figure 3.3, shows that the majority of the m/e 76 signal arrives at the detector at the same time as the m/e 77 signal. Therefore, the m/e 76 data is likely to originate from the same neutral product. $C_6H_4^+$ is simply a daughter ion of the C_6H_5 product. This slow signal was fit using the same $P(E_{trans})$s and neutral product masses assigned to reaction (1). There is small additional contribution in the m/e 76 spectrum which arrives earlier than the m/e 77 signal. Additionally, the m/e 46 and m/e 30 TOF spectra have corresponding fast shoulders that have not been accounted for with reaction (1). It is unlikely that this fast signal originates from a third phenyl plus NO_2 channel since there is no momentum matched signal at m/e 77. These fast signals, however, can be attributed to a channel producing benzyne and HONO:

$$C_6H_5NO_2 \xrightarrow{266\,nm} C_6H_4 + HONO. \qquad (2)$$

Although signal was not observed at m/e 47 the parent ion of HONO, the parent ion for C_6H_4 was detected. M/e 30 and 46 are likely to be the major ion fragments of HONO.[3, 19] The $P(E_{trans})$ used for this channel is peaked at 10 kcal/mole with an average of 15 kcal/mole released to translation, as shown in figure 3.5. A $P(E_{trans})$ peaking a non-zero value expected for unimolecular elimination processes. To further confirm the HONO product, signal at OH^+ was monitored. No definitive conclusions could be made from the m/e 17 spectrum, however, due to the poor signal to noise ratio found at m/e 17.

The fast feature arriving at 75 μsec in the m/e 30 time-of flight spectrum, shown in figure 3.6, can result from direct dissociation of nitrobenzene from an electronically excited state to form phenoxy and NO radicals.

$$C_6H_5NO_2 \xrightarrow{266\,nm} C_6H_5ONO \rightarrow C_6H_5O + NO \qquad (3)$$

To confirm the assignment of this channel we checked for signal from the momentum matched C_6H_5O product arriving at the appropriate time. Since IRMPD studies of anisole proved $C_3H_3^+$ and $C_5H_5^+$ are the major fragment ions of phenoxy radicals, signal was monitored at m/e 39 and 65 to find evidence for phenoxy radical formation. Figure 3.7 shows the time-of-flight spectra for m/e 39 and 65. The sharp feature arriving at 160 μsec does in fact momentum match the fast NO signal, confirming the assignment of channel 3. Figure 3.8 shows the $P(E_{trans})$ used to fit the data.

Signal was also monitored at m/e 93 to look for the parent C_6H_5O product. No signal, however, was observed. Our inability to detect the phenoxy radical parent mass may be due to the high internal excitation of the radical. From the conservation of energy, the total energy is partitioned among all the degrees of freedom:

$$E_{avail} = h\nu + E_{int,\ nitrobenzene} - D_o(RO\text{-}NO) = (E_E + E_T + E_V + E_R)_{products}$$

where the available energy is the photon energy plus the initial internal energy of nitrobenzene minus the bond dissociation energy D_o. At 266 nm the photon provides 107.5 kcal/mole. The heats of formation for phenoxy radical and NO product were used to estimate the bond dissociation energy according to the equation:

$$D_o(RO\text{-}NO) = \Delta H_f^\circ(RO^\cdot) + \Delta H_f^\circ(NO) - \Delta H_f^\circ(RONO)\ .$$

which gives $D_o(RO\text{-}NO)$ = 16.8 kcal/mole.[20] An upper limit for the internal energy of the parent molecule is obtained assuming the vibrational modes do not relax in the supersonic expansion. With the nozzle tip temperature at 200°C and the known vibrational frequencies of nitrobenzene,[21] the calculated vibrational energy is 7 kcal/mole. Since the rotational degrees of freedom relax in the expansion, they are expected to have a negligible contribution to the total energy compared to the photon energy. For this channel, the total energy available to the products is 98 kcal/mole and is partitioned among the product electronic, translational, vibrational, and rotational

degrees of freedom. With an average of 33 kcal/mole going into the product translational energy, a substantial amount of energy remains to be distributed among the internal degrees of freedom of the products. This internal energy of the products is likely to enhance the fragmentation of phenoxy radical in the ionizer.

An additional channel was still needed to completely account for all the signal at m/e 30, NO^+. One possible source considered was the secondary photodissociation of the NO_2 and HONO products to give NO:

$$NO_2 \xrightarrow{266nm} NO + O$$

$$HONO \xrightarrow{266nm} NO + OH.$$

The small absorption cross sections at 266 nm for NO_2 ($2x10^{-20}$ cm^2)[22] and HONO (~$5x10^{-20}$ cm^2)[23] suggest secondary photodissociation is unlikely unless NO_2 and HONO are formed with large amounts of vibrational energy; additional vibrational energy may dramatically increase the absorption cross section. In this case, however, it is unlikely that NO_2 and HONO products are formed in high vibrational states. The total energy available for the NO_2 channel and the HONO channel is 43 and 32 kcal/mole, respectively. For unimolecular decomposition following intersystem crossing to the ground electronic state the initial photon energy is statistically partitioned among all the vibrational degrees of freedom of the molecule, therefore NO_2 product should be formed with a minimal amount of internal energy. For the concerted HONO elimination, a large fraction of the excess energy is channeled into translation. It therefore, appears that secondary photodissociation of HONO and NO_2 does not play a role in this system an alternative interpretation needs to be considered.

As there is evidence from the HONO and NO_2 elimination channels that electronically excited nitrobenzene is internally converting, a nitro-nitrite isomerization channel from the ground electronic state is also expected to be present. This is a second possible mechanism for reaction (3) and was observed in the thermal studies[1, 2]. The

remaining m/e 30 signal was fit assuming reaction (3) and using the $P(E_{trans})$ shown in figure 3.8. This $P(E_{trans})$ shows only an average of 13 kcal/mole energy released to translation. With 98 kcal/mole of total energy available to the products (as described above) the phenoxy radical product is formed with an even larger amount of vibrational energy. In this case, C_6H_5O has enough energy to further decompose to cyclopentadienyl radical (C_5H_5) and carbon monoxide; the barrier for this process is 44 kcal/mole. The high probability for phenoxy radical secondary decomposition makes it more difficult to detect any evidence of the momentum matched phenoxy radical product. Evidence for secondary phenoxy radical decomposition, however, can help confirm the presence of this channel.

An additional fast shoulder at 100μsec, which could not be momentum matched with signal at NO or NO_2, was observed in both the m/e 39 and the m/e 65 time-of-flight spectra. (See figure 3.7). Two potential sources of this signal are spontaneous secondary decomposition of the primary products and secondary photodissociation where the primary dissociation products absorb another photon and undergoes further decomposition. In both cases, the product translational energy from the secondary decomposition will add to the translational energy distribution from the initial dissociation process, and therefore generate a fast signal. This is illustrated by the Newton diagram shown in figure 3.9. The primary dissociation phenoxy radical product is represented by the velocity vectors originating at the tip of the beam velocity vector, which is also the center of mass velocity. The velocity vectors for the secondary decomposition products originate at the tip of the velocity vectors for the primary dissociation. Figure 3.9 shows velocity vectors for cyclopentadienyl radical product from the secondary photodissociation of phenoxy radical. A complete Newton diagram for the secondary process would include a secondary circle corresponding to each primary recoil velocity. The laboratory velocity measured for the secondary products is the vector sum of the

initial beam velocity and the recoil velocities for both the primary and secondary dissociations.

The fast signal at m/e 65 and 39 was fit assuming that internally excited phenoxy radical generated via reaction (3) further decomposed to give cyclopentadienyl radical and carbon monoxide. It was not possible to confirm the assignment of this channel since no signal was observed at CO^+ for the secondary decomposition momentum matched fragment. The lack of signal at m/e 28 is not surprising since the detector background is high at m/e 28. Additionally, the large translational energy release found for this channel spreads the products, particularly the lighter mass product, over a large angular range, generating low signal levels at each angle. The slow broad signal for the m/e 65 and m/e 39 time-of-flight spectra were fit assuming $C_5H_5^+$ and $C_3H_3^+$ are fragment ions of the phenyl radical, phenoxy radical, and benzyne products.

Finally, although energetically feasible, there was no evidence for the nitrosobenzene and oxygen atom channel.

3.4 Discussion:

The time-of-flight data indicate that there are three important unimolecular decomposition channels occuring on the ground electronic state: C-N bond rupture to give NO_2 and phenyl radicals, molecular elimination to give HONO and benzyne, and isomerization to phenyl nitrite with subsequent dissociation to NO and phenoxy radical. Both NO_2 and NO elimination were found to also occur via dissociation from electronically excited states.

The $P(E_{trans})$ found for each reaction provides some information about the exit channel of the potential energy surface. As mentioned above, the $P(E_{trans})$ peaked at zero energy for reaction (1) indicates there is no exit channel barrier to form NO_2 and phenyl

radical products from the ground electronic state. In contrast, the $P(E_{trans})$ for reaction (2) is peaked significantly away from zero translational energy release. The observed $P(E_{trans})$ is consistent with those found for concerted molecular elimination reactions where there is a significant reaction barrier in addition to the endothermicity.[9] Typically, a large fraction (up to 70%) of the exit barrier is channeled into product translation. Reaction (2) is likely to occur through a five-membered transition state. With the strained configuration of this transition state, a substantial barrier in the exit channel is expected.

One remaining question regarding reaction (2) is whether the dissociation takes place via the ground or an excited electronic state. It is important to note that the recent thermal decomposition studies did not find evidence for the HONO elimination channel. This can be attributed to several reasons. One is that the rate parameters strongly favor the NO_2 channel. The A factor for HONO elimination from nitroalkanes was found to be $10^{12.4\text{-}12.7}$ compared to an A factor of $10^{15.6}$ found for simple bond rupture.[3] A similar difference in A factors is expected for nitrobenzene. Although the activation barrier for the HONO channel is not known, this channel is estimated to be ~10 kcal/mole more endothermic than reaction (1) from the heats of formation.[20] Both the lower A factor and higher endothermicity of the HONO channel indicate the NO_2 channel will be dominant.

In the thermal experiments, the excitation scheme is quite different than in our UV experiment. In the UV case, all the energy is deposited into the molecule at once when the 266 nm photon is absorbed and the dissociation rates will not determine level of excitation. For the thermal studies, however, a large number of collisions are used to slowly pump the molecule up to higher excitation levels. In this case, the high rate of simple bond rupture will limit the level to which the molecule can be excited. A similar competition between dissociation and further excitation is found for the IRMPD

studies.[3] These factors further favor simple bond rupture over HONO elimination in the thermal studies.

If, however, the HONO channel is accessible in the thermal studies there is another explanation for the lack of evidence for this channel. Under the conditions of the laser pyrolysis[1] and shock tube[2] studies, secondary reactions can hinder the primary product identification. In both thermal experiments radical scavengers were necessary to trap the primary phenyl and phenoxy products and to limit the secondary reactions. The monitored benzene and phenol products were assumed to be from phenyl and phenoxy radicals, respectively. Benzene and phenol, however, may also be generated via secondary reactions of other primary products having ring structure, such as benzyne.

Although the rate parameters strongly favor reaction (1) from the ground electronic state, at the high excitation levels obtained with the UV excitation reaction (2) is more likely to occur in these photodissociation studies compared to the thermal experiments. To further address the question concerning whether reaction (2) occurs on the ground electronic state, it is important to mention recent photodissociation studies of cyclohexene and 1,4 cyclohexadiene which directly compare the $P(E_{trans})$s observed for these two excitation schemes. Zhao et al.'s[7] studies indicate the $P(E_{trans})$ reflects only features in the exit channel; $P(E_{trans})$ was found to be independent of the excitation scheme and the total excitation energy. Zhao et. al. conclude that if the $P(E_{trans})$ obtained for UV excitation is similar to that for IRMPD the dissociation is likely to proceed along the ground potential energy surface. Although, IRMPD data for the photodissociation of nitrobenzene is not available, the $P(E_{trans})$ found for reaction (2) is quite similar to those found for HONO elimination from nitroalkanes in the IRMPD studies by Wodtke et al., as shown in figure 3.5.[3] This supports the hypothesis that HONO elimination from nitrobenzene occurs from the ground electronic state.

Both the recent thermal experiments[1, 2] and the present molecular beam studies suggest a nitro-nitrite isomerization is an important primary decomposition channel for nitrobenzene. Using laser-powered homogeneous pyrolysis, Gonzalez et. al. found the rate parameters for reaction (3) to be log $k_\infty(s^{-1})$=(14.3±1.0)-(65.5±5)/2.3RT.[1] The unimolecular nitro-nitrite rearrangement has been extensively studied for small nitrocompounds such as HONO and nitromethane.[24] In nitroaromatic compounds, the isomerization is thought to take place via the following diradical intermediate initially proposed by Chapman[25]:

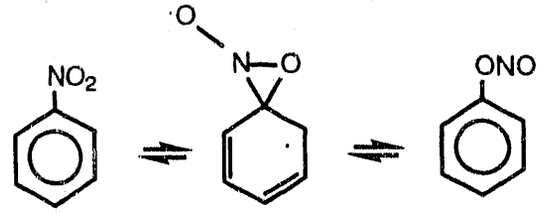

With 266 nm excitation, the TOF spectra for m/e 39, m/e 65, and m/e 30 indicate that reaction (3) may take place from two different potential energy surfaces (PES). The $P(E_{trans})$s obtained for this reaction are shown in figure 3.8. From the substantial translational energy release obtained for the $P(E_{trans})$ peaked at 30 kcal/mole reaction (3) may proceed via an excited electronic state where some of the electronic energy is channeled into translational energy of the products. This $P(E_{trans})$, however, was obtained by fitting the large peak in the m/e 65 and 39 TOFs. Phenoxy radical products which have lower translational energy release will be formed with greater internal excitation and are likely to further dissociate. In this case, the $P(E_{trans})$ found by fitting the m/e 65 and m/e 39 TOFs may not be sensitive to the low translational energy products. The TOF spectrum for NO at m/e 30 suggests, there are products from reaction (3) formed with lower translational energy.

To completely fit the m/e 30 data, a second dissociation channel for reaction (3) was used with a $P(E_{trans})$ peaked at 10 kcal/mole. Although the $P(E_{trans})$ shows there is a relatively low translational energy release for this channel, the fact that the $P(E_{trans})$

peaks away from zero energy contradicts the theoretically predicted translational energy distributions for simple bond rupture reactions where the internal energy is statiscally distributed throughout the molecule. For the simple bond rupture reactions generating two radical products, no exit barrier is expected and the $P(E_{trans})$ is generally peaked at zero energy.[5] This was observed for reaction (1) which occurs from the ground electronic state. A $P(E_{trans})$ peaked away from zero indicates the presence of a barrier in the exit channel.[9]

To determine whether the dissociation occurs on the ground or an excited PES, one must consider whether an exit barrier is likely for this channel. IRMPD studies of anisole (C_6H_5O-CH_3)[6] and ethyl vinyl ether (C_2H_5-$OCHCH_2$)[10] observed exit barriers for the dissociation of carbon-oxygen bonds. In both cases the method of excitation maintains the molecule in the ground electronic state and the translational energy distributions were found to peak at ~3 kcal/mole and extend to ~20 kcal/mole. The exit barrier was attributed to an electronic rearrangement in the formation of C_6H_5O and CH_2CHO radical products due to the partial double bond nature of the C-O bond.

An analogous mechanism is expected for the C_6H_5O-NO bond dissociation with a similar electronic rearrangement as the suggested in the C_6H_5O-CH_3 dissociation studies.[6] Therefore, an exit barrier is expected for this channel and reaction (3) is likely to proceed via the ground electronic PES. It is important to note that the $P(E_{trans})$ obtained for phenyl nitrite decomposition peaks at substantially higher energies than those found in the dissociation of anisole and ethylvinyl ether. The $P(E_{trans})$ peak position found for reaction (3), however, is somewhat ambiguous. Since there are several overlapping contributions to the m/e 30 data as shown in figure 3.6, it is difficult to obtain accurate threshold values for the $P(E_{trans})$.

In both channels which produce phenoxy radical and NO, there is 98 kcal/mole of energy available. For the two dissociation channels, the average translational energy

release was 13 and 33 kcal/mole respectively. This leaves 85 and 65 kcal/mole to the electronic, vibrational and rotational product degrees of freedom. Since the first electronic state of NO is ~4.6 eV above the ground state[26] and NO has only one vibrational degree of freedom, a large majority of the energy will remain as internal excitation of the phenoxy radical. It has been well established that phenoxy radicals with a high degree of internal excitation can undergo secondary decomposition to produce cyclopentadienyl radical and carbon monoxide.[6, 15, 16]

$$C_6H_5O\cdot \rightarrow C_5H_5\cdot + CO \qquad (4)$$

Kinetic studies by Lin et. al. found an activation energy of 44.0±0.9 kcal/mole and an A factor of $2.5x10^{11}$ s^{-1} for the unimolecular decomposition of phenoxy radical.[16] Colussi et al. initially proposed that the reaction occurs via a tight complex, as shown below, rather than a ring opening process.[15]

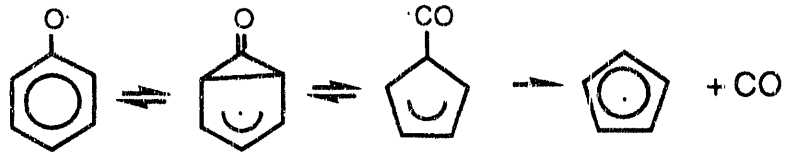

While the signal to noise ratio at m/e 28 was too poor to observe the CO product from reaction (4), the fast signal at m/e 65 and 39 indicates secondary decomposition is in fact occuring. The possible sources for C_5H_5 secondary decomposition are spontaneous dissociation and secondary photodissociation from both channels which form C_6H_5O. To determine which process is more likely one has to consider whether phenoxy radical can absorb a 266 nm photon. The UV absorption spectrum of phenoxy radical[27, 28] shows phenoxy radical has a strong absorption band around 240 nm. Although this band drops off before 266 nm, the absorption band is likely to shift significantly to the lower energies for phenoxy radicals with a high degree of internal excitation. Therefore C_6H_5O is likely to absorb at 266 nm. Since the phenoxy formed

via the ground state dissociation channel has more internal energy, it is more likely to absorb a 266 nm photon than the phenoxy radical formed from the excited state dissociation channel.

The fast m/e 39 and m/e 65 signal can be fit assuming phenoxy radical from either channel decomposes. If the fast m/e 39 and m/e 65 is from phenoxy radical formed from the slow reaction (3) channel, a substantial amount of translational energy is needed to fit the fast edge of the m/e 39 and m/e 65 TOF spectra. The $P(E_{trans})$ is shown in figure 3.10a. In contrast, a slower secondary $P(E_{trans})$ can be used, assuming the phenoxy radical from the fast reaction (3) channel undergoes secondary decomposition. The $P(E_{trans})$ for this process is shown in figure 3.10b. The later $P(E_{trans})$ suggests secondary decomposition occurs via a spontaneous process along the ground state PES. This hypothesis is supported by comparing the $P(E_{trans})$ obtained for phenoxy radical decomposition using IRMPD[6] with the $P(E_{trans})$ found in this study, as shown in figure 3.10. In the IRMPD experiment the phenoxy radical products were released with an average of ~20 kcal/mole. The $P(E_{trans})$ was peaked at 14 kcal/mole with a maximum energy release of 48 kcal/mole. With infrared multiphoton excitation, the phenoxy radical decomposition proceeds along the ground PES, therefore the large translational energy release results from a barrier in the exit channel. Although secondary decomposition can result from either spontaneous dissociation or seondary photodissociation, the linear power dependence obtained for the m/e 65 signal suggests spontaneous secondary decomposition of phenoxy radical from the ground PES is likely to be the dominant process. Additionally, both seondary decomposition of both phenoxy radical channels are expected to contribute to the signal.

Finally, an infrared multiphoton dissociation study of nitrobenzene would be helpful to determine the activation energies for simple bond rupture, isomerization and HONO elimination channels from highly vibrationally excited nitrobenzene. Table 3.2

lists the four fundamental vibrational frequencies of nitrobenzene[21] which match the wavelengths from a CO_2 laser.[29] If nitrobenzene has a reasonable absorption cross section at these wavelengths, it is possible to excite the molecule up to the dissociation limit via resonant and non-resonant absorption of many IR photons.[5] In contrast to the UV excitation scheme, the primary dissociation products from IRMPD would not be formed with such high internal excitation since unimolecular dissociation competes with continued photon absorption at levels above the dissociation threshold. Under these conditions, if the phenoxy radical is formed it will not have as much internal excitation and should live long enough to reach the detector. With IRMPD, it is more feasible to determine the presence or absence of the nitro-nitrite isomerization channel. $C_6H_5O^+$, the parent ion of phenoxy radical has been detected in the IRMPD study of anisole.[6] IRMPD studies of nitrobenzene would also be helpful in determining the barrier height for the HONO elimination and isomerization channels based on the relative yield of the reaction channels.

3.5 Conclusion:

Photofragmentation translational spectroscopy has been used to identify the primary dissociation channels for nitrobenzene excited by a 266nm photon. Five primary dissociation channels were identified. Simple C-N bond rupture, molecular elimination of HONO, and nitro-nitrite isomerization followed by C_6H_5O-NO bond dissociation occur from the highly vibrationally excited ground electronic state. Additionally, isomerization to give NO and phenoxy radical and a second NO_2 plus phenyl radical channel occur along electronically excited potential energy surfaces. Finally, the secondary photodissociation of phenoxy radical to give carbon monoxide and cyclopentadienyl radical was observed.

3.6 References:

1. A. L. Gonzalez, C. W. Larson, D. F. McMillen and D. M. Golden, J. Phys. Chem. **89**, 4809 (1985).

2. W. Tsang, D. Robaugh and W. G. Mallard, J. Phys. Chem. **90**, 5968 (1986).

3. A. M. Wodtke, E. J. Hintsa and Y. T. Lee, J. Phys. Chem. **90**, 3549 (1986).

4. C. W. Hand, C. Merritt and C. DiPietro, J. Org. Chem. **42**, 841 (1977).

5. P. A. Schulz, A. S. Sudbo, D. J. Krajnovich, H. S. Kwok, Y. R. Shen and Y. T. Lee, Ann. Rev. Phys. Chem. **30**, 379 (1979).

6. A. Schmoltner, D. S. Anex and Y. T. Lee, J. Phys. Chem. **in press**, (1991).

7. X. Zhao, R. E. Continetti, A. Yokoyama, E. J. Hintsa and Y. T. Lee, J. Chem. Phys. **91**, 4118 (1989).

8. D. J. Krajnovich, Ph.D., University of California, Berkeley, 1983.

9. S. A. Sudbo, P. A. Schulz, Y. R. Shen and Y. T. Lee, J. Chem. Phys. **69**, 2312 (1978).

10. F. Huisken, D. Krajnovich, Z. Zhang, Y. R. Shen and Y. T. Lee, J. Chem. Phys. **78**, 3806 (1982).

11. C. A. G. O. Varma, F. L. Plantenga, A. H. Huizer, J. P. Zwart, P. Bergwerf and J. P. M. Van Der Ploeg, J. Photochem. **24**, 133 (1984).

12. S. Nagakura, M. Kojima and Y. Maruyama, J. Mol. Spectros. **13**, 174 (1964).

13. A. Gonzalez-Lafont, J. M. Lluch, J. Bertran and J. Marquet, Spectrochimica Acta **44A**, 1427 (1988).

14. F. Zuccarello, S. Millefiori and G. Buemi, Spectrochimica Acta **35A**, 223 (1979).

15. A. J. Colussi, F. Zabel and S. W. Benson, Int. J. Chem. Kinet. **9**, 161 (1977).

16. C. Y. Lin and M. C. Lin, J. Phys. Chem. **90**, 425 (1986).

17. *CRC Handbook of Chemistry and Physics* (CRC Press, Inc., Boca Raton, Florida, 1981).

18. Zhao, Ph.D., University of California, Berkeley, 1988.

19. G. N. Spokes and S. W. Benson, J. Amer. Chem. Soc. **89**, 6030 (1967).

20. S. G. Lias, J. E. Bartmess, J. F. Liebman, J. L. Holmes, R. D. Levin and W. G. Mallard, *Gas-Phase Ion and Neutral Thermochemistry - Supplement No. 1* (American Institute of Physics, New York, 1988).

21. J. H. S. Green and D. J. Harrison, Spectrochimica Acta **26A**, 1925 (1969).

22. A. Bass, A. E. Ledford and A. H. Laufer, J. Res. Natl. Bureau Stands. **80**, 143 (1975).

23. H. Okabe, *Photochemistry of Small Molecules* (John Wiley and Sons, Inc., New York, 1978).

24. B. M. Rice and D. L. Thompson, J. Chem. Phys. **93**, 7986 (1990).

25. O. L. Chapman, D. C. Heckert, J. W. Reasoner and S. P. Thackaberry, J. Amer. Chem. Soc. **88**, 5550 (1966).

26. V. Hansson and R. W. Nicholls, J. Phys. B: Atom. Molec. Phys. **4**, 1769 (1971).

27. Y. Kajii, K. Obi, N. Nakashima and K. Yoshihara, J. Chem. Phys. **87**, 5059 (1987).

28. J. L. Roebber, J. Chem. Phys. **37**, 1974 (1962).

29. CO_2 Laser Spectrum Analyzer, (Optical Engineering, Inc., Santa Rosa, CA)

30. S. W. Benson, *Thermochemical Kinetics* (Wiley, New York, 1977).

31. A. Yokoyama, X. Zhao, E. J. Hintsa, R. E. Continetti and Y. T. Lee, J. Chem. Phys. **92**, 4222 (1989).

32. S. K. Pollack and W. J. Hehre, Tetrahedron Lett. **21**, 2483 (1980).

3.7 Tables:

Channel	$\Delta H_{reaction}$[a] (kcal/mole)	Available Energy (kcal/mole)
—		
$C_6H_5NO_2 \rightarrow NO$ + phenoxy	17	98
$C_6H_5NO_2 \rightarrow NO + C_5H_5 + CO$	38	77
$C_6H_5NO_2 \rightarrow NO_2$ + phenyl	72	43
$C_6H_5NO_2 \rightarrow HONO$ + benzyne[b]	83	32
$C_6H_5NO_2 \rightarrow O(^3P)$ + nitrosobenzene	92	23

Table 3.1 Energetics for various dissociation channels at 266 nm.
[a] heats of formation from [20, 30]
[b] heats of formation of benzyne (118±5) from [31, 32]

Nitrobenzene Vibrational Frequency (cm^{-1})	CO_2 Laser Frequency	CO_2 Transition
935	934.92	$00^01\text{-}10^00$ P(30)
977	977.23	$00^01\text{-}10^00$ R(22)
990	990.78	$00^01\text{-}10^00$ R(46)
1071	1071.88	$00^01\text{-}02^00$ R(10)

Table 3.2 Fundamental frequencies of Nitrobenzene[21] which match CO_2 laser lines.[29]

3.8 Figures:

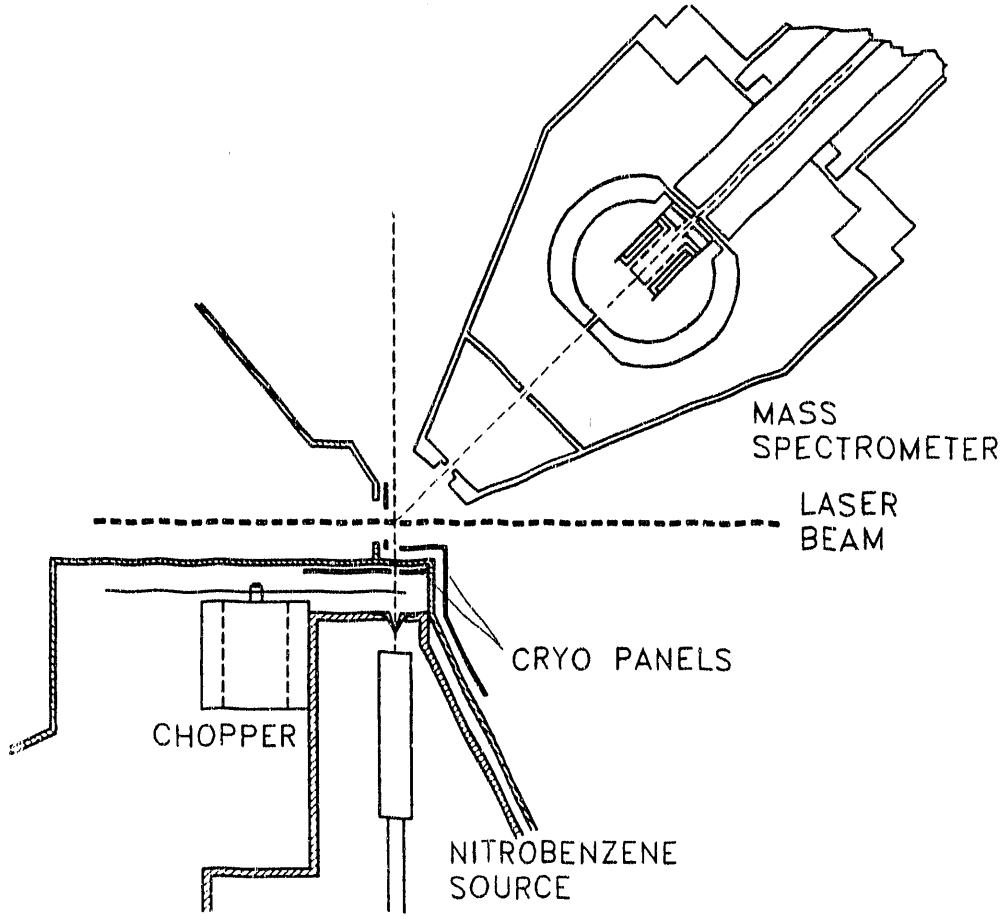

Figure 3.1: Schematic view of crossed molecular beams apparatus modified for photodissociation studies. Molecular beam was chopped with a wheel in the differential pumping region to reduce background in the main chamber.

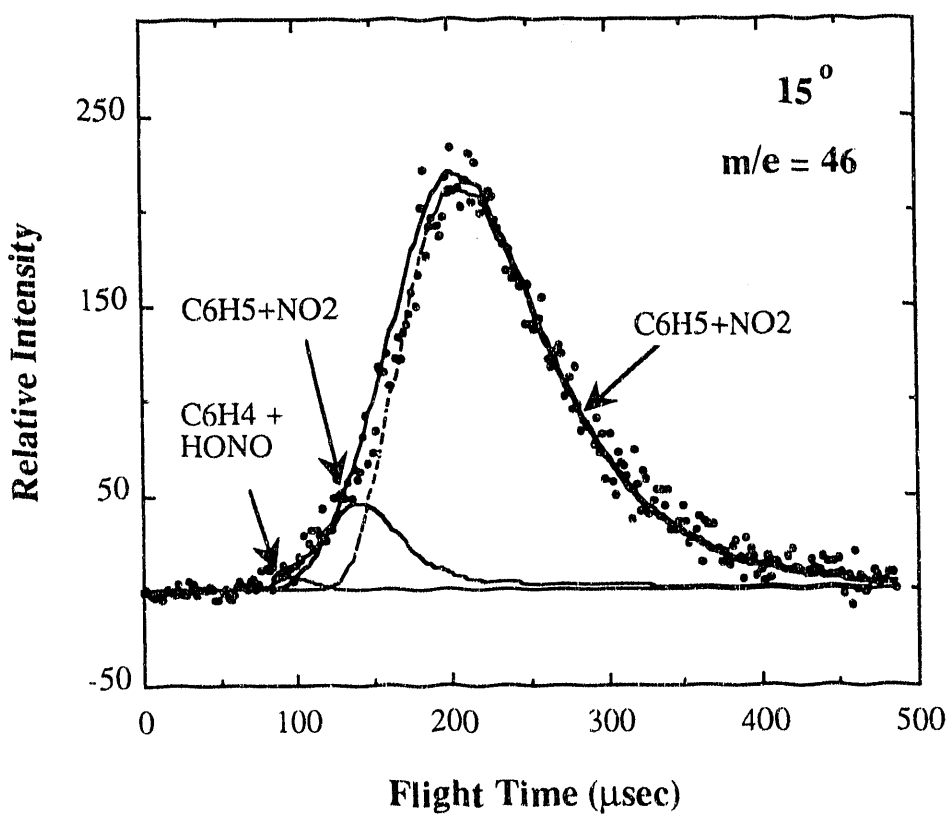

Figure 3.2: Time of flight spectrum for m/e 46 at 15°.

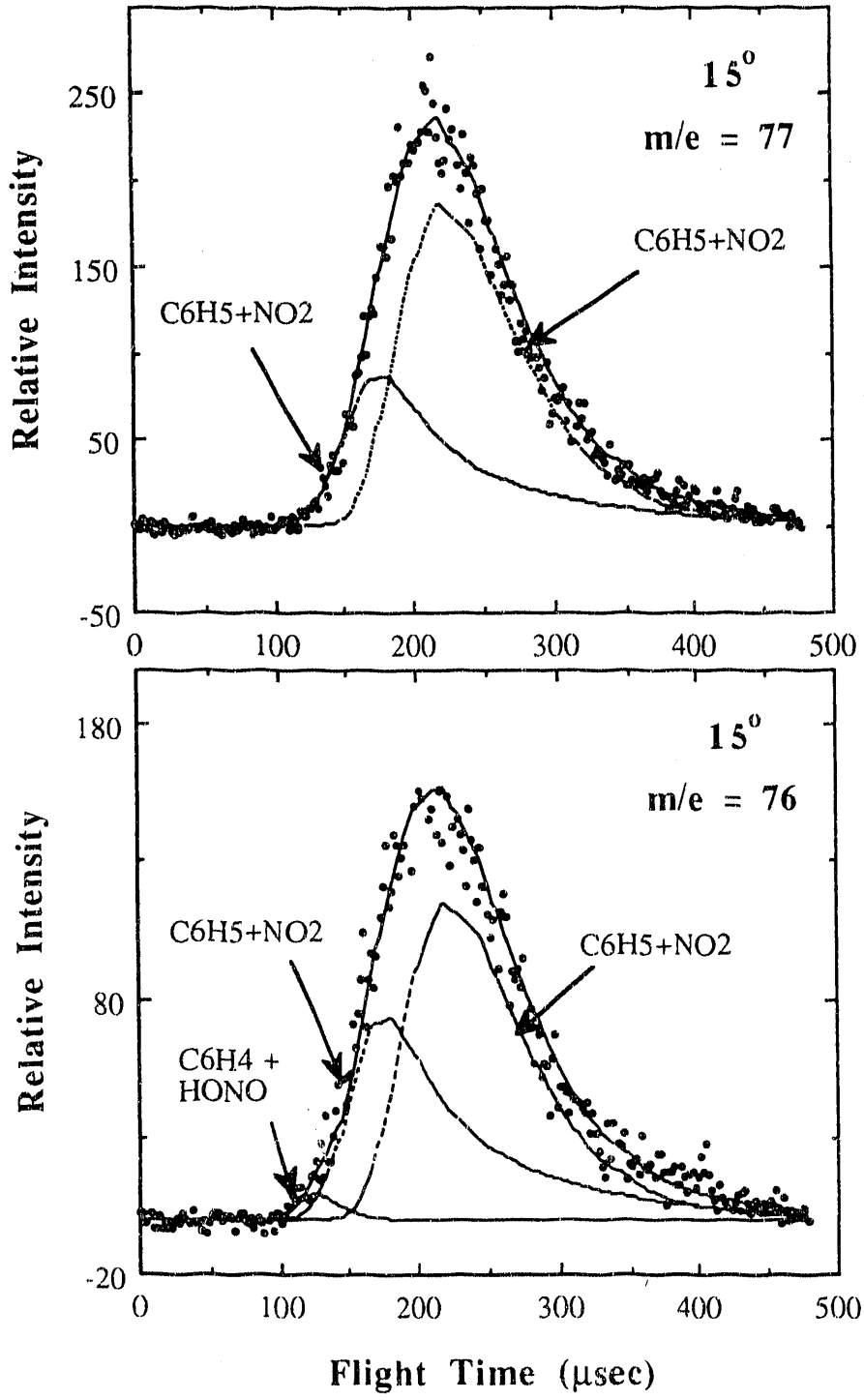

Figure 3.3: Time of flight spectrum for m/e 77 and m/e 76 at 15°.

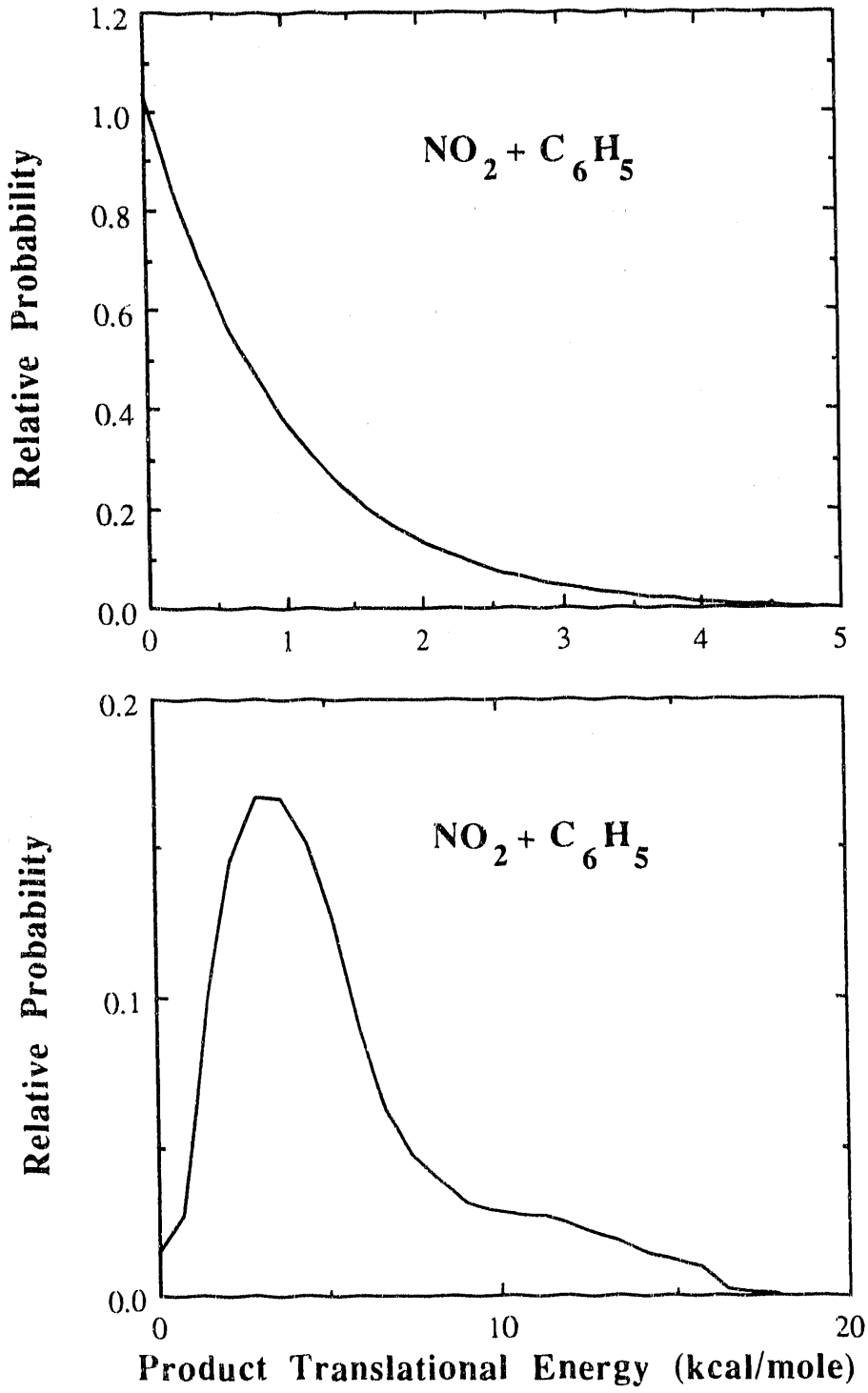

Figure 3.4 Translational energy distributions $P(E_{trans})$ for reaction (1).

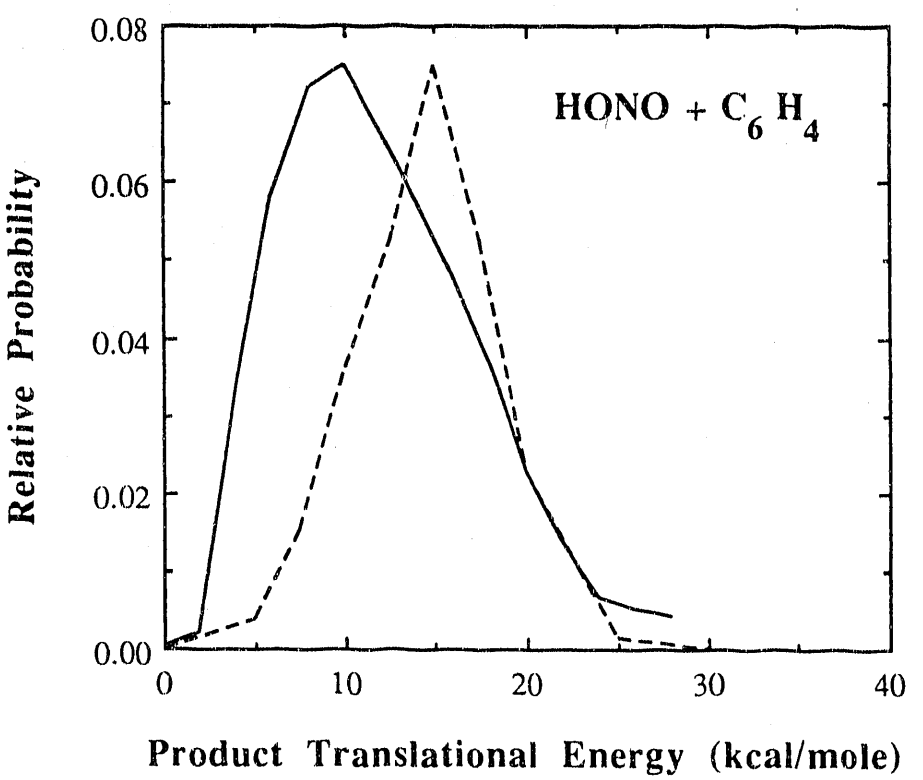

Figure 3.5: Translational energy distribution for reaction (2). Solid line represents $P(E_{trans})$ obtained for this study. Dashed line represents $P(E_{trans})$ obtained for HONO elimination from nitropropane in IRMPD studies by Wodtke et al..[3]

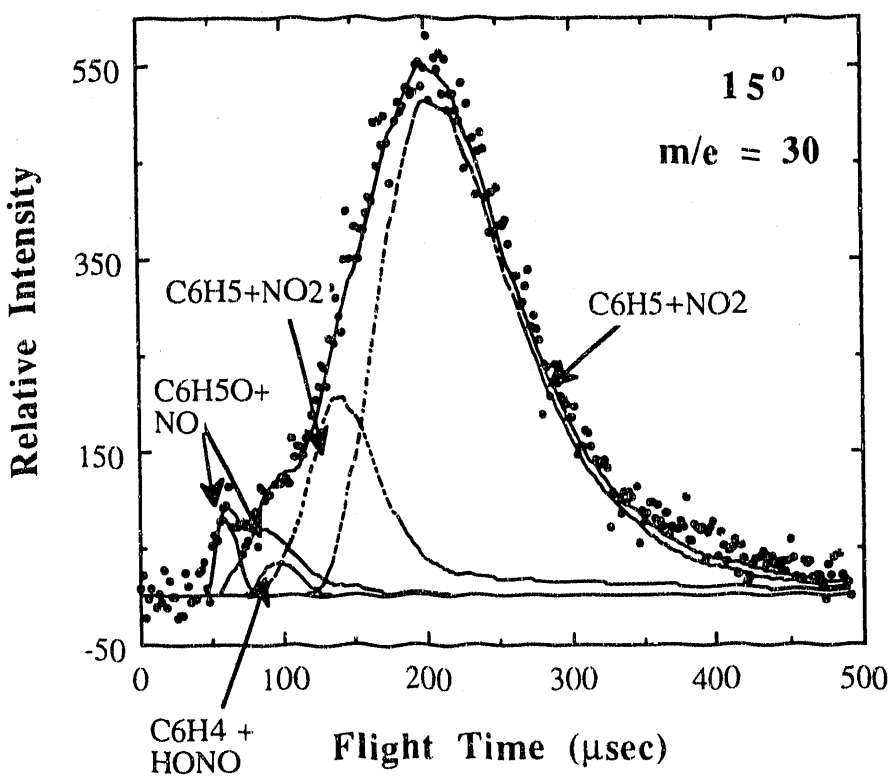

Figure 3.6: Time-of-flight spectrum for m/e 30 at 15°.

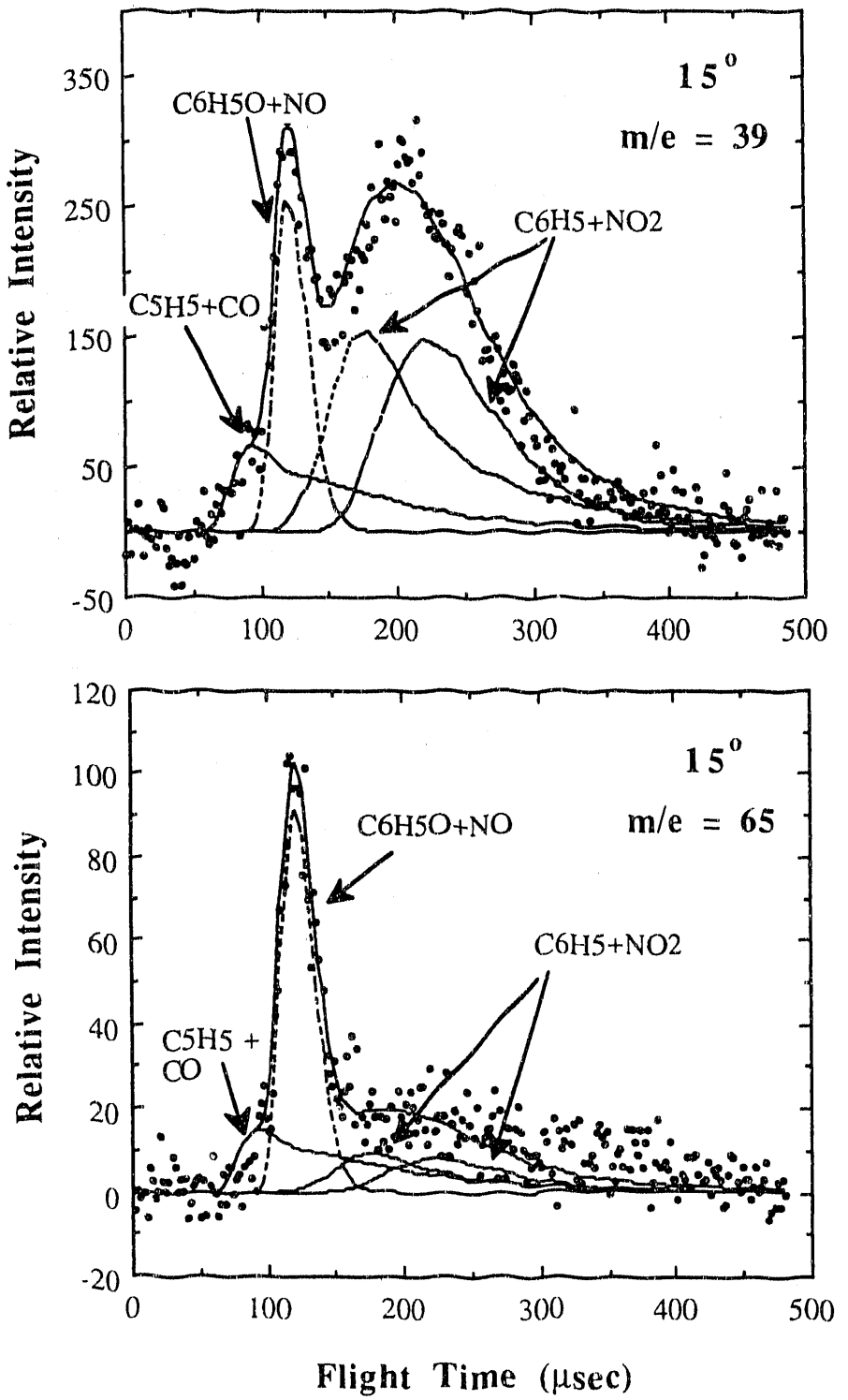

Figure 3.7: Time-of-flight spectrum for m/e 39 and m/e 65 at 15°.

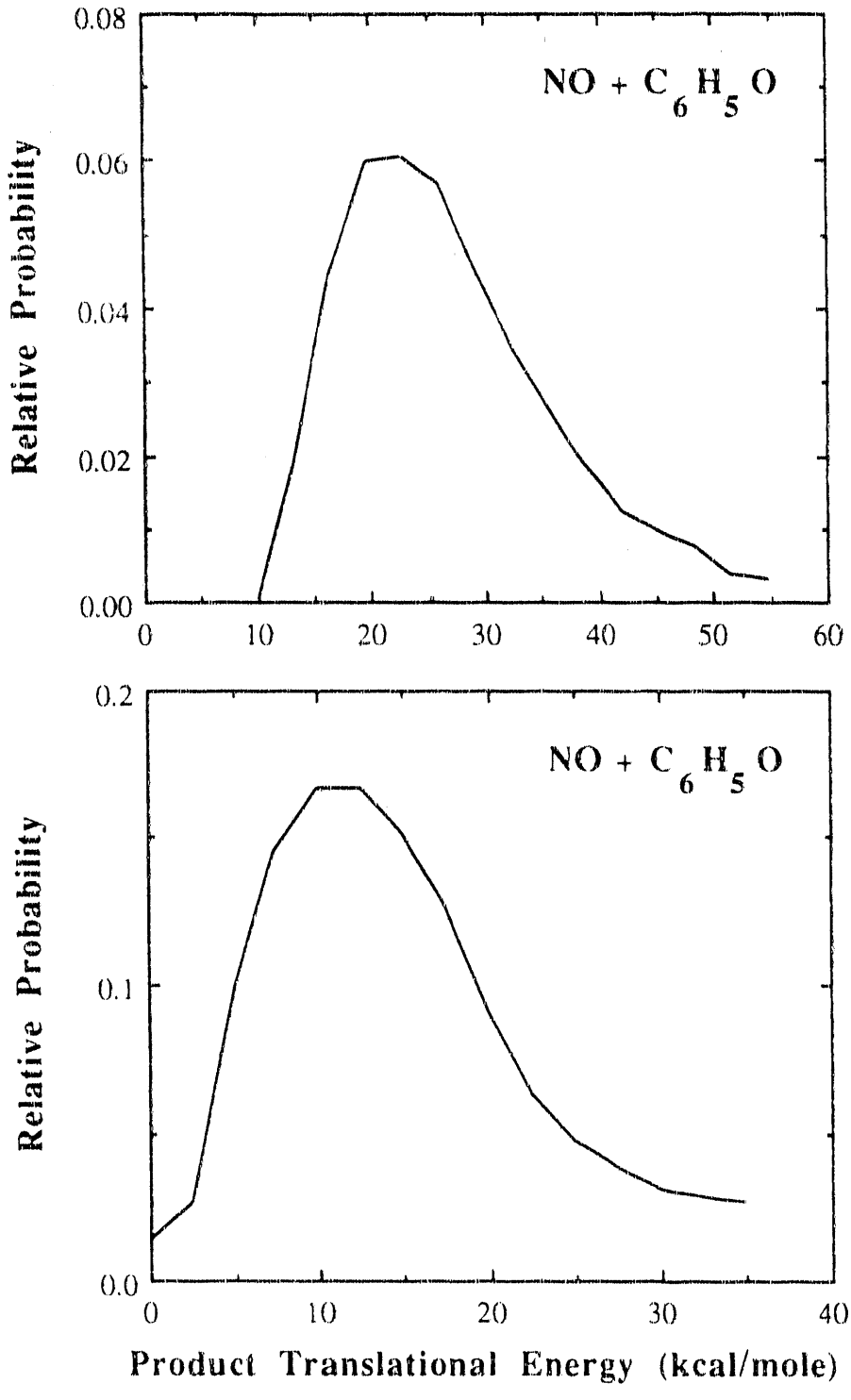

Figure 3.8: Translational energy distributions for reaction (3).

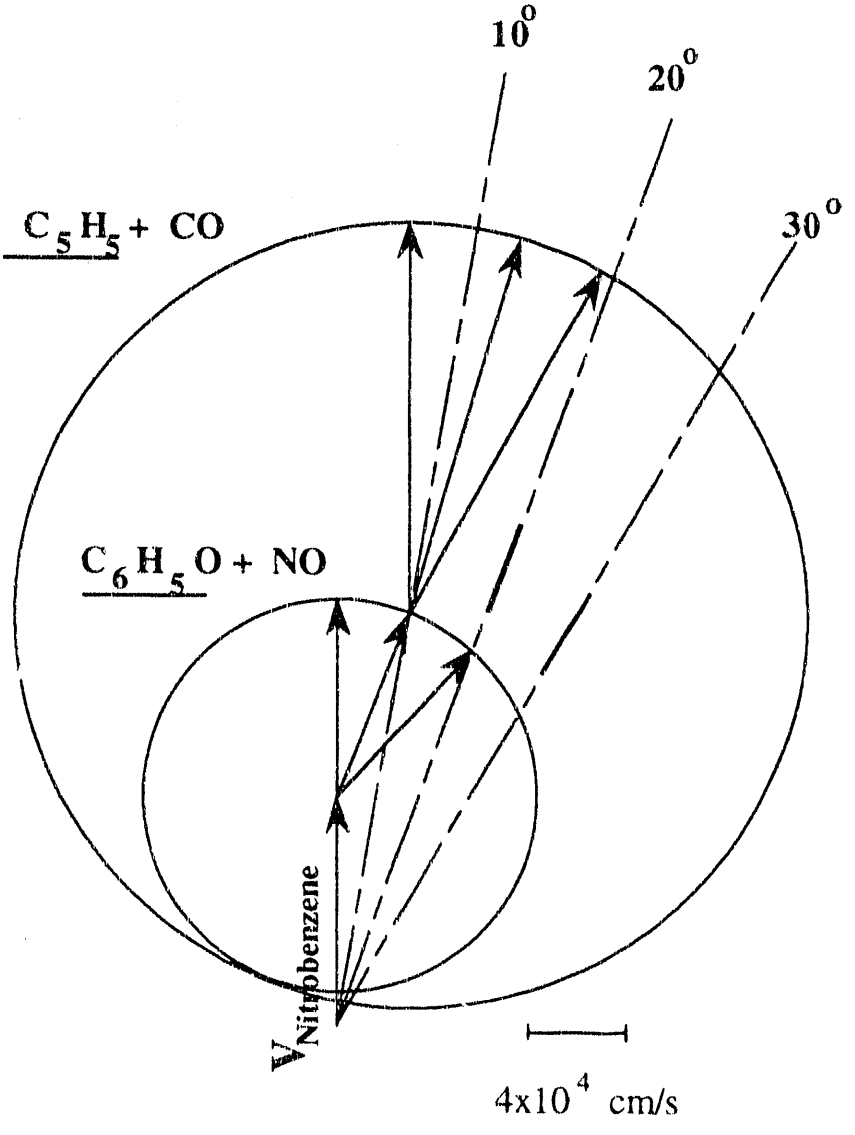

Figure 3.9 Newton diagram illustrating primary and secondary dissociation channels. Vectors originating at the tip of the beam velocity vector represent the phenoxy radical primary dissociation product. Velocity vectors originating from tip of phenoxy radical vector correspond to the cyclopentadienyl radical secondary photodissociation product.

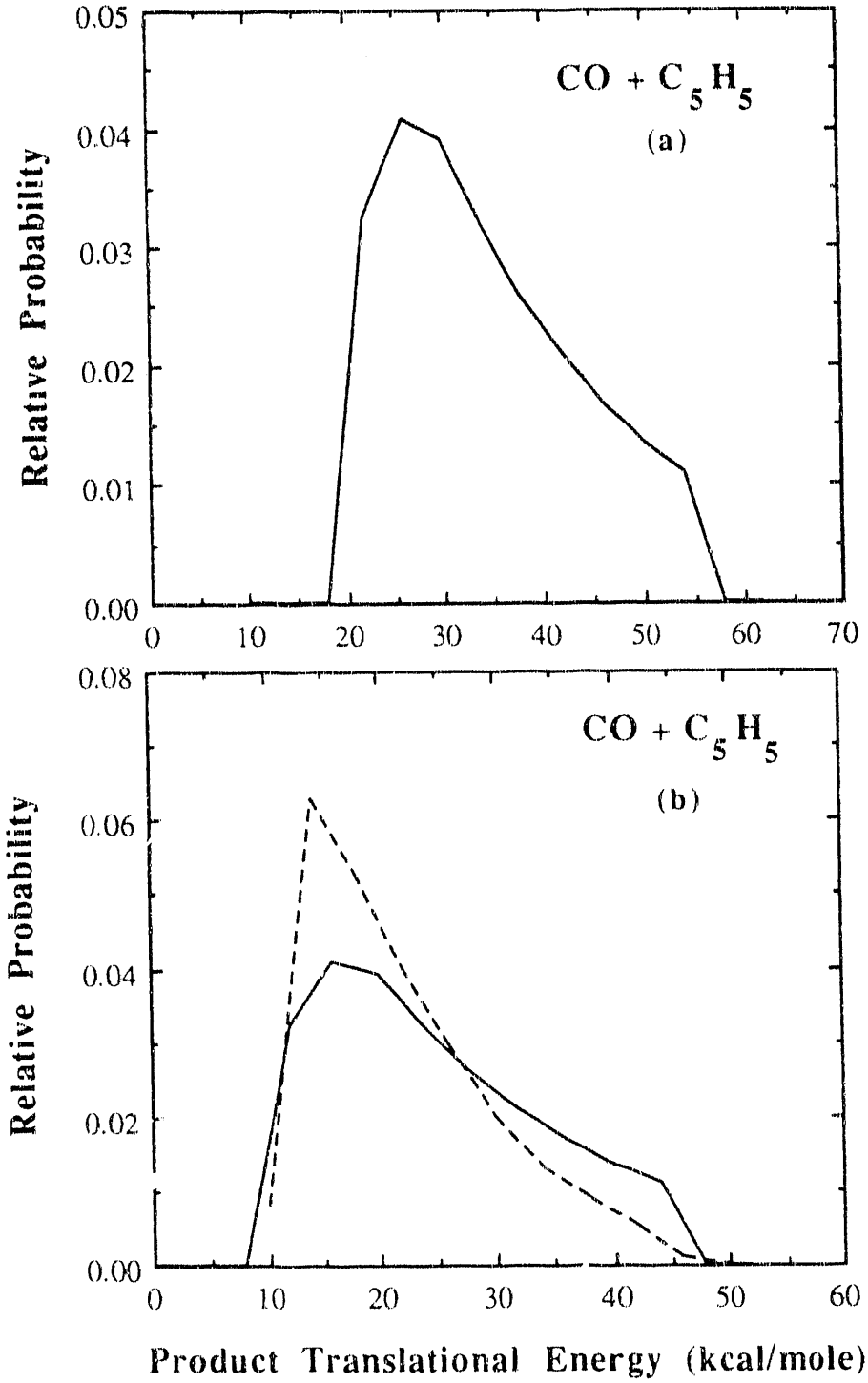

Figure 3.10: Translational energy distributions for secondary decomposition of phenoxy radical. Panel (a) shows $P(E_{trans})$ needed assuming all fast signal originates from the slow phenoxy channel. Panel (b) shows $P(E_{trans})$ needed assuming fast phenoxy channel undergoes secondary decomposition. Solid line represents $P(E_{trans})$ found for this study. Dashed line represents $P(E_{trans})$ found for secondary decomposition of phenoxy radical in IRMPD studies of anisole by Schmoltner et al.[6]

Chapter 4:

A Methyl Radical Source

4.1 Introduction:

This chapter describes the development and characterization of a new design for a supersonic methyl radical beam source. With an intense radical beam accompanied by several recent additional modifications to the universal crossed molecular beam machine, we hoped to improve the potential of studying the dynamics of larger variety of radical-molecule and radical-radical reactions under single collision conditions. To date, only a limited number of successful methyl radical reactive scattering experiments have been performed. These include studies of methyl radicals and halogen molecule reactions using effusive methyl beam sources and, more recently, supersonic radical beam sources.

The production of a free radical beam is relatively straightforward when carried out with an effusive pyrolysis source. In this case, the molecular flow at the source exit maintains the radical recombination through collisions to a minimum. Two great disadvantages of these sources, however, are the low number densities and the broad velocity distributions of the radical beams. These characteristics make it particularly

difficult to study reactions with small cross sections, as in the case of methyl radical reactions, where low A factors and high activation energies are common in the measured macroscopic rate constants for a wide range of reactions. The broad velocity distributions also restrict the dynamical information one can obtain from the scattering experiments, especially when the cross sections are strongly dependent on the collision energies.

Several pyrolysis sources[1, 2, 3, 4, 5, 6] have been modelled after the initial design of Kalos and Grosser.[7] Molecules effused with a Maxwell Boltzmann velocity distribution from a bundle of three 0.75 mm diameter tubes made from 0.025 mm thick tantalum foil . The tubes were heated by radiation and electron bombardment to 1400-1600K. Typically, the heated tube lengths ranged from 1-3 cm for these sources to maintain short contact times and prevent free radical recombination. A number of radical precursors ranging from dimethyl mercury, dimethyl zinc, trimethyl bismuth, methyl iodide and azomethane have been used. To obtain pure alkyl beams, the remaining parent molecules, as well as the high mass decomposition products, were removed from the beam by a slotted disk velocity selector. Mixtures of $Hg(CH_3)_2$ and helium have been used to give an increased peak velocity. The width of the velocity distribution in these beams, however, remained relatively broad. With source backing pressures of 0.2-3.0 Torr, intensities on the order of $5x10^{15}$ radicals sr^{-1} s^{-1} have been achieved with these sources.

Supersonic sources have also been used to generate methyl radicals for reactive scattering experiments as well as for spectroscopic studies.[8, 9, 10] In general, the supersonic nozzle designs are quite similar to the effusive beam sources. Typically, the heated zones were confined to the front tip of the source and were about 1-3 mm long to minimize radical recombination. Clogging was a common problem found with the higher backing pressures and smaller orifices of the supersonic radical sources. To lengthen the

nozzle lifetimes, the tantalum tube heaters were often replaced by quartz or ceramic tubes heated by thermal contact. Recently, a pulsed CH_3 supersonic beam source was used to study the resonant multiphoton spectrum of rotationally cold radicals. [11] In this nozzle design, the estimated contact time in the heated region was ~100 μsec.

In the Lee group [12], a supersonic methyl radical beam source similar to one designed by Hoffman et. al.[9] was used to study the reactive scattering of methyl radicals with halogenated hydrocarbons. In this design a tapered quartz capillary tube was heated by a tantalum heating element over a 1mm length at the nozzle tip with a 0.5 mm i.d.. A dilute mixture of 1 Torr ditertiary butyl peroxide in ~70 Torr He buffer gas was expanded through the nozzle tip which was held at ~1000°C. There were several points we hoped to improve upon by designing a new source. One is the low number density of methyl radicals. Another was the fact that the source clogged within a few hours with a black polymeric residue.[12] Both of these problems can be attributed to the long residence time of the methyl radical in the heated source region. It was also found that the tantalum heater reduced the quartz nozzle to silicon over time, requiring periodic replacement of the heating element and quartz nozzle. This chapter describes the design of a new source to try and overcome these problems.

4.2 Source Design:

Atomic and radical beams have been produced by numerous methods including pyrolysis, discharges and photolysis. Since there are many organic molecules that thermally decompose to give methyl radicals, a pyrolysis source is by far the most straightforward technique to generate CH_3. For atomic beams, the extent of dissociation in a pyrolysis source is simply dependent on the source temperature and on the

equilibrium constant. Since the dissociation temperature of halogens is relatively low, intense beams of Cl, Br, and I are possible.[13] The design of polyatomic radical beam sources is more challenging. In this case, recombination reactions to form more stable species than the initial radical precursor compete with the radical production and therefore limit the beam intensity. The new nozzle source was designed to optimize the methyl radical production while minimizing methyl radical recombination. To achieve this, two factors were taken into consideration: the temperature profile of the nozzle and the radical precursor residence time in the heated portion of the nozzle.

The basic design was modelled after a source recently used in the Lee group to generate a beam of NO_3 radicals by the thermal dissociation of N_2O_5.[14] The methyl radical beam source design is shown in figure 4.1. To generate methyl radicals from azomethane requires a much higher source temperature than the dissociation of N_2O_5 to form NO_3, ~1200K versus ~600K respectively. The major modifications of the N_2O_5 source included changes in the dimensions of the heater and the heater materials to accomodate the higher temperatures required. For the CH_3 source, the dimensions of the heated tube and tip front plate were optimized to insure that the hottest part of the nozzle tube was concentrated close to the tip. To achieve this, the front plate was changed from a disk, as used in the NO_3 source, to a simple strip. Using the thermal conductivity and resistivity of the source materials, a model was generated to calculate the temperature profile of the source as a function of tube and plate dimensions, as well as of current. A full description of this model has been included as an appendix to this chapter.

Supersonic sources have a tendency to form clusters. In the radical beams, this condensation results in contamination by recombined stable molecules as well a decreased number density of the species of interest. To avoid large amounts of clustering, while retaining a reasonable beam number density, we used a larger nozzle diameter d than that used in typical supersonic beam sources: the beam number density

scales as $P_o d^2$, while the number of collisions in the expansion is proportional to $P_o d$, where P_o is the pressure behind the nozzle. This increased nozzle diameter of the CH_3 source required a greater pumping speed to handle large gas throughputs. A roots blower with mechanical pump were used to back the source diffusion pump. This greatly enhanced our pumping speed, particularly for helium, the seed gas.

The dimensions of the heater tube and their effect on the gas residence time in the pyrolysis area was also an important consideration. The CH_3 source has a 0.080" channel length with a residence time of ~10μsec assuming 100 Torr backing pressure, 0.020" diameter nozzle, and 5,000 l/sec source pumping speed. Although several different channel lengths were tested, this length was found to be the optimum.

The basic design of this new source, shown in figure 4.1 and 4.2, consisted of two water cooled electrodes attached to the front of a stainless steel tube with 0.25" o.d.. A heater tube was inserted into a molybdenum front cap, which was vacuum brazed to the stainless steel tube. The heater tube had two sections. The back portion was 0.060"long with a 0.08" o.d. and 0.030" i.d.. The front portion was 0.50" long with the o.d. ground down to 0.050". The nozzle was directly heated by passing current through the tube. To maintain good electrical contact while the source was heated from 300 to 1600K, the heater tube was spring loaded between the molybdenum cap and the front plate. Since the juntions between the heater tube and the molybdenum cap and between the heater tube and the front plate are likely to be points of high resistance, the front contact point was made ~1/4 the area of the back to keep the hottest portion of the tube at the tip. One attractive feature of this design was that it was not necessary to maintain good thermal contact between a heater and the tube, which in turn heats the gas. This is in contrast to the quartz nozzle with the tantalum heater. For that case, if the thermal contact is poor, the heaters need to run at higher temperatures, and tend to burn out easily.

During the testing phase of the source, it was necessary to modify the material used for the heated section of the source. The initial material tested was Inconel, a high temperature stainless steel alloy. Inconel should be relatively resistant to reactions with the methyl radicals and should withstand temperatures up to 1600K. In practice, the spring loading stress accompanied by the high temperatures caused the front plate to warp. The Inconel parts were substituted with molybdenum which can tolerate much higher temperatures. The melting point of molybdenum is 2617°C compared to ~2000°C for Inconel.[15] Molybdenum, however, reacted with the methyl radicals at these high temperatures. This source successfully generated methyl radicals, but the tube tended to clog and degrade within four hours. Since the tube wall thickness was only 0.005" and typically carried 120 amps, it also burned out quickly.

Tungsten has a much lower carburization rate with methane than does molybdenum, and the high temperature reaction between tungsten and methane is known to produce carbides.[16] Therefore, the molybdenum tube was replaced with tungsten carbide (WC) to minimize the tube degradation. Tungsten carbide, with a 2600-2870° C melting point[15], was also expected to withstand the high temperatures. Although the tungsten carbide tube began to clog after running a beam for eight hours, the tube itself did not appear to react with the beam. The oven resistance remained stable even after the nozzle clogged, and the tube did not burn out. It was possible to clear out the blockage by running a beam of warm air with the heater at 70Watts (~800K) followed by a warm rare gas beam and therefore increase the lifetime of the tube. Even though it was possible to remove the deposits with a warm air beam, it was necessary to periodically replace the tungsten carbide portion of the nozzle. The source design made this procedure relatively easy. Since the molybdenum front plate and heater tube were accessible through the skimmer mounting plate, it was possible to change these parts without having to realign the source. After numerous tests to optimize the oven running conditions, the oven

temperature, the helium to azomethane ratio, and the total beam flux, the source was able to run up to twenty hours with the heater properties and signal level remaining stable.

The original design relied on the back copper electrode to make reasonable electrical contact with the stainless steel tube through a slip fit. The resistance for the whole heater system in this configuration was typically 30 milliohms. From the resistivity of tungsten carbide and the tube dimensions, the resistance of the tungsten carbide piece should only be ~0.50 milliohms. The resistance of the tungsten carbide tube, the resistance at the junctions between the tube and front plate and between the tube and molybdenum cap should give the largest contributions to the total resistance; these are the sections with the smallest cross sectional area and poorest contact. To minimize the resistance of the rest of the heater and to insure that the majority of the power was dissipated at the nozzle tip, an extra back copper electrode, which was soft-soldered to the stainless steel tube, was added. A flexible copper braid was used to connect the two back electrodes to maintain the spring loading.

In general, a measured total resistance for the heater and additional back electrode greater than ~6-12 milliohms at the initial nozzle installation, or during the first heating cycle, indicated a poor contact point between the molybdenum front plate and the tungsten carbide tube. In this case, the nozzle did not have a reliable lifetime and did not generate methyl radicals reproducibly. When this occurred, it was prudent to immediately replace the nozzle and front plate instead of moving on to scattering experiments.

The temperature of the heater tube was determined by measuring the terminal flow velocity of a rare gas beam. The velocity of a nozzle beam is dependent on the temperature of the nozzle tip. On axis beam time-of-flight of argon indicates that the nozzle tip temperature reaches approximately 1300° C at 160 Watts. After running a methyl radical beam for a few hours, the tungsten carbide tube and molybdenum front

plate became discolored at the tip from the heat. The carbon deposits were also concentrated at the very front of the tungsten carbide tube. Both of these findings confirmed that the hottest section is at the front of the nozzle, which was predicted by the model described below.

4.3 The Radical Precursor - Azomethane:

There are a number of molecules which thermally decompose to give methyl radicals. Azomethane was chosen as the radical precursor because its pyrolysis should generate only nitrogen, ethane and methane as beam contaminants. These species should not interfere with the planned methyl radical photodissociation experiments. Tests running ditertiary butyl peroxide in the nozzle showed that more clogging occured with this precursor than with azomethane.

The thermal decomposition of azomethane has been well studied since it was originally believed to undergo unimolecular dissociation and was therefore used to investigate unimolecular rate theory. Further studies have proven that azomethane's decomposition occurs through a complex process involving a short chain reaction. [17] Although the conditions in the expansion are quite different than those in the pyrolysis studies, a close examination of the products and kinetics of the thermal dissociation studies can provide clues about what beam contaminants might be present, as well as help identify the reactions responsible for generating the polymers. Kinetic modelling of the possible recombination reactions can also supply an idea of what might be a feasible range of heater tube residence times for maximizing dissociation and minimizing secondary reactions.

Since nitrogen, methane and ethane are the three most abundant decomposition products found by Paquin and Forst, the three following reactions must dominate the pyrolysis.[18]

$$CH_3N_2CH_3 \rightarrow 2CH_3\cdot + N_2 \quad (1)$$

$$CH_3\cdot + CH_3N_2CH_3 \rightarrow CH_4 + CH_2N_2CH_3\cdot \quad (2)$$

$$CH_3\cdot + CH_3\cdot \rightarrow C_2H_6 \quad (3)$$

Reaction (1) is likely to be a two step process where one carbon-nitrogen bond breaks at a time.[19] When the azomethane is pyrolyzed in the presence of nitric oxide, a methyl radical scavenger, the methane and ethane yield is dramatically reduced, confirming reactions (2) and (3). [17]

To efficiently produce methyl radicals and minimize their loss to secondary reactions, it is necessary to reduce the number of collisions between the methyl radicals and other reactants. This was achieved by diluting the azomethane in a rare gas and by attempting to keep the azomethane dissociation confined to the area just at the nozzle exit. The azomethane decomposition rate, as well as the radical recombination rates, can be used for estimating how the competition between the reactions influence the net CH_3 radical production.

To obtain an order of magnitude estimate of what a reasonable heater residence time might be, a few assumptions were made about the decomposition and recombination reactions. Although it has been established that the azomethane decomposition occurs with a short chain reaction, under our conditions where the azomethane was diluted with helium by a factor of ~30, it was reasonable to assume the decomposition occured through a unimolecular process to form 2 CH_3 and N_2. The rate constant used for this reaction was $k=2.4\times10^{14} \exp[(-47.6\text{kcal/mole})/RT]\ s^{-1}$ as measured by Lin and Laidler.[20] The decomposition rate has a strong temperature dependence, as one would expect for unimolecular reaction processes. The energy required to activate the molecule

is supplied by collisions with the buffer gas through the Lindemann-Hinshelwood mechanism.

In the methyl radical recombination process there is ~88 kcal/mole of energy liberated during the formation of ethane.[21] To stabilize the product molecule, the energy evolved must be distributed among the vibrational degrees of freedom or to a third body, which can easily carry the excess energy away through translation. Under our nozzle conditions the helium buffer gas plays an important role in dissipating this energy. A value of $7.95 \times 10^{-29} \exp[2306/T]$ cm^6 $molec^{-2}$ sec^{-1} from Macpherson and co-workers was used for this termolecular recombination rate.[22]

Acuchem, a computer program to model complex reaction systems was used to estimate the optimum conditions for the methyl radical generation.[23] This program was designed to model spacially homogeneous, isothermal, multi-component chemical reaction systems. Although these conditions do not match those in our nozzle tip, the model should give a reasonable picture of the favorable conditions for methyl radical production. The temperature, initial ratio of buffer gas to azomethane, and the total pressure were varied to explore how changes affected the methyl radical concentration. Acuchem's output gave the concentrations of the reaction components as a function of time.

For the computer program, we assumed that azomethane decomposed via a pseudo-two step process:

$$CH_3N_2CH_3 \rightarrow CH_3N_2\cdot + CH_3\cdot$$

$$CH_3N_2\cdot \rightarrow CH_3\cdot + N_2$$

with k_1 and k_2 as the respective rate constants. The first reaction was set as the rate limiting step and was therefore assigned the value given by Lin and Laidler, $k_1 = 2.4 \times 10^{14} \exp(-47.6\text{kcal/mole/RT})$ s^{-1}. The second reaction was assumed to occur spontaneously and was therefore assigned a large "dummy" value $k_2 = 10^{10}$ sec^{-1}, which is about four

orders of magnitude faster than the azomethane decomposition rate in the temperature range of interest. For this model, it was assumed that only the methyl recombination reaction was responsible for the loss of CH_3. Since the program could not handle termolecular reactions, we assumed the helium buffer gas concentration to be constant and incorporated its value into the termolecular rate to get an effective second-order rate constant.

Figure 4.3 shows the results of the computer kinetic modelling assuming 100 Torr total pressure with 5% azomethane in helium at 1200K. The methyl radical concentration and lifetime were strongly dependent on the initial conditions and this plot represents the results yielding the highest methyl radical concentration for the longest time. Below 1200K, the azomethane decomposition rate drops off rapidly producing only a very low concentration of methyl radicals. At higher temperatures and pressures, the methyl radical concentration drops off drastically, within a μsec. Clearly many simplifications regarding the reactions occurring in the nozzle tip have been made. The plot shows, however, that in order to effectively compete with the recombination reaction, it is critical to have the azomethane dissociation occur at the tip of the nozzle tip and to have the residence time in the heater at a minimum.

4.4 Azomethane Synthesis:

Azomethane was prepared by oxidation of 1,2-dimethylhydrazine with mercuric oxide suspended in water, as previously described by Renaud and Leitch. [24] Briefly, 50 g of 1,2-dimethylhydrazine dihydrochloride was first dissolved in 150 ml H_2O. Then 25 ml 10M NaOH was added to the solution to produce the free amine. This solution was slowly added dropwise through an addition funnel to a suspension of 120 g

mercuric oxide in 250 ml of water while the reaction mixture was stirred continuously at room temperature. A dry ice-acetone slush bath followed by a liquid nitrogen bath was used to trap the liberated azomethane. To enhance the azomethane distillation, the apparatus was maintained at ~200 Torr using a mechanical pump and needle bleed valve. Finally, the collected azomethane was purified by trap-to-trap distillation and by degassing at 77K. This typically generated 20 ml of azomethane for a yield of a 70%. 1,2- dimethylhydrazine and mecuric oxide were obtained from Aldrich and were used without further purification.

Various chlorinated methanes were found to be the major synthetic impurities by Forst and Rice. [17] The mass spectrum of a room temperature azomethane beam, obtained by the procedure described above, revealed a contaminant at m/e 50, the parent ion of CH_3Cl. From the integrated beam time-of-flights at m/e 15, 43, 58, and 50 (CH_3^+, $CH_3N_2^+$, $CH_3N_2CH_3^+$, and CH_3Cl^+), the methyl chloride contamination in the azomethane was estimated to be less then 1%. There was no indication of any other impurities in the azomethane from the mass spectrum.

4.5 Apparatus:

The source characterization was performed in a universal crossed molecular beams machine which has been described in detail previously and is shown in figure 4.4.[25] Two differentially pumped beams were crossed at 90° in the main chamber held at ~$8x10^{-8}$ Torr. A triply differentially pumped detector, consisting of an electron impact ionizer[26], a quadrupole mass spectrometer and a Daly type ion detector, [27] measured the products. The detector rotated in the plane of the two beams and about the 2x2x3 mm collision volume.

The primary methyl radical beam was defined by a 0.025" diameter skimmer 0.50" from the source, as well as a 0.060" x 0.070" defining slit 1.5" from the source. A variety of conditions were used for the methyl radical/azomethane beam in order to optimize for methyl radical production. Typically, the peak in the laboratory velocity of the methyl radical beamwas typically ~$30x10^4$ cm/s with a speed ratio ~5.0. The secondary rare gas beam was produced by expanding 500 Torr of neon or helium through a 0.15mm nozzle at room temperature. This beam was defined to 1.5° full width half maximum angular divergence with a 0.020" diameter stainless steel conical skimmer 0.40" from the source.

Time-of-flight (TOF) spectra of the scattered products were obtained by the cross-correlation method using a pseudo-random sequence chopper wheel mounted in the primary differential region. [28, 29] A trigger pulse from the cross-correlation wheel was used to initiate the ion counting electronics. The flight length for the on axis time of flights, the distance between the cross-correlation wheel and the ionizer, was 24.1 cm. For off axis time-of-flights, the flight length from the collision zone to the ionizer was 20 cm. All the off axis time-of-flights were adjusted for the methyl flight time between the chopper wheel and the collision zone (typically ~14 μsec), the cross-correlation trigger offset, and the ion flight time. [30] The trigger offsets and the distance between the single shot wheel and the ionizer were measured using rare gas beam time-of-flight. Angular scans of the product distributions were produced by integrating the signal in the time-of-flights at various detector positions.

A few modifications were made to the molecular beam apparatus in order to improve the signal to noise ratio for the methyl radical experiments. To minimize background from the methyl radical beam, the cross-correlation wheel was installed in the primary differential region; this is similar to the design used in the collisional deactivation experiments described in chapter 2. With this modification, the chopped

portion of the beam was pumped away before entering the main chamber, therefore reducing the background to some degree. This also helped reduce the time dependent background difficulties we observed with the cross-correlation wheel in previous experiments.[31] Another tremendous advantage of moving the chopper wheel to the differential region rather than having the wheel attached to the rotating detector is that the wheel no longer restricted the angular range of the detector. In the past, either 0°- 50° or 40°-90° in the laboratory frame, could be monitored. With the new arrangement, the full 90° detector rotation was possible without warming and venting the chamber to change the wheel position. Another benefit of having the chopper wheel in the primary differential chamber was the ability to monitor the stability of the methyl radical velocity throughout an experiment by rotating the detector onto the beam axis at any time.

Methyl radical reactions generally have small reaction cross sections and unfavorable kinematics for crossed molecular beam experiments: the light products are likely to be scattered over a large angular range even with a small release in translational energy. Therefore the number density of product molecules is expected to be relatively low. In order to increase the likelihood of observing signal, only one region of differential pumping for the secondary beam was used as shown in figure 4.4. This enabled us to move the secondary source closer and increase the number density by a factor of four since it is dependent on the distance as $\frac{1}{r^2}$. This configuration was also a key improvement in recent reactive scattering experiments where it was difficult to detect time-of-flight of the light fragments due to their broad angular distribution. [32]

Additional liquid helium cooled cryopanels were added to both the main chamber and the primary differential region to further reduce the background. With the main chamber background pressure ~1×10^{-7} Torr, most of the background in the detector from the beam gases can be attributed to molecules which bounce off surfaces and are directed into the detector. This background can be reduced by trapping the molecules on

the surfaces viewed by the detector. The panels were cooled by a Koch closed cycle helium refrigerator to ~10K, as measured by a Lakeshore diode thermocouple. This temperature is significantly below the condensation temperature of most gases. Depending upon the masses and the detector angle, the background count rates were reduced by at least a factor of 10-20 with these cryopanels.

4.6 Source Characterization:

The methyl radical beam was generated by bubbling ~650 Torr of helium gas through azomethane held at -78°C, using a dry ice acetone slush (~20 Torr of azomethane). A needle valve was used to reduce the backing pressure to 100 Torr and maintain the source chamber pressure at ~1-3x10^{-4} Torr. The 3% mixture of azomethane in helium was expanded through the 2.0 mm long resistively heated tungsten carbide tube at various heater powers.

A number of diagnostic techniques were used to characterize the pyrolysis source as a function of heater current. Mass spectrometry of the azomethane/methyl radical beam was used to check for the onset of azomethane dissociation. With on axis beam TOF, however, it was difficult to distinguish between signal due to methyl radicals and signal due to azomethane or other decomposition fragments cracking in the electron bombardment ionizer. A large contribution to the m/e 15 signal is due to fragmentation of azomethane; at room temperature, it is typically six times more likely than m/e 58, the parent ion for azomethane.[33] This problem is enhanced with the heated source, since the ion fragment ratios are known to change with additional vibrational energy.[34]

To evaluate whether simple on axis beam TOF would be a reasonable method to track our methyl radical production, we measured the fragment ion ratios for the three

major fragments of azomethane at room temperature and compared it to the fragment ion ratios when the source was heated. Figure 4.5 demonstrates how the azomethane/methyl radical mass spectrum shifts towards smaller masses as the power is increased. Clearly, the m/e 58 and 43 signals decrease as the oven temperature increases. It is difficult to determine the percentage of methyl versus azomethane in the beam from these on axis diagnostics. At 128 Watts (145 Amps and 0.885 VAC), the percentage of m/e 15 increases significantly over the m/e 58 and 43. This might lead one to believe that a significant amount of azomethane has dissociated when, however, the beam is still >90% azomethane as measured by the crossed beams experiments, as described below. This indicates that with additional vibrational energy, azomethane does fragment to lower masses. In contrast, at 152 Watts heater power (160 Amps and 0.950 VAC) the on axis mass spectrum suggests the beam is predominantly methyl radical since there is almost no signal at either m/e 43 or 58. This was in agreement with the crossed beams results where only a minimal amount of residual azomethane or CH_3N_2 was detected.

Since it was difficult to determine the onset of azomethane dissociation from the on axis mass spectrum, the crossed molecular beams technique was utilized to unequivocally identify the products in the pyrolysis beam source. To differentiate between the azomethane and methyl radicals in the beam and to optimize the conditions for methyl radical production, the mixture of methyl radicals and azomethane was scattered off a rare gas beam. From the conservation of linear momentum, the velocities of two recoiling fragments in the center-of-mass (CM) coordinate frame are inversely proportional to their masses. Therefore, the methyl radical scatters with a much larger CM velocity vector as well as a over a wider angular range, as depicted in the Newton diagram in figure 4.6. In the m/e 15 TOF at 25° in the laboratory frame, the signal contribution from methyl is easily distinguished from the azomethane contribution. Figure 4.7 shows the onset of methyl radical production. At ~130 Watts (150 amps at

0.885 VAC), the TOF at 25° shows that there is predominantly azomethane in the beam, although there is a small shoulder on the fast side which indicates the presence of methyl radicals. As more current was passed through the heater, the methyl radical production increased. Finally, at 152 Watts (160 amps at 0.950VAC) the fast m/e 15 dominated the signal.

To estimate the amount of methyl radicals produced in the beam versus the residual azomethane, other possible dissociation products such as CH_3N_2, as well as contaminants from radical recombination, the angular scans of the m/e 15 and m/e 43 signal at several different heater powers were measured. The m/e 43 signal at the lower heater powers was first used to get a product energy distribution, P(E), and CM angular distribution, $T(\theta)$ for the scattered residual azomethane and/or CH_3N_2. Both of these species are likely to fragment to m/e 15 in the ionizer and therefore should also be present in the m/e 15 TOF's as well. To fit the m/e 43 spectra, two channels were assumed. The first channel was simply a mass 58 ($CH_3N_2CH_3$) recoiling off neon with a P(E) identical to the distribution in the initial collision energies. To fit the slower species in these spectra, a second channel, consisting of a mass 43 particle recoiling off neon with a P(E) peaked close to zero to account for inelastic scattering, was used. Realistic assignments of P(E)'s to channels is difficult in this case, since there is a high probability that there are many different species in the initial beam. The two channels chosen are a simple way to account for the signal at m/e 43. The time-of-flights at m/e 15 can be fit assuming contributions from the m/e 43 channels plus an additional channel from methyl elastically scattering off neon. At 155 watts of heater power, the branching ratio of methyl radical to residual azomethane and/or CH_3N_2 is estimated to be ~90%

Naturally, the CH_3 radical/azomethane beam velocity changed dramatically as a function of the source heater power. The changes in the primary beam velocity and the resulting changes in the Newton diagrams for collisions with neon at 7.9×10^4 cm/s are

shown in table 4.1. These changes in the methyl radical beam velocity generate corresponding shifts in the off axis TOF's. The fast peak is always the methyl radical, not a crack of azomethane and/or other beam contaminants.

We found that the greatest amount of methyl radical production occurred at approximately 150 Watts of power. This corresponds to a source tip temperature of ~1500K from the rare gas TOF. This is much higher than the kinetic modelling results, which showed the highest methyl production at 1200K. It is likely that the vibrational beam temperature lagged behind the translational temperature since the energy transfer rate for T→T is orders of magnitude faster than for T→V.

To optimize the heater residence time, a variety of tungsten carbide tube lengths were tested during the initial methyl radical beam diagnostics. It was also thought that with a more gradual temperature gradient in the heater, it might be possible to dissociate the azomethane at a lower temperature and therefore not push the heater to such extreme conditions. With longer tubes, as the nozzle was heated, the m/e 58 signal from azomethane would decrease. Although the on axis beam time-of-flight usually showed an increase in the m/e 15 fragment under these conditions, the m/e 15 signal from elastically scattered methyl radical did not appear. This lack of methyl radical signal was attributed to recombination of the methyl radicals during the longer residence time in the heater.

One can expect the recombination rate to be strongly dependent on the carrier gas. Larger carrier gases such as neon and argon are likely to produce more recombination under the same conditions since they have much larger collision cross sections. During the testing phase of the source we tried using argon as the carrier gas. We were able to decrease the m/e 43 signal from scattered azomethane which indicated we were heating up the azomethane. No fast signal from the methyl radical appeared in the crossed beams

experiment. Running under the same conditions, but using helium as the carrier gas, we were able to generate a significant number of methyl radicals.

4.7 Beam Contaminants:

As ethane and methane are major products in standard thermal decomposition studies of azomethane, [18] tests were performed in order to ascertain the extent of these in the beam source. Unfortunately, it was difficult to quantify the amount of methyl radical recombination. The major fragment of ethane is at m/e 28 [33] which coincides with m/e 28 signal from nitrogen, another product of azomethane dissociation. To check for ethane formation we also monitored the m/e 30, m/e 31, m/e 29, m/e 27 and m/e 26 signals, all of which are possible ion fragments of ethane. The off axis time-of-flights were identical for all of these masses and the signal at these masses could not be accounted for by leakage from m/e 28. Therefore, a significant amount of recombination was occurring. The m/e 15 signal that was observed, however, is unlikely to be a crack of ethane; ethane recoiling off neon would generate signal with a much slower laboratory velocity. To reduce the radical recombination, we maximized the ratio of the signal at m/e 15 to the signal at m/e 30 as a function of the azomethane to helium seed ratio. These conditions also gave the largest overall m/e 15 signal. After adjusting the seed ratio, we noted a significant increase in the nozzle lifetime before clogging became a problem. Therefore, not surprisingly, the reactions leading to polymer formation were also reduced at the lower seed ratio. The final azomethane to helium ratio was 1:8.

Other possible beam contaminants include methane and a variety of other hydrocarbon carbons. Since methane is only one mass unit away from methyl radical, it will scatter off the rare gas with a similar Newton circle and TOF as the methyl radical.

To check whether our m/e 15 signal was from methyl radical rather than methane, the signals at m/e 16, m/e 14, m/e 13 and m/e 12,fragment ions of both CH_4 and CH_3[33], were monitored. The signal observed at m/e 16 was 5% of the m/e 15 signal and can be accounted for by leakage in the mass spectrometer from m/e 15 and by the 1% natural abundance of ^{13}C. This suggests that the methane contamination is probably minimal. The additional vibrational energy of methane produced in the heated source, however, might shift the fragments to smaller masses as noted for azomethane.

Although the crossed beams elastic scattering experiments showed strong evidence for the presence of a significant methyl radical number density, there is a possibility that the signal is from methane formation in the beam. The ultimate test to check for methyl radicals in the beam is a reactive scattering experiment. Since it has been well established that ICl reacts with CH_3 to give CH_3I under crossed molecular beam conditions with favorable kinematics, [1, 2, 3, 4, 5, 6, 9] this reaction was used as the definitive test of our methyl radical source. Figure 4.8 shows a time-of-flight of m/e 142, the parent ion of CH_3I, at a lab angle equal to 70° which correspond to the center of mass angle. The total counting time in this spectrum was twelve minutes. This clearly demonstrates the presence of methyl radicals in the primary beam.

4.8 General Tips:

It is appropriate to document a few more general points about running this source. It was prudent to change the nozzle after about 20 hours when the carbon deposits start building up and the foreline pressure just begins to decrease. This minimizes the damage due to the carbon build up and the subsequent high resistance occurring at the junction point between the molybdenum front cap and the tungsten carbide tube. After longer running times, we found that the back junction tended to

deteriorate and the tungsten carbide tube became welded to the molybdenum cap. This is fine, of course, unless the tube clogs and needs replacement (during the reactive scattering experiments this was inevitable). Since tungsten carbide is extremely difficult to machine with standard tools, it was necessary to have the residue removed by electrical discharge machining. To remove any carbon deposits and to clean the contact point in the molybdenum cap, it was polished with diamond paste on the back of a drill bit between each run.

Careful examination of the tungsten carbide tube after a twenty hour experiment suggested that the limiting factor in the nozzle lifetime might be clogging due to the deterioration of the WC at the front junction, rather than from recombination reactions leaving deposits in the tube. A design modification where the surface area at this point is enlarged might help alleviate this problem. This, of course, will change the heater tube temperature profile. But, these changes might not be significant enough to affect the net methyl radical production.

4.9 Conclusion:

An intense methyl radical source, that is stable over twenty hours, has been generated and charaterized. The beam source configuration and running conditions have been optimized for the CH_3 production. With a few more minor modifications to lengthen its lifetime, this source should provide a greater opportunity to explore a wide variety of radical-radical and radical-molecule reactions.

4.10 References:

1. C. F. Carter, M. R. Levy and R. Grice, Faraday Discuss. **55**, 357 (1973).

2. C. F. Carter, M. R. Levy and R. Grice, Chem. Phys. Lett. **17**, 414 (1972).

3. D. L. McFadden, E. A. McCullough, F. Kalos, W. R. Gentry and J. Ross, J. Chem. Phys. **57**, 1351 (1972).

4. D. L. McFadden, E. A. McCullough, F. Kalos and J. Ross, J. Chem. Phys. **59**, 121 (1973).

5. L. C. Brown, J. C. Whitehead and R. Grice, Mol. Phys. **31**, 1069 (1976).

6. J. A. Logan, C. A. Mims, G. W. Stewart and J. Ross, J. Chem. Phys. **64**, 1804 (1976).

7. F. Kalos and A. E. Grosser, Rev. of Sci. Instr. **40**, 804 (1969).

8. P. Somssich, K. Strein and H. Schmiedel, Ber. Bunsenges. Phys. Chem. **85**, 401 (1981).

9. S. M. A. Hoffmann, D. J. Smith, J. H. Williams and R. Grice, Chem. Phys. Lett. **113**, 425 (1985).

10. J. W. Hudgens, in *Advances in Multi-photon Processes and Spectroscopy* S. H. Lin, Eds. (World Scientific, Singapore, 1987),

11. P. Chen, S. D. Colson, W. A. Chupka and J. A. Berson, J. Phys. Chem. **90**, 2319 (1986).

12. G. N. Robinson, G. M. Nathanson, R. E. Continetti and Y. T. Lee, J. Chem. Phys. **89**, 6744 (1988).

13. J. J. Valentini, M. J. Coggiola and Y. T. Lee, Rev. Sci. Instrum. **48**, 58 (1977).

14. J. M. Myers, M. J. Cote and H. F. Davis, personal communication.

15. *CRC Handbook of Chemistry and Physics* (CRC Press, Inc., Boca Raton, 1981).

16. J. Hojo, T. Shimogama and A. Kato, Nippon Kagaku Kaishi **9**, 1174 (1979).

17. W. Forst and O. K. Rice, Can. J. Chem. **41**, 562 (1963).

18. Y. Paquin and W. Forst, Int. J. of Chem. Kin. **V**, 691 (1973).

19. R. J. Crawford and K. Takagi, J. Amer. Chem. Soc. **94**, 7406 (1972).

20. M. C. Lin and K. J. Laidler, Can. J. Chem. **44**, 2927 (1966).

21. S. W. Benson, *Thermochemical Kinetics* (John Wiley & Sons, New York, 1968).

22. M. T. Macpherson, M. J. Pilling and M. J. C. Smith, J. Phys. Chem. **89**, 2268 (1985).

23. W. Braun, J. T. Herron and D. Kahaner, Gaithersburg, MD, 1986),

24. R. Renaud and L. C. Leitch, Can. J. Chem. **32**, 545 (1954).

25. Y. T. Lee, J. D. McDonald, P. R. LeBreton and D. R. Herschbach, Rev. Sci. Inst. **40**, 1402 (1969).

26. G. O. Brink, Rev. Sci. Inst. **37**, 857 (1966).

27. N. R. Daly, Rev. Sci. Instrum. **31**, 264 (1960).

28. G. Comsa, R. David and B. J. Schumacher, (1981).

29. V. L. Hirschy and J. P. Aldridge, Rev. Sci. Instrum. **42**, 381 (1971).

30. D. Krajnovich, Ph.D., University of California at Berkeley, 1983.

31. A. M. Schmoltner, P. M. Chu and Y. T. Lee, J. Chem. Phys. **91**, 5365 (1989).

32. A. M. Schmoltner, P. M. Chu, R. J. Brudzynski and Y. T. Lee, J. Chem. Phys. **91**, 6926 (1989).

33. E. Stenhagen, S. Abrahamsson and F. W. McLafferty, in *Atlas of Mass Spectral Data* (Wiley, New York, 1969),

34. H. G. Rubahn, J. P. Toennies, M. Wilde and J.Wanner, Chem. Phys. Lett. **120**, 11 (1985). and references therein.

4.11 Tables:

Heater Power	V_{pk} [a] (x10^4cm/s)	Speed Ratio	$E_{collision}$ [b] (kcal/mole)		Center of Mass Angle [c]	
			CH_3	$(CH_3)_2N_2$	CH_3	$(CH_3)_2N_2$
130	24.7	4.3	6.9	12.0	24.0°	6.5°
145	27.6	4.5	8.4	14.7	20.9°	5.6°
150	28.3	5.0	8.8	15.4	20.4°	5.5°
155	30.2	4.5	9.9	17.3	19.2°	5.1°

(a) peak in laboratory velocity.

(b) spread in collision energy ~30% fwhm.

(c) measured from CH_3/azomethane beam.

Table 4.1. Experimental beam conditions as a function of heater power.

4.12 Figures:

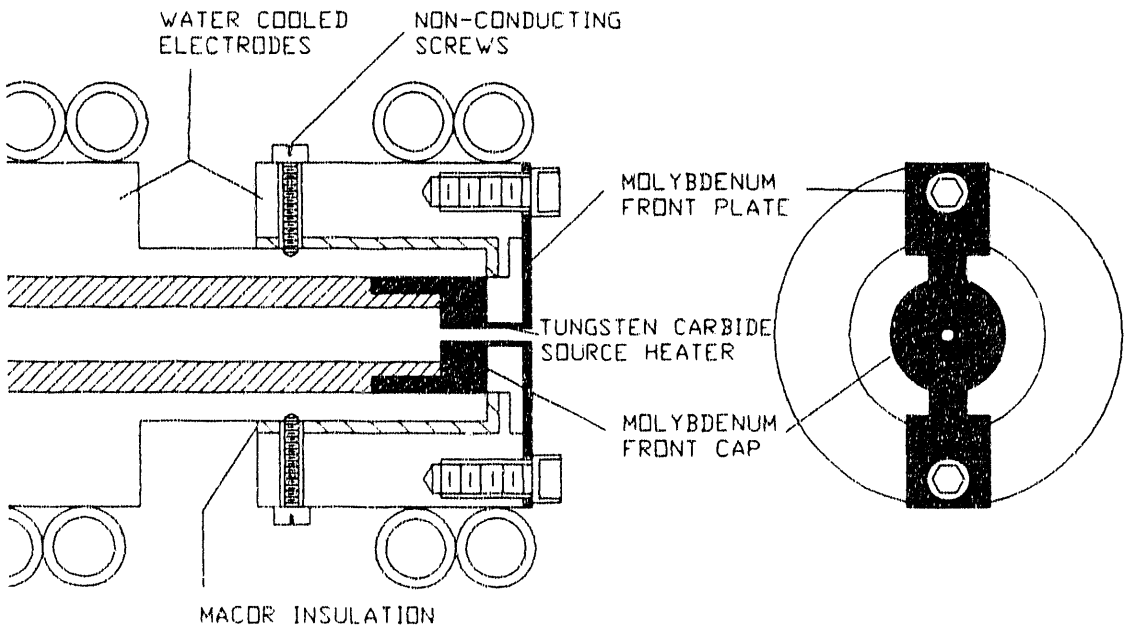

Figure 4.1: Assembly drawing of methyl radical source.

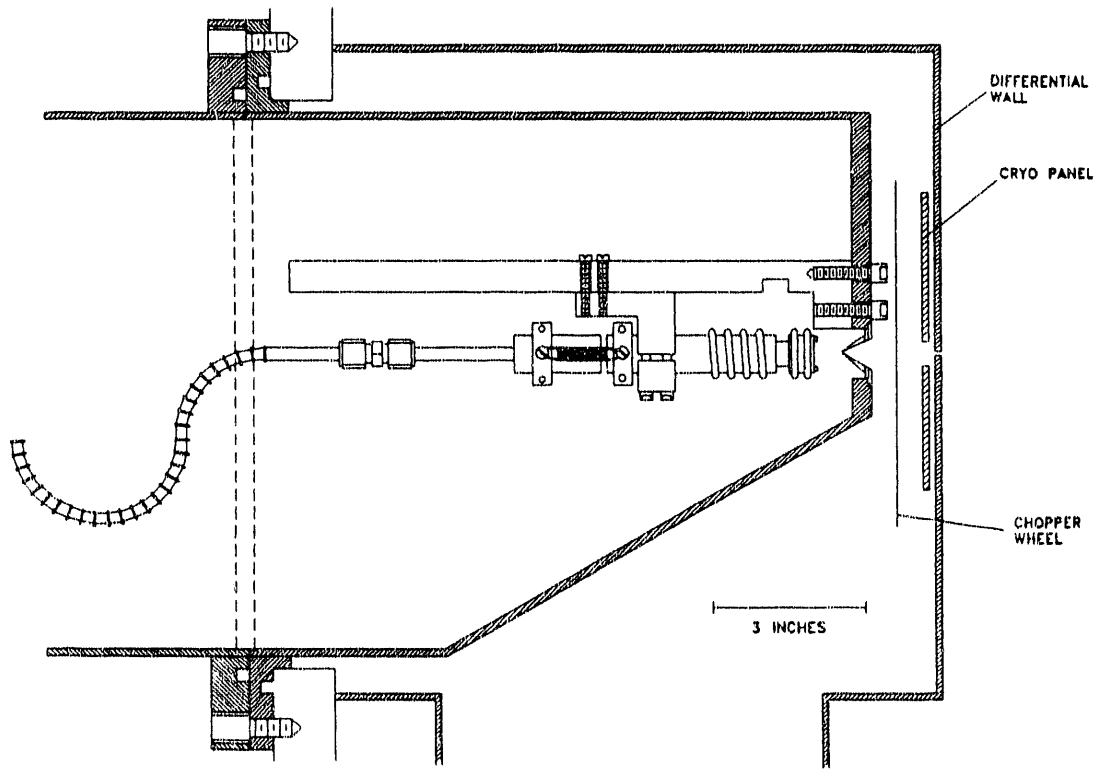

Figure 4.2: Methyl radical source shown with spring loading and mounting assembly.

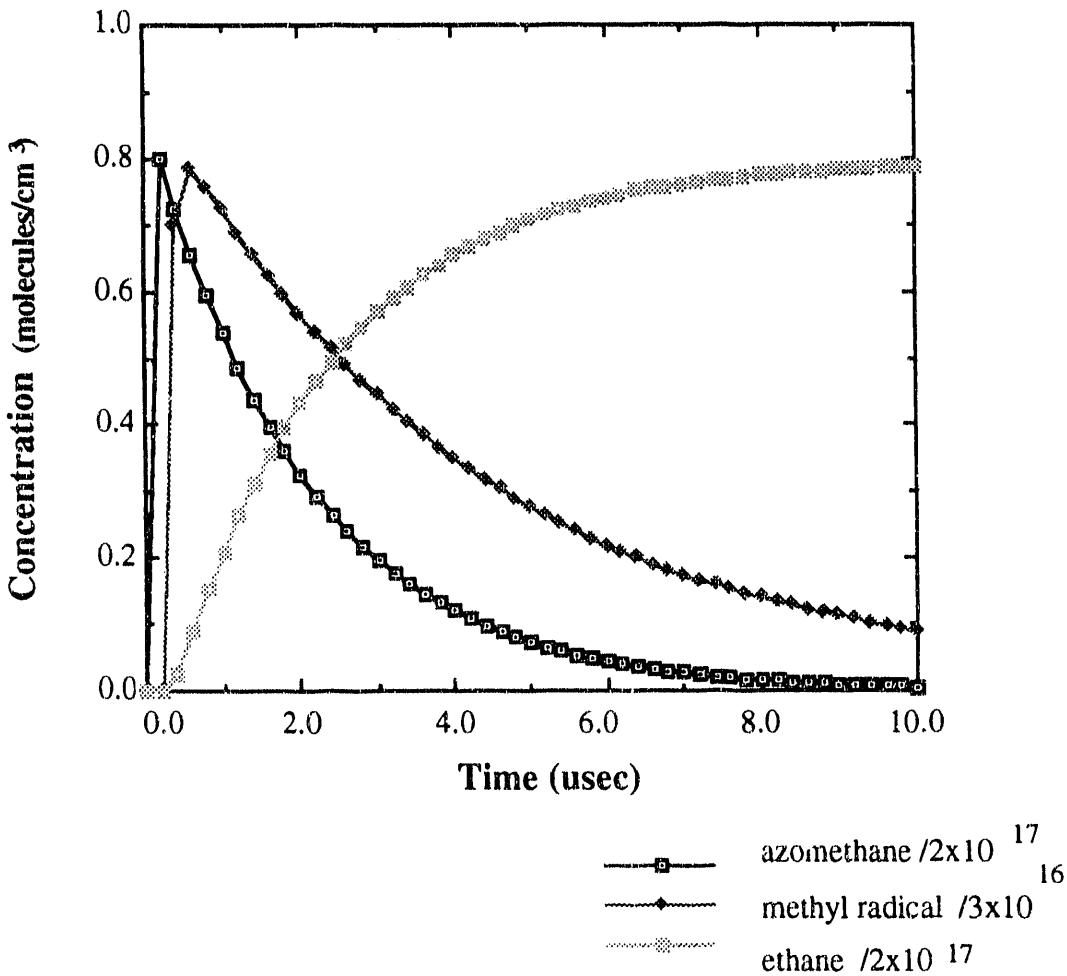

Figure 4.3: Azomethane decomposition kinetics. Azomethane, methyl radical, and ethane concentrations as a function of time. Output from Acuchem program.[23]

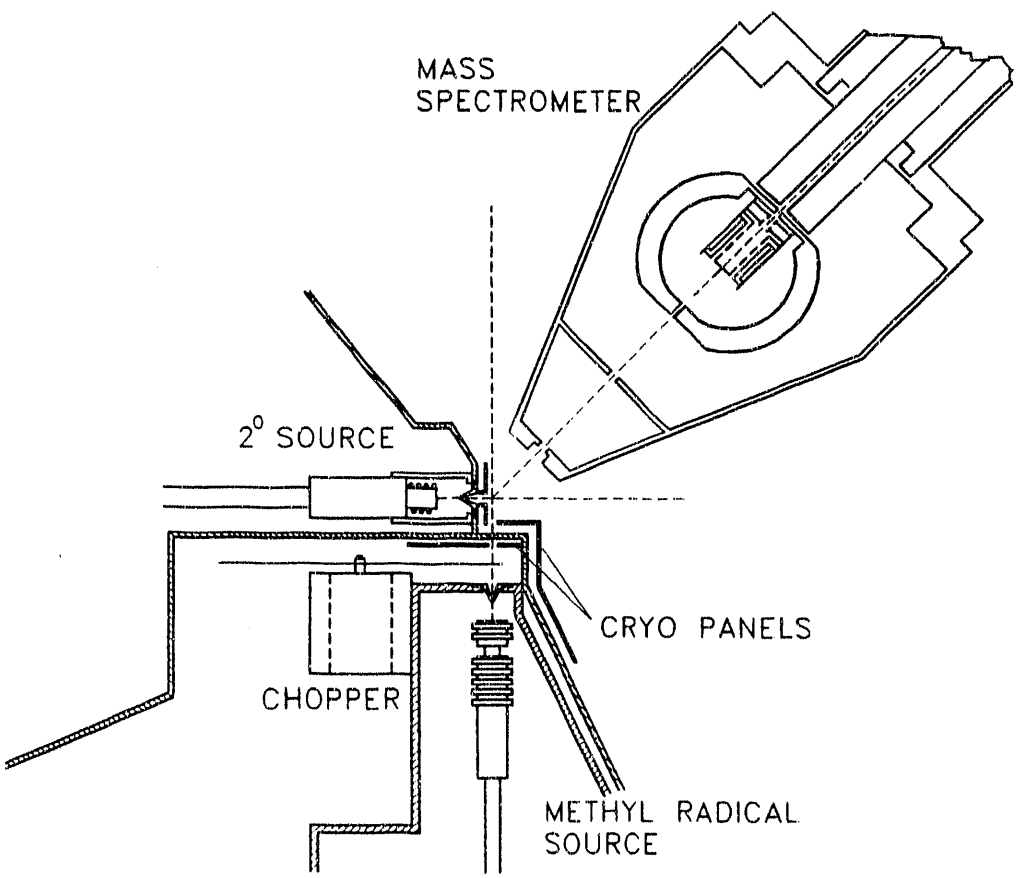

Figure 4.4: Schematic view of the crossed molecular beams apparatus with differentially pumped molecular beams and rotatable mass spectrometer detector. Dashed lines indicate reactant beams and products entering detector.

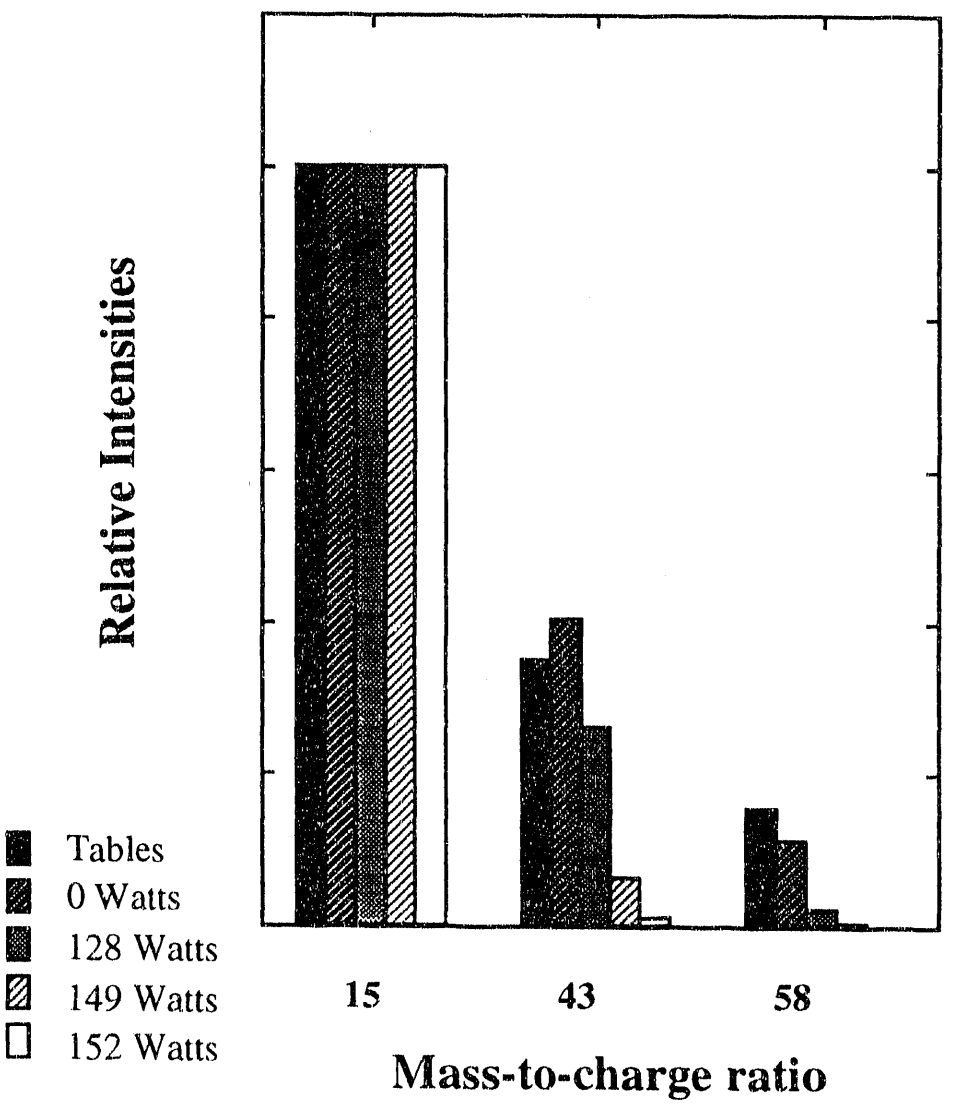

Figure 4.5: Mass spectrum of azomethane/methyl radical beam as a function ofsource heater power. M/e 15, 43, and 58 correspond to CH_3^+, $CH_3N_2^+$, and $CH_3N_2CH_3^{+\cdot}$ respectively. Table values from ref.[33]

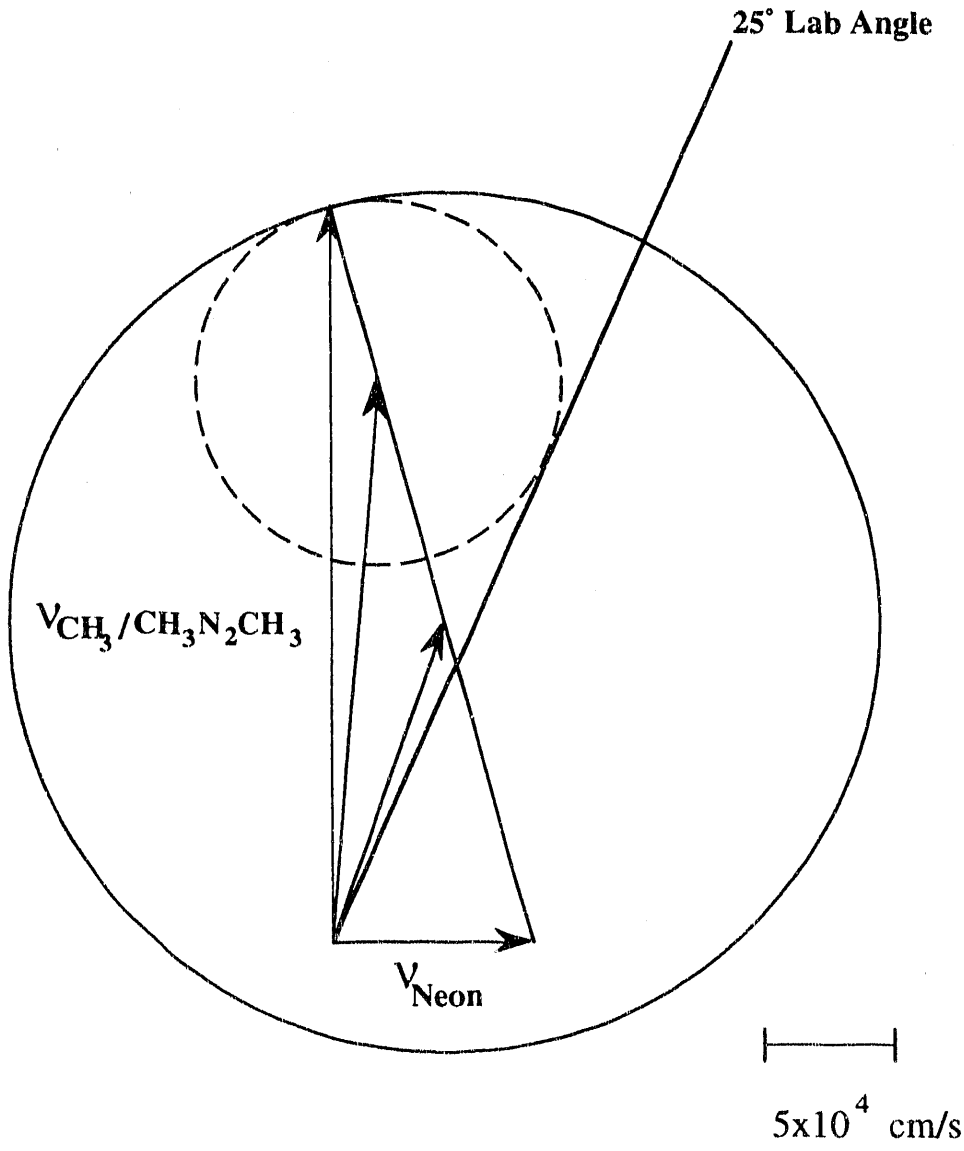

Figure 4.6: Newton diagram of methyl and azomethane elastically scattered from a neon beam. Dashed circle represents azomethane elastic circle. Solid circle represents methyl radical elastic scattering.

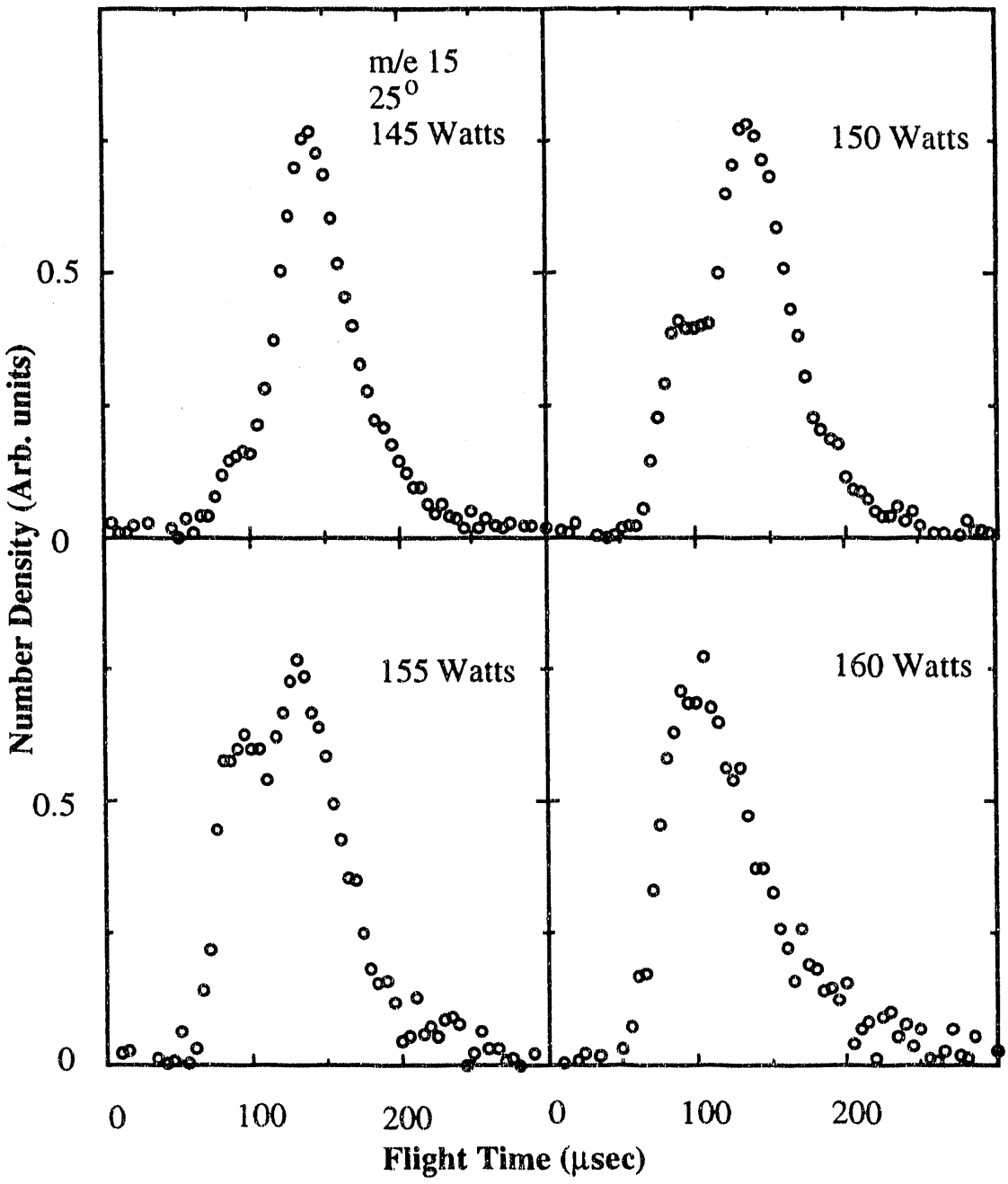

Figure 4.7: M/e 15 signal at 25° for methyl radical/azomethane beam scattered off neon. Scattered signal is shown as a function of heater power demonstrates the onset of methyl radical production. .

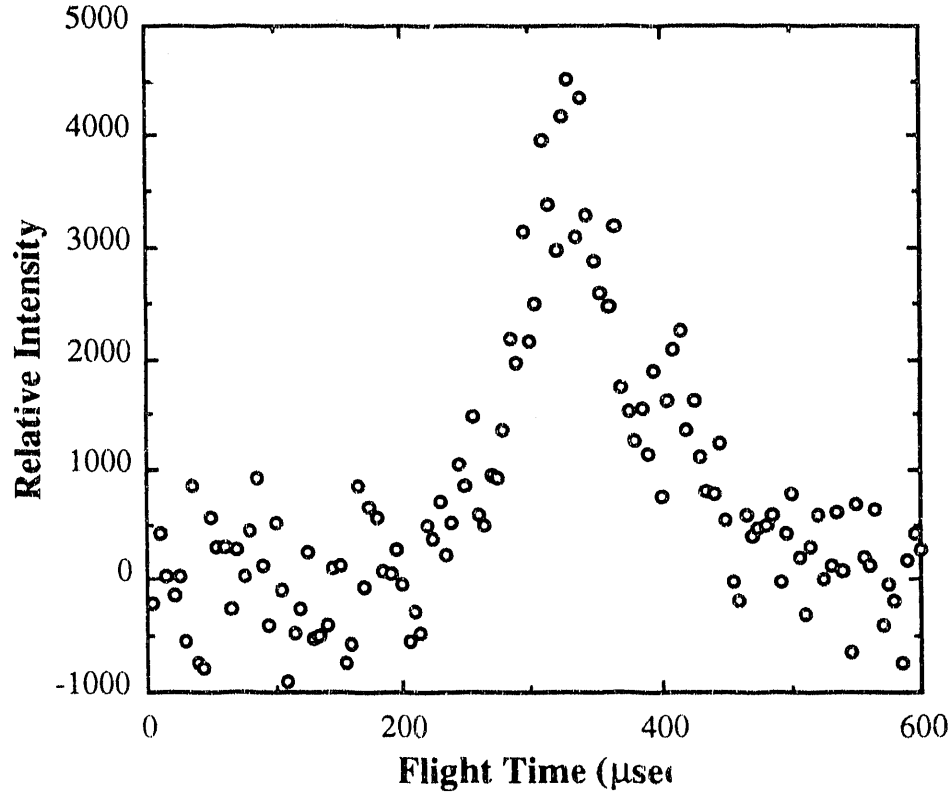

Figure 4.8: Time of flight spectrum for m/e 142 at 70° for reactive scattering of CH_3+ ICl.

4.13 Appendix:

Source Temperature Profile Model

In a pyrolysis source where recombination readily competes with radical production, such as in the case of methyl radicals, the radical precursor should remain in the heated nozzle just long enough to reach the vibrational temperature which coincides with the onset of dissociation. The source design considered two key factors to optimize the radical production and minimize the recombination: the residence time in the heated section of the nozzle and the temperature profile of the nozzle. In this section, a simple model, used to study the temperature profile of a this nozzle source shown in figure 4.1, will be described. Since translation to translation energy transfer occurs quite readily, the translational temperature profile of the gas as it flows through the heated tube should closely follow the temperature of the tube. The onset of the molecular dissociation, however, depends on the internal excitation of the molecule and therefore depends on translational to vibrational energy transfer. Since the T→V energy transfer rate is much slower than T→T, the vibrational temperature should lag behind the translational temperature.

The temperature profile of the heated tube is simply dependent on the resistivity and thermal conductivity of the material. Conductive heat loss to the gas flowing through

the tube and radiative heat loss are minimal and should not significantly change the tube's temperature profile. A maximum value for the radiative heat loss of the tube can be estimated by assuming the entire heated section of the tube reaches the highest temperature, in this case 1500 K. The total surface area is 0.049 $in^2 \equiv 3.2x10^{-5}$ m^2. From the Stefan Boltzmann law, the power radiated is given by $I=e\sigma A(T^4 - T_0^4)$. Assuming the emissivity is equal to one (the largest possible value) and given Stefan's constant, $\sigma = 5.7 \times 10^{-8}$ $W/m^2 K^4$, the total power radiated is estimated to be less than 9 Watts, less than 5% of the input energy.

The actual heat transferred to the gas can be calculated knowing the flow rate and final energy of the gas. With a 5,000 l/s diffusion pump on the source region running at $\sim 2x10^{-4}$ Torr, the gas load is 1 Torrl/s or $\sim 6x10^{-5}$ moles/s. It requires $1.5x10^4$ J/mole to heat helium from 300 to 1500K, so only ~1 Watt of heat is transferred to the gas mixture. Again, this is a very small amount compared to the total input power; the conductive heat is in fact the largest power sink.

The temperature profile can be estimated given the geometry of the heater. At steady state, the heat flow through a segment of the tube can be expressed by,

$$Q_{in} + Q_{gen} = Q_{out} \qquad (1)$$

The heat flow, Q_{in} and Q_{out} are a function of the thermal conductivity, k(T). Q_{gen}, the power dissipated in the section, is dependent on the current, I, resistivity, $\rho(T)$, and cross sectional area, A. Equation 1 can be written as:

$$-k(T)A\left(\frac{dT}{dx}\right)_x + \frac{I^2\rho(T)}{A}dx = -k(T)A\left(\frac{dT}{dx}\right)_{x+dx} \qquad (2)$$

which simplifies to:

$$\frac{k(T)d^2T}{\rho(T)dx^2} = \frac{-I^2}{A^2} \qquad (3)$$

where T equals the temperature. The integrals become more complicated and must be solved numerically when the temperature dependences of the thermal conductivity and of the resistivity are included, therefore the initial model assumed constant values for k(T)

and $\rho(T)$. For the heater configuration, it was convenient to solve equation 3 for two different segments: the tube and the front plate with cross sectional areas equal to a_1 and a_2 respectively (see figure 4.9). This was also necessary since the two sections were made of different materials (tungsten carbide and molybdenum) in the final source. The temperature of each segment was given by $T_1(x)$ from x=0 to b and $T_2(x)$ from x=b to c. The boundary conditions were:

x=0	T_1=300K
x=c	T_2=300K
x=b	$T_1=T_2$

since points x=0 and x=c were water cooled and the tube was in contact with the plate at x=b. Figure 4.9 shows a simple Mathematica[1] program written to solve the simultaneous equations resulting from the integrals with the given boundary conditions, as well as the plot of the temperature profile.

This model was used to optimize the initial dimensions of the tube and front plate. From the graph, the hottest part is within 0.5mm of the source exit, assuming a 2.0mm long tube with 1.3mm o.d. and 0.76mm i.d. for the tungsten carbide section and 2.0mm x 0.5 mm for the cross section of a 12.6mm long molybdenum front plate attached to a water cooled copper block. (See figure 4.1.)

During construction of the nozzle, it was convenient to machine the tungsten carbide tube with an extra 1.5mm back length with a 2.0mm o.d. and 0.76mm i.d.. To check how this affected the temperature profile, the program was modified to include three segments with the temperature equal to $T_1(x)$ from x=0 to p,$T_2(x)$ from x=p to q, and $T_3(x)$ from x=q to r. The boundary conditions were:

x=0	T_1=300K
x=p	$T_1=T_2$
x=q	$T_2=T_3$
x=r	T_3=300K.

The Mathematica program and resulting temperature profile, in figure 4.10, shows that the actual hottest area still falls within 0.5 mm of the nozzle tip.

Both of these models required >300 Amps to have the hottest region reach ~1500K, the source temperature where we found significant amount of methyl radical production. Only 160 Amps, however, were actually required to generate a significant number of methyl radicals. A rare gas beam was used to measure the actual temperature of the source as a function of heater current. The translational temperature of the gas should reach that of the nozzle within a few collisions and the terminal flow velocity of a rare gas in a supersonic beam is dependent on the temperature of the nozzle tip by:

$$v=\sqrt{\frac{5kT}{m}}.$$

The beam time-of-flight of argon as a function of heater power is shown in figure 4.11.

The discrepancies between the model and the experiment are likely a result of the original assumption that k(T) and ρ(T) are constant in the model calculations. The temperature dependences of k(T) and ρ(T) will change the overall temperature profile. Generally, the thermal conductivity decreases at higher temperatures, therefore as a segment gets hotter it conducts less heat. The resistance increases with temperature for molybdenum and tungsten carbide, therefore more heat will be dissipated in a segment as the temperature increases. For molybdenum, k(T) decreases by a factor of 0.73 while ρ(T) increases by a factor of 8.0 for temperatures from 20°-1200°C.[2] For the tungsten carbide segment, only data for the resistivity as a function of temperature was available. The thermal coefficient of electrical resistance for WC is $4.95\times10^{-4}deg^{-1}$,[3] and the resistance increases by a factor of 2 over the temperature range of interest. Both of these effects will generate a much steeper temperature gradients with the hottest portion reaching a higher temperatures.

It is possible to incorporate the temperature dependences of the thermal conductivity and resistivity into the model. For equation 3, one can use a polynomial to represent a function defined as k(T)/ρ(T). The set of simultaneous differential equations

can only be solved numerically with this temperature dependence and the two point boundary conditions for each equation.[4]

Another possible source of the discrepancy between the actual current needed to run the source and the calculated current is the assumption that the temperature is actually 300K at x=0. This point is not in direct contact with the water cooled copper block compared to the contact at x=r. Changing the temperature at x=0 from 300K up to 600K did not significantly effect the current required for the tip to reach 1500K, therefore the temperature dependences of k(T) and ρ(T) probably are much more important than the boundary conditions.

It was possible to roughly model the temperature of the pyrolsis source. Although the model calculations did not match our experimental values for the final heater temperature, it was useful for choosing the dimensions of the heater tube and front plate of the radical source. Unfortunately, the more interesting issue, the changes in the vibrational temperature of a radical precursor as it passes across the heater, is a far more complex problem. The vibrational temperature profile of the precursor is dependent on the efficiency of V$\rightarrow$T energy transfer, which is much slower than T$\rightarrow$T energy transfer. Experimental studies of the source performance as a function of heater tube dimensions and heater current were necessary to determine the optimum running conditions.

4.13.1 References:

1. S. Wolfram, *Mathematica A Sytem for Doing Mathematics by Computer* (Addison-Wesley Inc., Redwood City, 1988).

2. *Metals Handbook* (American Society for Metals, Cleveland, 1990).

3. G. V. Samsonov, *High Temperature Materials, Properties Index* (Plenum Press, New York, 1964).

4. W. H. Press, B. P. Flannery, S. A. Teukolsky and W. T. Vetterling, *Numerical Recipes The Art of Scientific Computing* (Cambridge University Press, Cambridge, 1988).

4.13.2 Figures:

```
C1=.; C2=.
i=350;  a1=8.08 10^-3; a2=1.03 10^-2; k1=0.423; rho1=20.2
10^-6; b=.204; c=0.839
k2=1.35;rho2=6 10^-6
B1=(i^2*rho1/(k1*a1^2))
B2=(i^2*rho2/(k2*a2^2))
constants={C1,C2}/.Solve[{B2 C1==B1 C2,  (-B1*b^2/2) +
C1*b == (-B2*b^2/2) +
     C2*b -C2*c + (B2*c^2/2)}, {C1,C2}]
C1=constants[[1]] [[1]]
C2=constants[[1]] [[2]]
temp1=(-B1*x^2)/2 + C1*x + 300
temp2=(-B2*x^2)/2 + C2*x + 300 - C2*c + (B2*c^2)/2
p1=Plot[temp1,{x,0,b}]
p2=Plot[temp2,{x,b,c}]
Show[p1,p2, PlotRange -> {0,1800}]
```

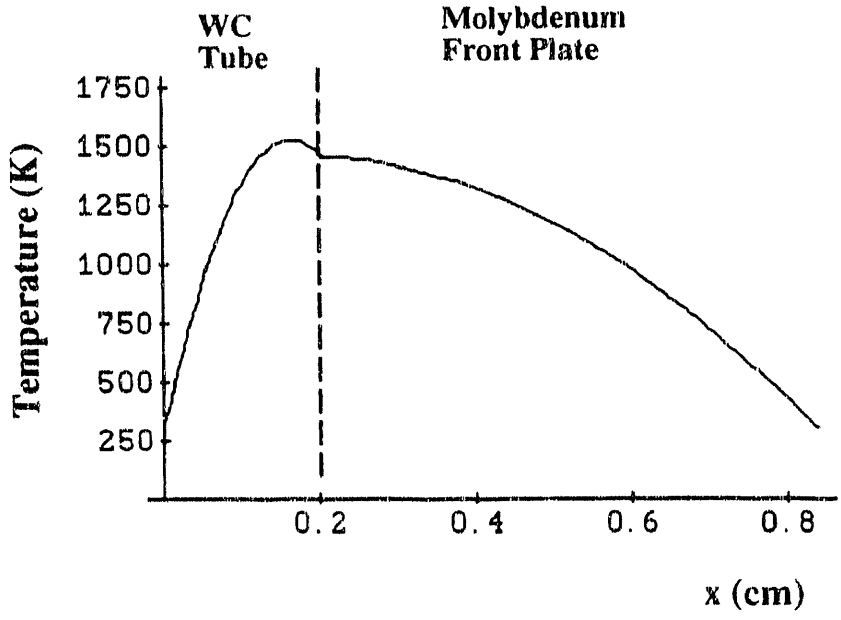

Figure 4.9: Mathematica program assuming two segments in the heater. Output of the program showing the heater temperature profile.

```
C1=.; C2=.;C3=.;D2=.;
i=325;  a1=2.70 10^-2; a2=8.08 10^-3; a3=1.03 10^-2; k1=0.423
 k2=1.35; rho1=20.2 10^-6; rho2=6 10^-6
 p=.15; q=0.35;r=1.00
B1=(i^2*rho1/(k1*a1^2))
B2=(i^2*rho1/(k1*a2^2))
B3=(i^2*rho2/(k2*a3^2))
constants={C1,C2,C3,D2}/.Solve[{B2 C1==B1 C2,  C2 B3== B2
C3,
(-B1*p^2)/2 + C1*p + 300 == (-B2*p^2)/2 + C2*p +D2,
(-B2*q^2)/2 + C2*q + D2 == (-B3*q^2)/2 + C3*q +(300 -C3*r +
(B3*r^2)/2)},
{C1,C2,C3,D2}]
C1=constants[[1]] [[1]]
C2=constants[[1]] [[2]]
C3=constants[[1]] [[3]]
D2=constants[[1]] [[4]]
temp1=(-B1*x^2)/2 + C1*x + 300
temp2=(-B2*x^2)/2 + C2*x +  D2
temp3=(-B3*x^2)/2 + C3*x + 300 - C3*r + (B3*r^2)/2
p1=Plot[temp1,{x,0,p}]
p2=Plot[temp2,{x,p,q}]
p3=Plot[temp3,{x,q,r}]
Show[p1,p2,p3, PlotRange -> {0,1800}]
```

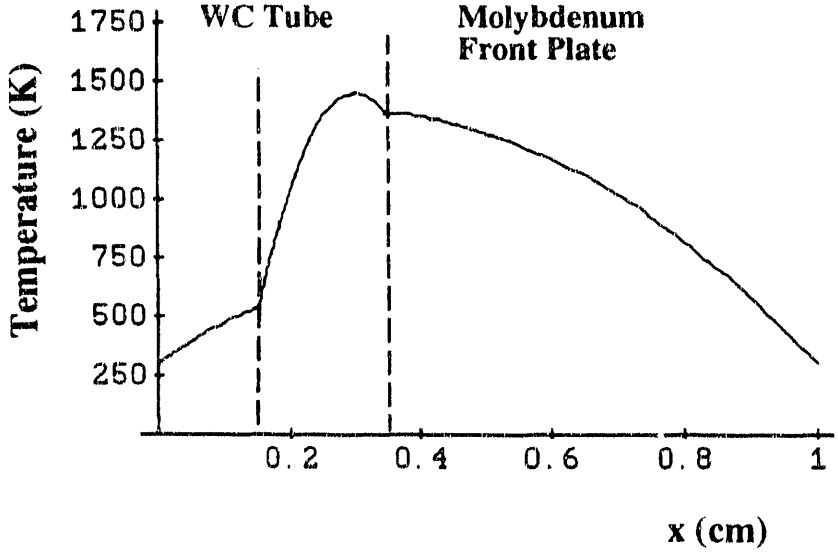

Figure 4.10: Mathematica program assuming three segments in the heater. Output of the program showing the heater temperature profile.

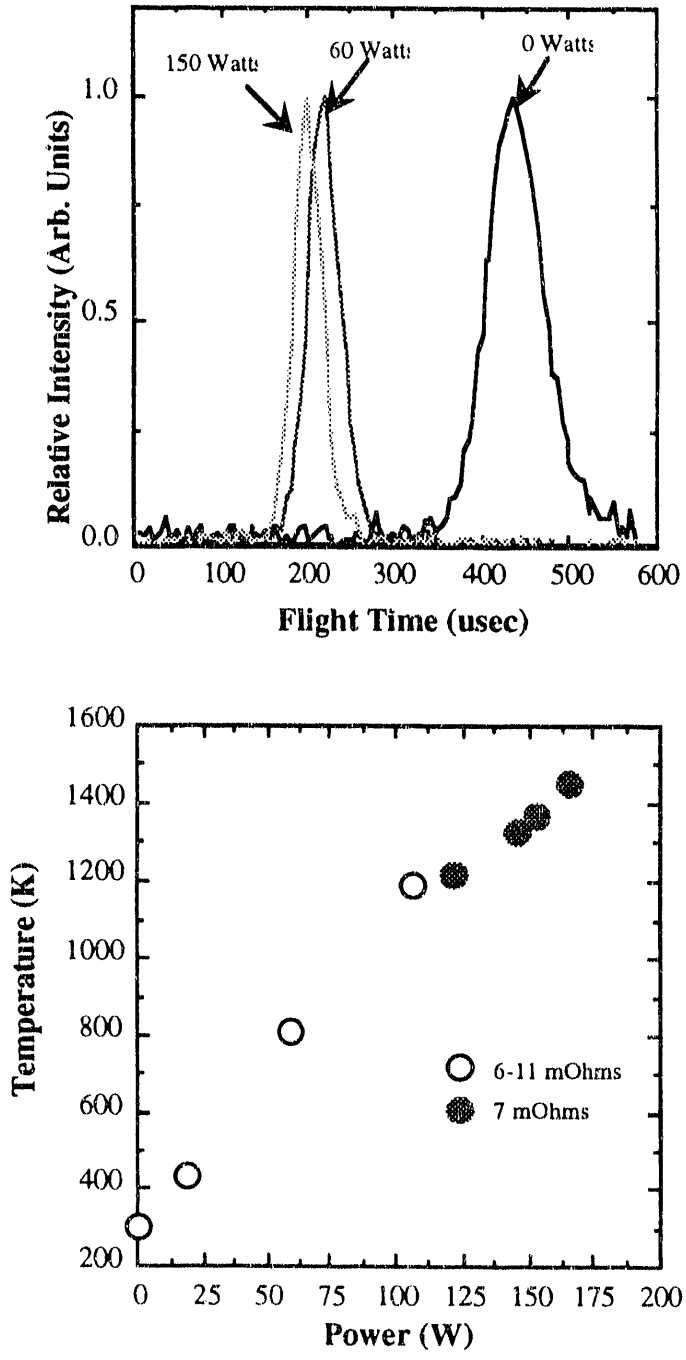

Figure 4.11: Argon beam time-of-flight as a function of heater current and oven temperature as a function of heater power.

END

DATE FILMED

12 / 17 / 92